A fundamental study of epitaxial graphene on silicon carbide on silicon for mid-infrared nanophotonics

A thesis submitted in fulfilment of the requirements for the degree of
Doctor of Philosophy

By

Patrick Rufangura
B.Sc., M.Sc.

School of Electrical and Data Engineering
Faculty of Engineering and Information Technology
University of Technology Sydney
November 2021

Abstract

The ability to control light and matter interactions at the nanoscale is a key scope of nanophotonics. In particular, the mid-infrared (MIR) range of the electromagnetic (EM) spectrum hosts several molecular vibrational fingerprints, making it an exciting spectrum for many applications such as exhaled breath detection, cancerous tissue diagnosis, water quality monitoring, greenhouse gas detection, machine vision, and navigation. Plasmonics has enabled sub-diffraction confinement and manipulation of light. However, the high losses and lack of dynamic tunability characterising the conventional metal plasmonics in the MIR ranges represent a bottleneck for further progress.

This work demonstrates that the combination of graphene and silicon carbide can enhance MIR absorption, detected field strength, and confinement. In particular, the possibility of combining the tunable nature of graphene surface plasmon polaritons (SPPs) with low loss surface phonon polaritons (SPhPs) supported in SiC offers great promise. The epitaxial graphene (EG) platform technology on cubic silicon carbide on silicon wafer has substantially advanced over the last decade and offers a straightforward, site-selective, and CMOS compatible platform for developing tailored metasurfaces made of any complex EG/SiC pattern at the wafer -scale.

This thesis combines electromagnetic simulations and experimental characterisations to reveal the fundamental optical properties of EG/SiC/Si using a forest of silicon carbide nanowires grown bottom-up on silicon as a test platform. We first demonstrate that a large wavevectors mismatch between graphene's plasmon and incident photon hinders graphene's SPP mode excitation in a flat EG/SiC/Si system. We overcome this issue by investigating the polariton modes excitation in the core/shell SiC/graphene nanowires system.

By addressing the wavevectors mismatch issue, we demonstrate absorption enhancement of MIR photons and broadening spectral resonances outside the SiC's Reststrahlen band, resulting from the hybridisation of localised SPhP-SPP modes in graphene/SiC nanowires system. Furthermore, we demonstrate extreme subwavelength confinement of the MIR photons within a few nanometers thick oxide layer between graphene and SiC. We also reveal the potential dynamic tunability of hybrid polariton modes in this system. Our simulation results suggest a more compelling need to focus on top-down fabrications of periodically ordered EG/SiC-based metasurfaces to improve further the performance of these material systems towards the MIR nanophotonics.

Certificate of original authorship

I, Patrick Rufangura, declare that this thesis is submitted in fulfilment of the requirements for the award of Doctor of Philosophy in the School of Electrical and Data Engineering, Faculty of Engineering and Information Technology, at the University of Technology Sydney.

This thesis is wholly my own work unless otherwise reference or acknowledged. In addition, I certify that all information sources and literature used are indicated in the thesis.

This document has not been submitted for qualifications at any other academic institution.

This research is supported by the Australian Government Research Training Program.

Production Note:
Signature: Signature removed prior to publication.

Date: 23rd November 2021

Dedication

To Uwiteka Imana Ishobora Byose, my wife Bona Uwera, my daughter Josie A. I. Rufangura, my parents, late Leonidas Rutsindura, and Margueritte Mukankuranga.

Acknowledgements

First and foremost, I would like to express my profound gratitude to my principal supervisor Prof. Francesca Iacopi for granting me an opportunity to join her research team and for her tremendous support throughout my PhD studies. She gave me the opportunity to realise my childhood dream by working on a fascinating nanophotonics project and introduced me to the outstanding collaborators in the nanophotonics community. Her excellent advice and endless encouragement were vital for the realisation of this PhD thesis.

Second, I would extend my sincere gratitude to A/Prof. Arti Agrawal, my co-supervisor, for invaluable support in my numerical simulations and theory. Her continuous advice and valuable advice significantly lifted my love for electromagnetic simulations a level higher and enabled me to resolve some of the fundamental problems which were hindering my PhD research progress.

My sincere gratitude goes to Prof. Christopher Poulton of the School of Mathematical and Physical Sciences at UTS for providing me with access to the COMSOL Multiphysics computational facility during my first year in this PhD project.

Further, I want to thank Dr Iryna Khodasevych, a postdoc in our Integrated NanoSystems research group at UTS, for good discussions on the mode theory in chapter 6 and valuable comments in my thesis writing. I am also very grateful for valuable discussions and support from my external supervisor, Dr Dennis Delic, from the Defence Science and Technology Group.

I gratefully acknowledge the Commonwealth of Australia, represented by the Defense Science and Technology Group, for scholarship top-up under the project-based funding agreement No.8673.

My gratitude is extended to our collaborators in the USA, Prof. Joshua D. Caldwell of Vanderbilt University and A/Prof. Thomas G. Folland of the University of Iowa for collaborations and valuable, insightful discussions on understanding the surface polariton modes in graphene and silicon carbide.

I gratefully acknowledge technical support in my experimental works provided by Dr Linda Xiao from the Forensic Unit of the science lab at the Faculty of Science at UTS for the training on Raman and FTIR spectroscopy tools. Thanks to Geoffrey McCredie for great technical assistance in the Vacuum and Cleanroom unit of the science lab, Herbert Yuan for training and

technical support on scanning electron microscope, Katie McBean for facilitating the communications with the technical team in the labs. I also acknowledge valuable discussions and support from Dr Angus Gentle, Dr Blake Regan, and Mr Caleb Estherby at the Vacuum and Cleanroom units.

I extend my sincere gratitude to Dr Matteo Bosi from IMEM-CNR Institute, Italy, for providing me with the 3C-SiC nanowires samples.

A special thanks to the University of Technology Sydney for providing me with the opportunity to undertake my PhD studies in this university and for granting me full scholarships throughout all my PhD candidature. I also acknowledge the administration and academic assistance provided by the School of Electrical and Data Engineering admin staff team.

Huge thanks go to the past and current colleagues in the Integrated NanoSystems research group: Dr Aiswarya Pradeepkumar, Dr Neeraj Mishra, Dr Mojtaba Amjadipour, Dr Anjon Kumar Mondal, Dr Shaikh Faisal, and Mr David Katzmarek, for making me feel at home from day one and encouraging discussions shared during my PhD studies.

Special thanks to the family of Missionary Moses Kang for the warmest hospitality and prayers support during this PhD journey and for providing my first ever accommodation in their beautiful home when I first landed in Sydney.

Last but not least, I express my profound gratitude to my beautiful wife for her tremendous support and patience during my PhD candidature. She has been a continuous source of support, love, encouragement, and care for our family, contributing immensely to completing this PhD thesis. Thanks to my daughter for being very patient when I was absent from playing busy with PhD research. Her patience has been a source of motivation in my PhD journey.

List of Publications

Journal articles

1. **Rufangura, Patrick**, Iryna Khodasevych, Arti Agrawal, Matteo Bosi, Thomas G. Folland, Joshua D. Caldwell, and Francesca Iacopi. "Enhanced Absorption with Graphene coated Silicon carbide Nanowires for Tunable Mid-Infrared Nanophotonics." **Nanomaterials 11, no. 9 (2021): 2339.**

2. **Rufangura, Patrick**, Thomas G. Folland, Arti Agrawal, Joshua D. Caldwell, and Francesca Iacopi. "Towards low-loss on-chip nanophotonics with coupled graphene and silicon carbide: a review." **Journal of Physics: Materials 3, no. 3 (2020): 032005**

Conferences

1. **Rufangura, Patrick**, Arti Agrawal, Thomas G. Folland, Joshua D. Caldwell, and Francesca Iacopi. "Enhanced Absorption with Core/Shell Silicon Carbide/Graphene Nanowires for Tunable Mid-Infrared Nanophotonics." Oral Presentation **In 63rd Electronic Materials Conference (63rd EMC), June 23-25, 2021.**
2. **Rufangura, Patrick**, Arti Agrawal, Matteo Bosi, Thomas G. Folland, Joshua D. Caldwell, and Francesca Iacopi. "Enhanced Mid-Infrared Reflectance with Graphene Coated Silicon Carbide Nanowires." Oral Presentation **In Conference on Lasers and Electro-Optics/Pacific Rim, p. C11E_2. Optical Society of America, 2020.**

Table of Contents

List of Figures

List of Acronyms

EM	Electromagnetic
TE	Transverse electric
TM	Transverse magnetic
EG	Epitaxial graphene
SiC	Silicon carbide
3C-SiC	Cubic silicon carbide
Si	Silicon
NW	Nanowire
LO	Longitudinal optical phonon
TO	Transverse optical phonon
SPP	Surface plasmon polariton
SPhP	Surface phonon polariton
LSPP	Localised surface plasmon polariton
LPhP	Localised surface phonon polariton
FOM	Figure of merit
IR	Infrared
NIR	Near-infrared
MIR	Mid-infrared
FIR	Far- infrared
FTIR	Fourier transformed infrared
ATR	Attenuated total Reflection
SEM	Scanning electron microscopy
TEM	Transmission electron microscopy
CVD	Chemical vapor decomposition
CMOS	Complementary metal-oxide-semiconductor
GOS	Graphene on silicon
NA	Numerical aperture
FEM	Finite element method
SNOM	Scanning near field optical microscopy
AREELS	Angle-resolved electron energy loss spectroscopy
HREELS	High-resolution electron energy loss spectroscopy

CST	Computer simulation technology
HFSS	High-frequency structure simulator
PARDISO	Parallel direct sparse solver
MD	Mirror displacement
2D	Two dimensional
CM	Collimating mirror
ILS	Infrared light source
Ph.D.	Doctor of Philosophy
UTS	University of Technology Sydney
TMOS	Transformative Meta-optical systems
INSys	Integrated Nanosystems

Chapter 1: Introduction

1.1.Background and Motivation

"Optics" is a branch of physics, which deals with the behaviour and properties of light, light and matter interaction, and associated applications. It achieved considerable progress since the invention of the classical theory of electromagnetic field by James Clerk Maxwell in the 19th century[1]. Conventional optics uses materials with a positive real part of the dielectric function to propagate and manipulate electromagnetic (EM) waves at optical frequencies. The benefit associated with the use of plane waves and refractive optics is that they enable propagation and manipulation of light over long distances with comparative ease. However, as a consequence of the diffraction limit first reported by Ernst Abbe in 1873, a beam of light travelling in a medium with refractive index (n) and a converging half-angle θ, a minimum resolvable size of $\mathrm{d} = \frac{\lambda}{2\mathrm{NA}}$ results, where NA is the numerical aperture of the lens and $\mathrm{NA} = \mathrm{n}\sin\theta$. For a microscope objective of $\mathrm{NA} = 1$, the minimum focal spot is $\mathrm{d} = \frac{\lambda}{2}$, from roughly a quarter of a micron for the blue end of the visible spectrum and extending to several microns for longer-wavelength infrared light[2-4].

For mid-infrared (MIR) and far-infrared (FIR) light, the focusing of light to nanoscale dimensions is not realistic. Such wavelengths of light are advantageous for many applications ranging from vibrational spectroscopy enabling insights into the composition of chemicals and materials, and they provide non-contact monitoring of temperature, offer the promise of minimal free-space attenuation of light by the atmosphere, as well as limiting light-induced damage on samples of interest associated with higher frequency light sources. However, the long wavelengths that enable these applications also imply that the requisite optical components must also be at wavelength scale or larger, limiting opportunities for compact solutions. Thus, there is a strong desire for photonic solutions that enable operations beyond the diffraction limit, which has sparked a substantial body of works in plasmonics and metamaterials over recent years [5].

Nanophotonics offers the possibility to improve infrared (IR) technology significantly[6, 7]. Surface plasmon polariton (SPP) modes result from strong coupling of bound EM fields with collective charge oscillations (plasmon) in a conductor, enabling sub-diffraction manipulation of light. Graphene is one of the promising plasmonic materials that can excite strongly confined SPPs in the MIR and FIR spectral ranges with remarkable dynamic tunability and electric field confinement, unrealisable with conventional metal plasmonics[6, 8-11]. To date, several graphene-based novel photonic devices such as optical modulators[12], photodetectors[13-16], switches[17], antennas[18], waveguides[19], sensors[10], and polarisers[20] were proposed.

On the other hand, polar dielectric materials such as BN, SiO_2, and SiC simultaneously support low loss and sub-wavelength confined EM fields in the MIR and FIR spectral range via the stimulation of surface phonon polariton (SPhP) modes[4, 21]. SPhPs arise from the strong interaction of EM waves and collective vibration of ionic lattice within the Reststrahlen band, a narrow spectral range between transverse optical (TO) and longitudinal optical (LO) phonon frequencies. The ability to confine MIR wavelengths through excitation of SPPs and SPhPs has many implications for optics and optoelectronic technologies such as MIR photodetection[16], sensing[22], and photovoltaics cells[23]. Optical devices that combine graphene and polar materials are inferred to significantly advance MIR photonic technologies due to the exceptional polaritonic responses resulting from the hybridisation of SPP and SPhP modes in these material systems. For example, recent studies of hybrid SPP-SPhP modes in graphene on polar materials revealed the resultant dispersion relation to be significantly modified[24-27].

Thanks to the advancement of graphene synthesis techniques, the 2D material can now be grown on, or transferred to, and characterised with different polar dielectric substrates [28]. However, in most cases, the transfer of graphene onto the substrate deteriorates graphene's properties and is limited to small-scale samples. Epitaxial graphene (EG) grown on silicon carbide is a suitable platform for growing graphene directly on semiconductors for diverse technologies and applications[28, 29]. Over the past few years, some theoretical and experimental works were optically conducted on graphene on bulk silicon carbide[26, 30-32]. Uniform quality EG can now be grown over a large scale on silicon carbide on silicon [28, 33, 34]. Notably, our research group at the University of Technology Sydney successfully developed a novel alloy mediated catalytic method[33-35] that enables epitaxial graphene growth on cubic silicon carbide on silicon (EG/3C-SiC/Si) substrates. This offers the opportunity to develop and characterise complex graphene/silicon carbide 3D photonic structures at the wafer-scale with nanoscale precision, using advanced silicon processing technologies. Moreover, this technique enables the growth of EG conformally on the structured SiC surfaces[36, 37].

1.2. Aims and objectives

This thesis aims to investigate the fundamental optical properties of epitaxial graphene on cubic-silicon carbide on silicon(EG/3C-SiC/Si) and develop an EG/SiC photonic model to serve as a robust platform towards EG/SiC-based nanophotonics for mid-infrared applications. The following are specific objectives:

- To develop a theoretical understanding of the hybrid phonon-plasmon polariton in epitaxial graphene on silicon carbide.
- To investigate excitation of surface phonon polariton in cubic silicon carbide on silicon in flat SiC/Si system using numerical simulations and experimental characterisations, and examine the effect of parameters such as different polarisation and angles of incident electromagnetic radiation, and thickness of dielectric space, on the resonant excitation of surface phonon polariton in a flat SiC/Si system.
- To investigate excitation of localised surface phonon polariton and surface plasmon in graphene-coated SiC nanowires using numerical simulations and experimental characterisation and analyse hybridisation of the polariton modes in these material systems.
- To perform a sensitivity analysis on the parameters which affect the hybridisation between SPhP and SPP modes in EG/SiC nanowires.
- To assess the achievable electric field enhancement, confinement and tunability of the hybrid modes in the curved EG/SiC nanowires and extrapolate potential uses with an ordered/ periodic metasurface.

1.3. The significance of the research

A detailed understanding of the fundamental optical properties of graphene on silicon carbide on silicon substrates will enable the design and fabrication of EG/SiC/Si-based metasurfaces for mid-infrared applications using advanced silicon processing technologies. There are at least four potential sectors expected to benefit from this project, as it will progress further within the further research of the ARC Centre of Excellence for Transformative Meta-Optical Materials:

- First is the health sector, where compact photonic devices such as bio-detectors, sensors, and lasers are needed for rapid disease diagnosis and treatment. The polariton modes in graphene and SiC have their resonances in the MIR spectrum, a range known to host several bio-molecular and proteins fingerprints, and this makes the EG/SiC material a potential platform for miniaturised medical sensors and imaging detectors.

- The second sector is military and defence. Most military and defence operations such as surveillance and targeting occur under cover of darkness, which makes it hard to detect with visible detectors and sensors[38]. For instance, it is almost impossible to detect a threat moving behind foliage in the dark at night using visible detectors. EG/SiC-based tunable metasurfaces could be designed and fabricated for MIR detection and sensing of dark objects that are opaque to visible light and for night vision.
- The third sector is energy. Light and energy saving is another field to benefit from this project, where graphene/SiC-based metamaterial absorbers could be designed and fabricated to increase the efficiencies of solar cell devices extending the response range to the MIR.
- The fourth sector is communications. The current state of communications and data sharing needs fast, dynamic, and broadband internet, which can be addressed by developing novel nanophotonic devices. Graphene waveguides have been investigated in recent years [39-42]. On the other hand, a combination of graphene and polar materials is believed to improve the propagation length of hybrid polariton modes which are very important for plasmonic waveguides[27]. Therefore, photonic waveguides based on the EG/SiC system could be designed and fabricated to improve communications and data sharing.

1.4. Thesis structure

Chapter 1 is an introduction. It starts with a brief introduction and motivation of the research. The chapter also provides the study's aim, objectives, and significance and concludes with the thesis structure.

Chapter 2 provides detailed background on surface polariton modes. It starts with discussions on the solutions of Maxwell equations. The chapter discusses the general theory of surface wave excitation on a planar interface between a conductor and dielectric using a case study of an air-silver system. Subsequently, the chapter provides a detailed theory of surface plasmon and surface phonon polariton excitation in silicon and graphene and discusses the dispersion relations of individual polariton modes and hybrid mode in a combined graphene /silicon carbide material system. The chapter concludes with the calculations of propagation and confinement figures of merit for hybrid phonon-plasmon polariton mode in graphene/silicon carbide material system

Chapter 3 focused on the literature review. It starts with a review of different graphene synthesis techniques focusing on the epitaxial growth of graphene on silicon carbide on silicon. The second part of the chapter reviews the recent progress on graphene and silicon carbide-based nanophotonics.

Chapter 4 discusses the two methodologies used in this thesis. First, the experimental part, which comprises material synthesis, and infrared characterisation, is described. Then the second part discusses the numerical modelling and the simulation tools employed in this thesis focusing on the finite element method and COMSOL Multiphysics.

Chapter 5 discusses the designed photonic model to investigate surface polariton modes in a flat graphene/ silicon carbide system. The first part of the chapter discusses how we built our graphene on a silicon carbide model in COMSOL Multiphysics and mesh benchmark for convergency test of the model. The second part of chapter 5 details the simulations performed and sensitivity studies to analyse surface phonon and plasmon polariton modes excitation in graphene and silicon carbide. The chapter concludes with the experimental characterisations of epitaxial graphene grown on an unpatterned cubic silicon carbide on silicon to validate the simulation results.

Chapter 6 discusses the excitation and hybridisation of localised surface phonon-plasmon polariton modes in the core/shell silicon carbide/ graphene nanowires. It starts by creating a graphene/silicon carbide nanowire COMSOL Multiphysics simulation model to investigate the localised surface phonon and plasmon polaritons modes excitation and their hybridisation. This is followed by an analysis of the modes and electric field enhancement, different sensitivity studies, and tunability analysis of the hybrid polariton modes in the graphene/SiC nanowires system. The second part of the chapter focuses on experiments and measurements conducted on the core/shell silicon carbide/ graphene nanowires. The chapter concludes with discussions and comparisons between experimental results with the simulations.

Chapter 7 summarises the main findings of this work and proposes future directions and developments.

Chapter 2. Theoretical background on the surface polariton modes

At the MIR and THz regions, graphene behaves like metals with a definite conductivity dominated by intra-band transitions and a Drude like behaviour with a complex dielectric function consisting of negative real permittivity and positive imaginary permittivity[43]. Hence, this chapter starts with a general theory of conventional metal plasmonics to understand the physics behind the excitation of SPP mode in a conductor using metal. Later in the chapter, the theory is extended to the particular study of graphene plasmonics and phonon polariton in SiC.

2.1. Maxwell's equations and fundamentals of plasmonics

The fundamental behaviour of materials when interacting with electromagnetic (EM) fields can be described by the solutions of Maxwell's equations. Notably, the dielectric function of metals depends on the frequency of EM waves interacting with them. This strong dependency on the frequency, which is called the dispersive nature of metals, can be analysed through their complex dielectric function $\varepsilon(\omega)$. In this section, we start with the four sets of Maxwell's equations (2.1-2.4) to examine the behaviour of metal in the presence of EM fields.

$$\nabla . \mathbf{D} = \rho_{\mathrm{ext}} \tag{2.1}$$

$$\nabla . \mathbf{B} = 0 \tag{2.2}$$

$$\nabla \times \mathbf{E} = -\frac{\partial \mathbf{B}}{\partial \mathrm{t}} \tag{2.3}$$

$$\nabla \times \mathbf{H} = \mathbf{J}_{\mathbf{ext}} + \frac{\partial \mathbf{D}}{\partial \mathrm{t}} \tag{2.4}$$

D, **E**, **H**, and **B** represent dielectric displacement, electric field, magnetic field, and magnetic induction/magnetic flux density, respectively whereas ρ_{ext} and $\mathbf{J}_{\mathbf{ext}}$ are charge and surface current density. The total current and charge density can be given by the sum of internal and external components of these quantities. $\mathbf{J} = \mathbf{J}_{\mathbf{ext}} + \mathbf{J}_{\mathbf{internal}}$, and $\rho = \rho_{\mathrm{ext}} + \rho_{\mathrm{internal}}$.

The four Maxwell's equations are connected by electric polarisation (**P**) and magnetisation (**M**), as shown by the equations (2.5) and (2.6).

$$\mathbf{D} = \varepsilon_0 \mathbf{E} + \mathbf{P} \tag{2.5}$$

$$\mathbf{H} = \frac{1}{\mu_0}\mathbf{B} - \mathbf{M} \tag{2.6}$$

μ_0 , and ε_0 define magnetic permeability and electric permittivity of free space, respectively. **P** is electric polarisation, defined as an electric dipole moment per unit volume into the material resulting from microscopic dipoles alignment with the electric field. The divergence of electric polarisation yields internal charge density and can be described by (2.7).

$$\nabla.\mathbf{P} = -\rho_{\text{internal}} \tag{2.7}$$

By inserting relation (2.5) into (2.1), we can get an equation that combines both external and the induced charge density as follows,

$$\nabla.(\varepsilon_0\mathbf{E} + \mathbf{P}) = \rho_{\text{ext}}$$

$$\nabla.\varepsilon_0\mathbf{E} + \nabla.\mathbf{P} = \rho_{\text{ext}}$$

$$\nabla.\varepsilon_0\mathbf{E} - \rho_{\text{internal}} = \rho_{\text{ext}}$$

$$\nabla.\mathbf{E} = \frac{\rho}{\varepsilon_0} \tag{2.8}$$

One can use equations (2.5) and (2.8) while considering isotropic, linear, and non-magnetic media and get two sets of equations, (2.9) and (2.10), describing how matter and EM fields interact.

$$\mathbf{D} = \varepsilon_0\varepsilon\mathbf{E} \tag{2.9}$$

$$\mathbf{B} = \mu_0\mu\mathbf{H} \tag{2.10}$$

Here ε is frequency-dependent relative permittivity (dielectric function), and μ is magnetic permeability, which is assumed to be 1 for the non-magnetic media. The dielectric function of a material is an essential parameter for analysing the phenomena that occur when it interacts with EM fields.

In the next section, we analyse the behaviour of a conductor when interacting with an EM plane wave at a planar interface. For simplicity, in this section, we consider a planar interface between a metal and dielectric.

2.2. Surface wave at the planar interface between a metal and a dielectric

Surface plasmon polaritons (SPPs) are the EM surface modes that are excited and propagate at the interface between a conductor, typically metal with negative real permittivity, and dielectric material with positive permittivity. Since SPP modes are the surface wave, their field intensity is maximum at a conductor-dielectric interface and vanishes exponentially in the direction perpendicular to the interface.

We use the wave equation and Maxwell's equation in (2.1-2.4) to describe the fundamental properties of surface plasmon polariton at a flat interface between metal and dielectric.

As a starting point, let us assume the external charge and surface current densities to be zero. Thus the combination of the two curls in Maxwell's equations (2.3, 2.4) yields the following expression;

$$\nabla \times \nabla \times \mathbf{E} = -\mu_0 \frac{\partial^2 \mathbf{D}}{\partial t^2} \tag{2.11}$$

Using identity relations[44]: $\nabla \times \nabla \times \mathbf{E} = \nabla(\nabla.\mathbf{E}) - \nabla^2\mathbf{E}$ and $\nabla.(\varepsilon\mathbf{E}) = \mathbf{E}.\nabla\varepsilon + \varepsilon\nabla.\mathbf{E}$, with the assumption that there is no external source (i.e., $\nabla.\mathbf{D} = 0$), equation (2.11) can be modified to give (2.12),

$$\nabla\left(-\frac{\mathbf{E}}{\varepsilon}.\nabla\varepsilon\right) - \nabla^2\mathbf{E} = -\mu_0\varepsilon\varepsilon_0 \frac{\partial^2 \mathbf{E}}{\partial t^2} \tag{2.12}$$

If we consider a minimal variation of the dielectric profile over distances ($\nabla\varepsilon = 0$), equation (2.12) can be adjusted into a fundamental equation that describes the theory of EM wave.

$$\nabla^2\mathbf{E} - \mu_0\varepsilon\varepsilon_0 \frac{\partial^2 \mathbf{E}}{\partial t^2} = 0 \tag{2.13}$$

Equation (2.13) can be solved independently in the medium with permittivity (ε), using appropriate boundary conditions and by taking a harmonic time dependence of electric field ($\mathbf{E}(r,t) = \mathbf{E}(r)e^{-i\omega t}$). Thus, the modified (2.13) yields the Helmholtz equation (2.14).

$$\nabla^2\mathbf{E} + \frac{\omega^2}{c^2}\varepsilon\mathbf{E} = 0 \tag{2.14}$$

where, $c = \sqrt{\frac{1}{\mu_0\varepsilon_0}}$ is the speed of light in the free space

We can now analyse a propagating surface EM wave at the planar interface between a conductor and dielectric media using equation (2.14).

As depicted in Figure 2.1 for simplicity, we consider a one-dimensional problem where dielectric permittivity changes only along one spatial coordinate, particularly the wave propagating along the x-direction, while showing no spatial variation in the y-direction, i.e., $\varepsilon = \varepsilon(z)$[44].

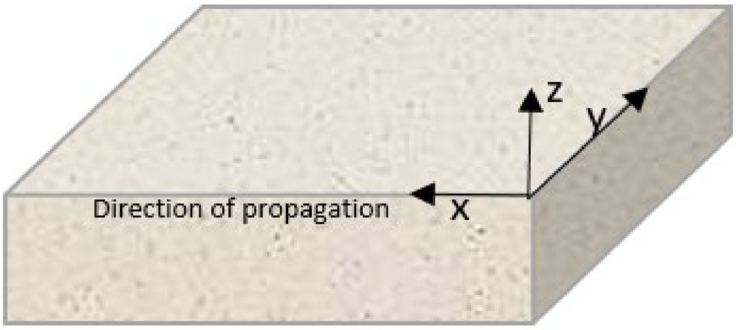

Figure 2.1. Schematic of the planar interface with the wave propagating along the x-direction of the coordinate system.

The propagating wave can be characterised by $\mathbf{E}(x, y, z) = \mathbf{E}e^{ik_x x}$ where k_x stands for a complex propagation constant of a propagating wave and defines the wavevector's component in the direction of propagation. By inserting this equation into equation (2.14), we obtain a wave equation as a function of the electric field.

$$\frac{\partial^2 \mathbf{E}(z)}{\partial z^2} + \left(\left(\frac{\omega}{c}\right)^2 \varepsilon - {k_x}^2\right) \mathbf{E}(z) = 0 \tag{2.15}$$

Typically, equation (2.15) has its counterpart for the magnetic field (2.16), which can be obtained by applying appropriate boundary conditions on Maxwell's equation and using a propagating wave equation with the magnetic field.

$$\frac{\partial^2 \mathbf{H}(z)}{\partial z^2} + \left(\left(\frac{\omega}{c}\right)^2 \varepsilon - {k_x}^2\right) \mathbf{H}(z) = 0 \tag{2.16}$$

Expression (2.15) and (2.16) are the starting points for thoroughly understanding the theory of EM waves propagating at a planar interface between two mediums[45].

In order to use the wave equation to understand the dispersion of a propagating surface wave and spatial field, we need to find mathematical expressions for different **E** and **H** fields components. The curl of equations (2.3) and (2.4) and harmonic time dependence $\left(\frac{\partial}{\partial t} = -i\omega\right)$ lead to the six sets of equations containing **E** and **H** components of the fields.

$$\frac{\partial \mathbf{H}_z}{\partial y} - \frac{\partial \mathbf{H}_y}{\partial z} = -i\omega\varepsilon_0\varepsilon\mathbf{E}_x \tag{2.17}$$

$$\frac{\partial \mathbf{H}_x}{\partial z} - \frac{\partial \mathbf{H}_z}{\partial x} = -i\omega\varepsilon_0\varepsilon\mathbf{E}_y \tag{2.18}$$

$$\frac{\partial \mathbf{H}_y}{\partial x} - \frac{\partial \mathbf{H}_x}{\partial y} = -i\omega\varepsilon_0\varepsilon\mathbf{E}_z \tag{2.19}$$

$$\frac{\partial \mathbf{E}_z}{\partial y} - \frac{\partial \mathbf{E}_y}{\partial z} = i\omega\mu_0\mathbf{H}_x \tag{2.20}$$

$$\frac{\partial \mathbf{E}_x}{\partial z} - \frac{\partial \mathbf{E}_z}{\partial x} = i\omega\mu_0\mathbf{H}_y \tag{2.21}$$

$$\frac{\partial \mathbf{E}_y}{\partial x} - \frac{\partial \mathbf{E}_x}{\partial y} = i\omega\mu_0\mathbf{H}_z \tag{2.22}$$

For the wave propagating only along the x-direction $\left(\frac{\partial}{\partial x} = ik_x\right)$ with homogeneity (i.e., no variation) in y-direction coordinate $\left(\frac{\partial}{\partial y} = 0\right)$, equation (2.17-2.22) can be modified as follows;

$$\frac{\partial \mathbf{E}_y}{\partial z} = -i\omega\mu_0\mathbf{H}_x \tag{2.23a}$$

$$\frac{\partial \mathbf{E}_x}{\partial z} - ik_x\mathbf{E}_z = i\omega\mu_0\mathbf{H}_y \tag{2.23b}$$

$$ik_x\mathbf{E}_y = i\omega\mu_0\mathbf{H}_z \tag{2.23c}$$

$$\frac{\partial \mathbf{H}_y}{\partial z} = i\omega\varepsilon_0\varepsilon\mathbf{E}_x \tag{2.24a}$$

$$\frac{\partial \mathbf{H}_x}{\partial z} - ik_x\mathbf{H}_z = -i\omega\varepsilon_0\varepsilon\mathbf{E}_y \tag{2.24b}$$

$$ik_x\mathbf{H}_y = -i\omega\varepsilon_0\varepsilon\mathbf{E}z \tag{2.24c}$$

A system of equations (2.23 and 2.24) is formed by the two independent solutions with different polarisation properties of the propagating wave[44, 45]. The first set of equations (2.23a-c) comprise only $\mathbf{H}_x, \mathbf{H}_z$ and $\mathbf{E}_y$ while the second set (2.24a-c) consists of $\mathbf{E}_x, \mathbf{E}_z$ and $\mathbf{H}_y$. The first equations correspond to nonzero $\mathbf{H}_x, \mathbf{H}_z$ and $\mathbf{E}_y$ with zero $\mathbf{E}_x, \mathbf{E}_z$ and $\mathbf{H}_y$, (2.23a-c), this set is known as transverse electric (TE or s) modes. The second set corresponds to a nonzero $\mathbf{E}_x, \mathbf{E}_z$ and $\mathbf{H}_y$ with zero $\mathbf{H}_x, \mathbf{H}_z$, and $\mathbf{E}_y$, (2.24a-c), this set is called transverse magnetic (TM or p) modes.

For the TE modes, equations (2.23 and 2.24) can be simplified to obtain the following:

$$\mathbf{H}_{\mathrm{x}} = \mathrm{i}\frac{1}{\omega\mu_0}\frac{\partial \mathbf{E}_{\mathrm{y}}}{\partial \mathrm{z}} \quad [A/m] \tag{2.25a}$$

$$\mathbf{H}_{\mathrm{z}} = \frac{\mathrm{k}_x}{\omega\mu_0}\mathbf{E}_{\mathrm{y}} \quad [A/m] \tag{2.25b}$$

and by using (2.25) in (2.15), the corresponding wave equation for TE mode can be deduced;

$$\frac{\partial^2 \mathbf{E}_{\mathrm{y}}}{\partial \mathrm{z}^2} + \left(\left(\frac{\omega}{\mathrm{c}}\right)^2 \varepsilon - {\mathrm{k}_{\mathrm{x}}}^2\right)\mathbf{E}_{\mathrm{y}} = 0 \tag{2.26}$$

Similarly, for TM modes, equations (2.23 and 2.24)) can be reduced and yield the following:

$$\mathbf{E}_{\mathrm{x}} = -\mathrm{i}\frac{1}{\omega\varepsilon_0\varepsilon}\frac{\partial \mathbf{H}_{\mathrm{y}}}{\partial \mathrm{z}} \quad [V/m] \tag{2.27a}$$

$$\mathbf{E}_{\mathrm{z}} = -\frac{\mathrm{k}_{\mathrm{x}}}{\omega\varepsilon_0\varepsilon}\mathbf{H}_{\mathrm{y}} \quad [V/m] \tag{2.27b}$$

where equation (2.27) can be used in (2.16) to produce a TM wave equation as follow;

$$\frac{\partial^2 \mathbf{H}_{\mathrm{y}}}{\partial \mathrm{z}^2} + \left(\left(\frac{\omega}{\mathrm{c}}\right)^2 \varepsilon - {\mathrm{k}_{\mathrm{x}}}^2\right)\mathbf{H}_{\mathrm{y}} = 0 \tag{2.28}$$

After getting the TM and TE modes equations, we can now analyse surface plasmon polariton at the flat interface between a metal and a dielectric medium. Figure 2.2 depicts a schematic of a simple system used to investigate SPP modes at a single flat interface between a dielectric medium ($\mathrm{z} > 0$) with a positive dielectric constant ε_1 (a non-absorbing dielectric spacer) and a conducting medium ($\mathrm{z} < 0$) with a complex dielectric function $\varepsilon_2(\omega)$. As a condition for SPP mode to exist at the interface, the real permittivity of conducting medium needs to be negative ($\mathrm{Re}[\varepsilon_2(\omega)] < 0$) and much larger than the imaginary part, $\mathrm{Im}[\varepsilon_2(\omega)]$[44, 46].The permittivity of a dielectric medium is always positive.

Herein, we are only concerned with the solution of wave propagating/confined at the interface ($\mathrm{z} = 0$) between metal and dielectric with evanescent decay of the field in the transverse z-direction.

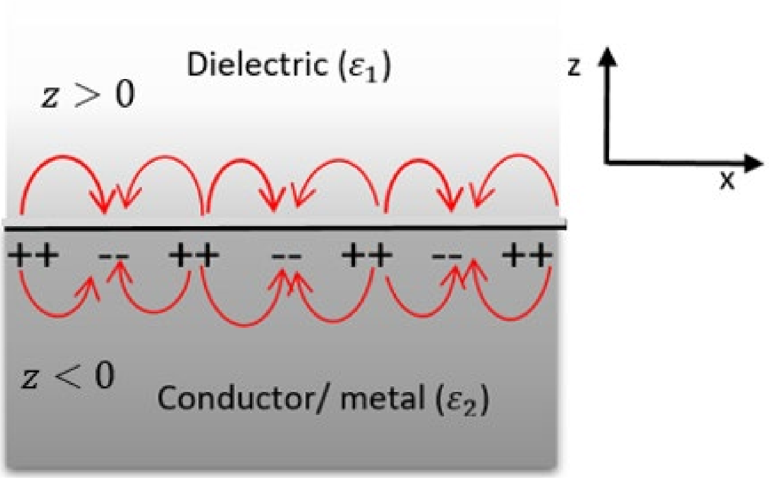

Figure 2.2. A sketch of collective oscillating charges at the interface between a dielectric and conductor (generation of surface plasmon).

In order to investigate SPP modes excitation, an appropriate polarisation is required. Therefore, we need to inspect whether we can use TM or TE polarisation to explore the propagating SPP modes at the interface between a conductor and a dielectric medium.

2.3. Exploring the excitation of surface plasmon polariton mode in a planar interface with TE and TM waves

Let us start with the solutions of TE mode for EM waves. By considering a flat interface as the one described in Figure 2.2 for a wave propagating along the x-direction, the equations (2.25) can be solved in both mediums ($z < 0$ and $z > 0$). We take the electric-field component in the y-direction to be $\mathbf{E}_{yi}(z) = \mathbf{E}_{01} e^{ik_{xi}x - k_{zi}z}$ (i=1, 2 for the medium 1 and 2).

For the top medium in the dielectric spacer ($z > 0$), the wave can be represented by (2.29).

$$\mathbf{E}_{y1}(z) = \mathbf{E}_{01} e^{ik_x x - k_{z1} z} \tag{2.29a}$$

$$\mathbf{H}_{x1}(z) = -i\mathbf{E}_{01} \frac{k_{z1}}{\omega\mu_0} e^{ik_x x - k_{z1} z} \tag{2.29b}$$

$$\mathbf{H}_{z1}(z) = \mathbf{E}_{01} \frac{k_x}{\omega\mu_0} e^{ik_x x - k_{z1} z} \tag{2.29c}$$

For the EM wave in the second medium in the metal ($z < 0$), the following can be deduced:

$$\mathbf{E}_{y2}(z) = \mathbf{E}_{02} e^{ik_x x + k_{z2} z} \tag{2.30a}$$

$$\mathbf{H}_{x2}(z) = i\mathbf{E}_{02}\frac{k_{z2}}{\omega\mu_0}e^{ik_x x + k_{z2}z} \tag{2.30b}$$

$$\mathbf{H}_{z2}(z) = \mathbf{E}_{02}\frac{k_x}{\omega\mu_0}e^{ik_x x + k_{z2}z} \tag{2.30c}$$

Also, expression (2.26) can be modified and become;

$$k_{zi}^2\mathbf{E}_{yi} + (k_0^2\varepsilon_i - k_x^2)\mathbf{E}_{yi} = 0 \tag{2.31}$$

with $\frac{\partial^2\mathbf{E}_{yi}}{\partial z^2} = k_{zi}^2\mathbf{E}_{yi}$.

Consequently, for $z > 0$ we get,

$$\left(k_{z1}^2 + (k_0^2\varepsilon_1 - k_x^2)\right)\mathbf{E}_{y1} = 0 \tag{2.32}$$

whereas, for $z < 0$ we obtain,

$$\left(k_{z2}^2 + (k_0^2\varepsilon_2 - k_x^2)\right)\mathbf{E}_{y2} = 0 \tag{2.33}$$

Since $\mathbf{E}_{yi} \neq 0$, therefore we can simplify (2.32) and (2.33) as follows;

$$k_{z1}^2 = k_x^2 - k_0^2\varepsilon_1 \tag{2.34a}$$

$$k_{z2}^2 = k_x^2 - k_0^2\varepsilon_2 \tag{2.34b}$$

From equations (2.29) and (2.30), the continuity relation of $\mathbf{H}_x$ at the interface ($\mathbf{H}_{x1}(z) = \mathbf{H}_{x2}(z)$) leads us to the following:

$$\mathbf{E}_{01}k_{z1} + \mathbf{E}_{02}k_{z2} = 0 \tag{2.35}$$

For the case where $\mathbf{E}_{01} = \mathbf{E}_{02}$,

$$\mathbf{E}_{01}(k_{z1} + k_{z2}) = 0 \tag{2.36}$$

Here $\mathbf{E}_{01}$ and $\mathbf{E}_{02}$ defined the maximum electric field intensity in dielectric and metal, respectively.

A condition for the confinement of SPP mode at the interface ($z = 0$) requires both positive wavevectors in dielectric ($\mathrm{Re}[k_{z1}] > 0$) and in metal ($\mathrm{Re}[k_{z2}] > 0$)[44]. From equation (2.36), this condition is only fulfilled when $\mathbf{E}_{01} = \mathbf{E}_{02} = 0$. This implies that the fields in equation (2.29-2.30) will become zero. Consequently, TE polarisation cannot excite surface polariton modes at a planar interface between a metal and a dielectric[44, 46].

Next, we explore the excitation of surface modes with TM polarisation. Similarly, we consider a flat interface described in Figure 2.2 for a wave propagating in the x-direction and solve the equations (2.27) for both half-spaces, namely, $z < 0$ and $z > 0$. We also define the magnetic field component in the y-direction to be $\mathbf{H}_{yi}(z) = \mathbf{H}_{0i}e^{ik_x x - k_{zi}z}$ (i=1, 2 for the medium 1 and 2).

For $z > 0$, equation (2.27) can be modified to obtain (2.37);

$$\mathbf{H}_{y1}(z) = \mathbf{H}_{01}e^{ik_x x - k_{z1}z} \tag{2.37a}$$

$$\mathbf{E}_{x1} = i\frac{k_{z1}}{\omega\varepsilon_0\varepsilon_1}\mathbf{H}_{y1}(z) \tag{2.37b}$$

$$\mathbf{E}_{z1} = -\frac{k_x}{\omega\varepsilon_0\varepsilon_1}\mathbf{H}_{y1}(z) \tag{2.37c}$$

while for $z < 0$, it can be modified to the following expressions;

$$\mathbf{H}_{y2}(z) = \mathbf{H}_{02}e^{ik_x x + k_{z2}z} \tag{2.38a}$$

$$\mathbf{E}_{x2} = -i\frac{k_{z2}}{\omega\varepsilon_0\varepsilon_2}\mathbf{H}_{y2}(z) \tag{2.38b}$$

$$\mathbf{E}_{z2} = -\frac{k_x}{\omega\varepsilon_0\varepsilon_2}\mathbf{H}_{y2}(z) \tag{2.38c}$$

The continuity relation for tangential components of the field suggests that, $\mathbf{E}_{x1} = \mathbf{E}_{x2}$ and $\mathbf{H}_{y1} = \mathbf{H}_{y2}$, yield to the following expressions:

$$i\frac{k_{z1}}{\omega\varepsilon_0\varepsilon_1}\mathbf{H}_{y1}(z) = -i\frac{k_{z2}}{\omega\varepsilon_0\varepsilon_2}\mathbf{H}_{y2}(z) \tag{2.39a}$$

$$\frac{k_{z1}}{\varepsilon_1} = -\frac{k_{z2}}{\varepsilon_2} \tag{2.39b}$$

As earlier discussed, to maintain SPP mode at the interface ($z = 0$), the following need to be satisfied $(\mathrm{Re}[k_{z1}] > 0)$ and in metal$(\mathrm{Re}[k_{z2}] > 0)$. This also is confirmed by equation (2.39b), where we need the two mediums to be with opposite signs of real electric permittivity for that condition to remain valid. For example, a dielectric medium with $(\mathrm{Re}[\varepsilon_1] > 0)$ and a conductor (metal) with $(\mathrm{Re}[\varepsilon_2] < 0)$.

Using the same condition as in TE mode derivation, one can manipulate (2.28) for TM modes to find an equivalent equation to (2.34a and 2.34b).

By combining equations (2.34) and (2.39b), we can realise the expression (2.40), which describes the dispersion relation of the surface wave at the flat interface between a dielectric and conducting medium.

$$\mathrm{k_x} = \mathrm{k_0}\sqrt{\frac{\varepsilon_1\varepsilon_2}{(\varepsilon_2+\varepsilon_1)}} \qquad (2.40)$$

where $\mathrm{k_0} = \frac{\omega}{c}$ represents wavevector of light in the free space. For the complete derivation of equation (2.40), see Appendix A.

According to (2.40), TM polarised EM wave can be used to excite surface mode at the planar interface.

In the next section, we analyse the dispersion relation of the surface plasmon polariton mode supported at the conductor-dielectric planar interface. We use silver as a conductor and air as a dielectric medium.

2.4. Dispersion of surface plasmon polariton at the dielectric- metal interface

Much about the physics of SPP modes can be understood by analysing the dispersion relation (frequency dependence of the in-plane wavevector of SPP modes) of these modes (2.40). For simplicity of notation, we replace $\mathrm{k_x}$ by $\mathrm{k_{spp}}$ to describe the wavevector of surface plasmon polariton $\left(\mathrm{k_{SPP}} = \mathrm{k_0}\sqrt{\frac{\varepsilon_1\varepsilon_2}{(\varepsilon_2+\varepsilon_1)}}\right)$ propagating along x-direction of the interface of a conductor and dielectric.

Herein we take silver and air interface (Figure 2.3) as a case study. In the later sections of this chapter, we will extend this theory to the dispersion relation of surface phonon and surface plasmon polaritons supported in silicon carbide and graphene materials.

The dielectric function of silver $\varepsilon_2(\omega)$ can be calculated using the Drude model (2.41)[44].

$$\varepsilon_2(\omega) = \left(1 - \frac{{\omega_p}^2}{(\omega^2 + i\gamma\omega)}\right) \qquad (2.41)$$

where ω_p, and γ define the plasma frequency and damping constant. In our calculations, we used $\omega_p = 7.90$ eV and $\gamma = 0.06$ eV from[47]. Figure 2.3b shows the calculated negative real and positive imaginary permittivity of silver.

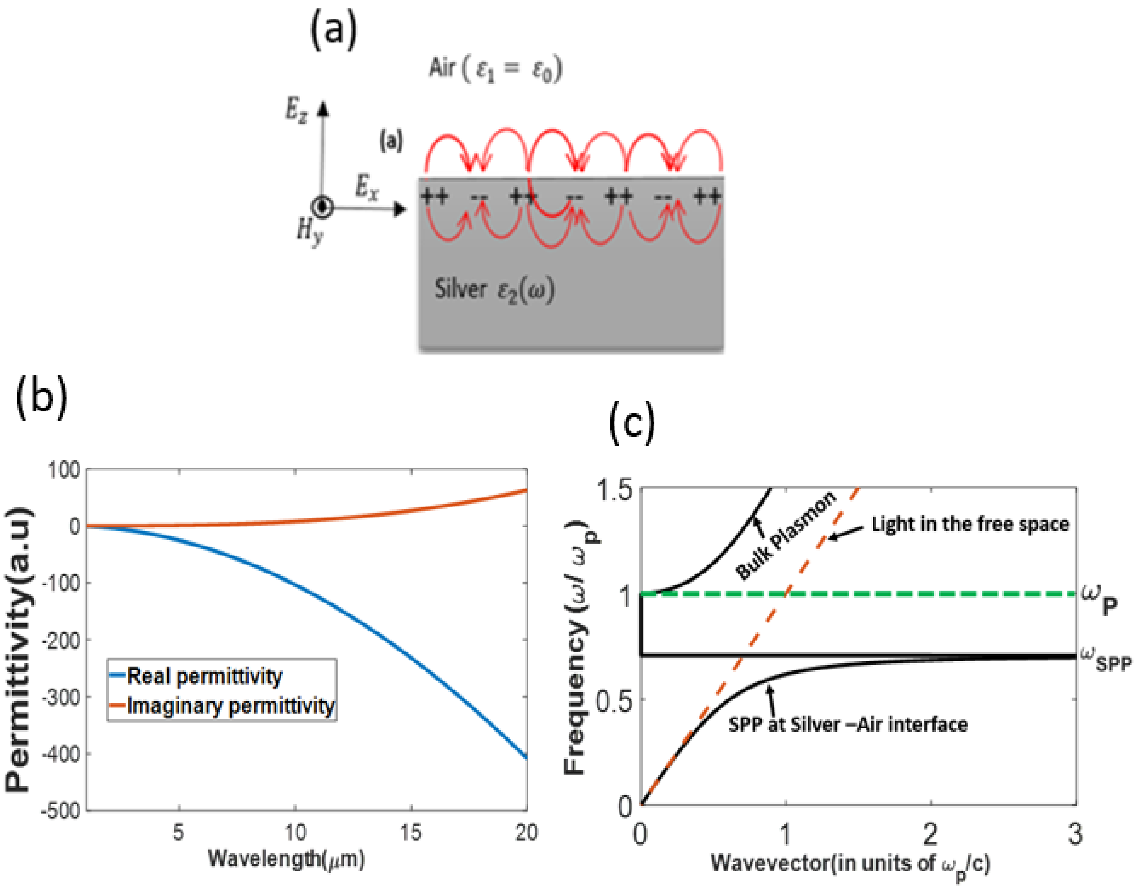

Figure 2.3. (a) A schematic showing SPP mode excited at the flat interface between air and silver, (b) the calculated permittivity (real and imaginary) of silver, calculated using equation (2.41). (c) The calculated dispersion relation of air-silver interface compared with the dispersion of light propagating in the free space. The horizontal solid black line in (c) denotes the surface plasmon polariton frequency (ω_{SPP}), whereas the discontinuous green lines indicate the position of plasma frequency (ω_p). Note, the frequency (ω) in the y-axis is normalised to the plasma frequency (ω_p), while wavevector in the x-axis is normalised to ω_p/c.

As shown in Figure 2.3c, at low frequencies (for small wavevectors), the dispersion curve of SPP mode in the air-silver approaches that of light in the free space, and the waves exist several wavelengths into the dielectric space[44, 47]. Many researchers describe these characteristics as grazing incidence waves, also defined as Sommerfeld-Zenneck waves[48]. At high frequency, the wavevector of SPP is significantly larger than the wavevector of light in the free space ($k_{spp} \gg k_0$). This indicates that for an equal angular frequency, the wavevector of SPP modes is always much larger than the wavevector of light in free space ($k_{SPP} > k_0$), leading to the so-called momentum mismatch ($\hbar k_{SPP} > \hbar k_0$) between light travelling through air and of SPP at the surface of the silver. Thus, this needs to be overcome for light to be coupled with SPP.

It is worth noting that surface plasmon frequency (ω_{spp}) sets the upper limit where surface plasmon polariton excitation can take place[46, 47]. Expression for ω_{spp} can be derived from relation (2.41), when the damping factor of the free oscillating electrons in a conductor is considerably negligible ($\gamma \approx 0$). This implies that imaginary permittivity be zero (no absorption losses), and frequency-dependent permittivity of metal is equal to the dielectric constant of dielectric material but with opposite sign ($\varepsilon_2 = -\varepsilon_1$)[46].

By solving (2.41) with the stated conditions, we get the following expression for the SPP mode resonance frequency;

$$-\varepsilon_1 = 1 - \frac{{\omega_p}^2}{{\omega_{SPP}}^2} \qquad (2.42a)$$

$$\omega_{spp} = \frac{\omega_p}{\sqrt{\varepsilon_1 + 1}} \qquad (2.42b)$$

Using relation (2.42b) for the air-silver system, we can calculate $\omega_{spp} = 1364$ THz (~ 220 nm), which corresponds to $\frac{\omega}{\omega_p} = 0.71$ from the normalised frequency in Figure 2.3c (horizontal solid black line). It is also worth mentioning that at ω_{spp} the wavevector of SPP tends to infinity $\left(k_{spp} \rightarrow \infty\right)$ since $\varepsilon_2 = -\varepsilon_1$, and thus the corresponding wavelength tends to zero $\left(\lambda_{spp} \rightarrow 0\right)$. This is what makes SPP an exciting phenomenon for subwavelength confinement of light, particularly in high-resolution microscopy[49].

Furthermore, at the frequencies beyond the plasma frequency (ω_p) (spectrum above the green horizontal dash line in Figure 2.3c), metals support volume plasmon, also called the bulk plasmon[44, 46, 50].

Generally, SPP modes also exhibit damping, which is described by propagation length (L_{SPP}). It is related to the ohmic losses in metals and can be determined from imaginary permittivity (Figure 2.3b). Consequently, the energy contained in SPP modes considerably drops as they propagate along the interface. If one intends to fabricate plasmonic devices, the propagation length set the upper limit of the size of the intended devices [47]. The equation for propagation length of SPP mode can be obtained from the imaginary component of its wavevector (k''_{SPP}).

$$L_{SPP} = \frac{1}{2k''_{SPP}} \tag{2.43}$$

An imaginary component for the SPP modes' wavevector can be deduced from relation (2.40) to obtain the following[46, 47].

$$k''_{SPP} = k_0 \frac{\varepsilon''_2}{2(\varepsilon'_2)^2}\left(\frac{\varepsilon'_2\varepsilon_1}{\varepsilon'_2 + \varepsilon_1}\right)^{\frac{3}{2}} \tag{2.44}$$

ε'_2 and ε''_2 denote real and imaginary electric permittivity of a conductor (silver), respectively.

We can put together (2.43) and (2.44) to get the expression for the propagation length of the surface plasmon[46].

$$L_{SPP} = \lambda_0 \frac{(\varepsilon'_2)^2}{2\pi\varepsilon''_2}\left(\frac{\varepsilon'_2 + \varepsilon_1}{\varepsilon'_2\varepsilon_1}\right)^{\frac{3}{2}} \tag{2.45}$$

From equation (2.45), it can be seen that propagation length is a multiple of the wavelength of light in the free space. For low loss metals and when a condition for $|\varepsilon'_2| \gg |\varepsilon_1|$ is fulfilled[47], the expression for propagation length of SPP mode can be simplified as,

$$L_{SPP} = \lambda_0 \frac{(\varepsilon'_2)^2}{2\pi\varepsilon''_2} \tag{2.46}$$

Equation (2.46) suggests that long propagation length requires a conductor/metal with very small imaginary permittivity and large negative real permittivity[47]. Usually, the propagation length of SPP mode at the interface between a dielectric and metal vary from tens to hundreds of micrometres. In Figure 2.4a, we report the calculated propagation length of SPP modes at the air-silver interface.

Lastly, we need to know how the fields associated with SPP modes would penetrate the medium bounding the interface (air-silver), and this is analysed from the parameter known as penetration depth (δ_{zi}). The penetration depth of the fields describes the distance over which fields intensity decay to $1/e$ of their maximum intensity at the interface (z=0). Both expressions for penetration depth into the dielectric (δ_{z1}) and metal (δ_{z2}) can be obtained by manipulating expressions (2.39b and 2.40). Also, it is given by the inverse of the imaginary part of the wavevector in the z-direction ($\delta_{zi} = \frac{1}{k''_{zi}}$)[46, 47, 51].

$$\delta_{z1} = \frac{1}{k_0}\sqrt{\left|\frac{\varepsilon'_2 + \varepsilon_1}{\varepsilon_1^2}\right|} \tag{2.47}$$

$$\delta_{z2} = \frac{1}{k_0}\sqrt{\left|\frac{\varepsilon'_2 + \varepsilon_1}{\varepsilon'^2_2}\right|} \tag{2.48}$$

δ_{z1} and δ_{z2} symbolise the penetration depth in dielectric (air) and a conductor (silver), respectively.

In Figure 2.4b-c, the calculated penetration depths into silver and air as the function of wavelength are shown for the air-silver material system.

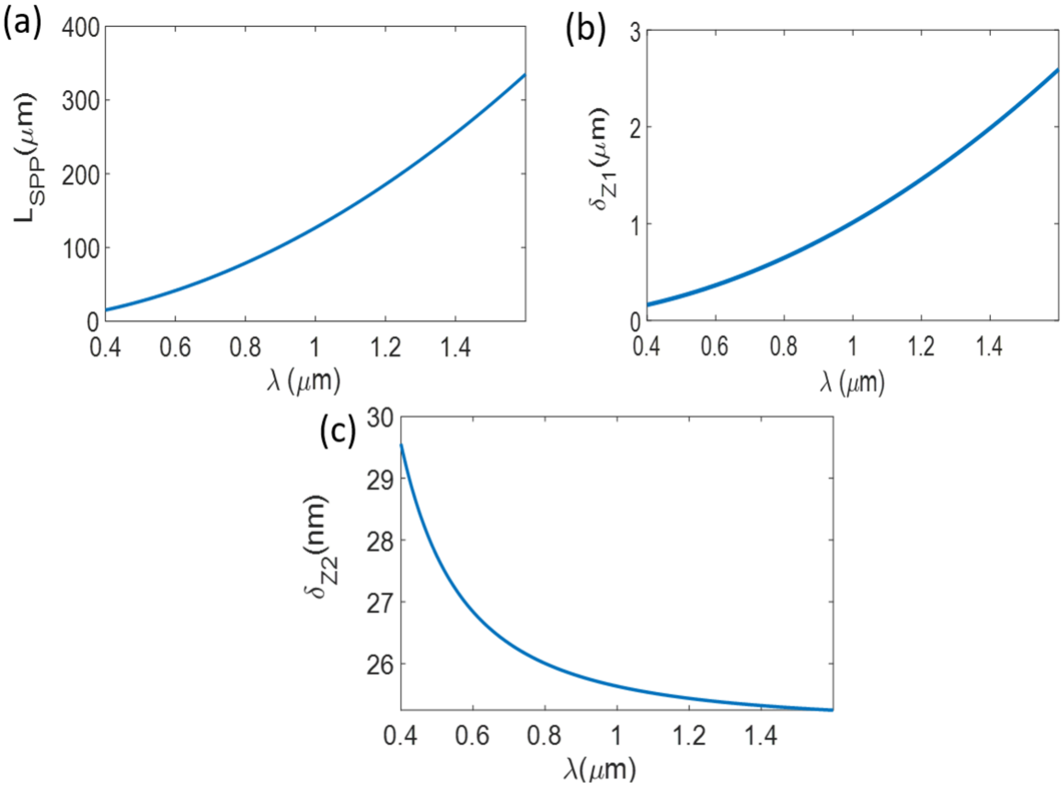

Figure 2.4. (a) Propagation length of SPP modes at the air/silver interface. (b) Penetration depth into dielectric (air), c) penetration depth into metal (silver). We performed the calculations using ω_p = 7.90 eV and γ = 0.06 eV from[47].

At the lower wavelength (visible spectrum) below ~ 1 μm, the penetration depth (δ_{z1}) into dielectric (air) is relatively equal to the wavelength of light in the free space while it is significantly larger for longer wavelengths, Figure 2.4b. This happens because metal behaves like a perfect conductor, and thus the wavevector of SPP modes gets closer to those of light in the free space (see the dispersion curve in Figure 2.3c), causing weak confinement of the fields to the surface[47]. The penetration depth into the dielectric provides information on how the SPP modes would be affected by changes in a refractive index. It also defines the required air gap thickness (coupling medium) for optimal coupling of evanescent fields into SPP modes in Otto prism configuration. This will be discussed further in section 5.3.1of chapter 5.

Figure 2.4c shows the calculated penetration depth into a conductor (silver) δ_{z2} with a maximum value of ~29.5 nm. Generally, the maximum value of δ_{z2}, can go up to $\sim 50\text{nm}$ at the visible frequency regime for metals, and it provides information about the thickness of metal films needed to excite SPP modes in Kretschmann prism configuration[46, 47]. It also indicates the required measures for the feature sizes of metal, allowing control of SPP modes in plasmonic devices[47, 52]. As shown in Fig.2.4c, δ_{z2} is significantly smaller than the free space light wavelength, indicating strong SPP mode confinement in silver at the visible frequency regime.

As hitherto indicated, the SPP modes excited at a flat air-silver interface have a larger wavevector than the light in the free space, which we referred to as momentum mismatch. In the following section, we discuss how to overcome this issue.

2.5. Excitation of surface plasmon polariton at a dielectric- metal interface

For a given light of frequency ω, a wavevector $k_0 = \frac{\omega}{c}$ can be increased by a certain value Δk using prism coupler in the process known as coupling via attenuated total internal reflection [53]. It is also possible to overcome the deficiency between the momentum of light and SPP mode using the gratings coupler, where the periodicity of gratings gives the Δk. Another method consists of scattering from engineered defects on the surface, such as subwavelength holes or asperities [52, 54, 55]. Such defects can enable momentum matching between free-space light and surface plasmons by scattering the incident light, which leads to the generation of localised SPP modes [44, 54]. SPP modes can also be excited by coupling free-space light to the nanoparticles of a diameter similar to or larger than the wavelength of incident light through the process known as Mie scattering[44, 56].

Finally, other techniques for launching and analysing SPP mode include scattering-type scanning near field optical microscopy (s-SNOM), high energy electron beam, and fluorescence imaging using emitters such as fluorescent molecules or quantum dots[44, 50]. However, in this thesis, we limit our discussions on the coupling with a prism and grating coupler.

2.5.1. Excitation with a prism through attenuated total internal reflection

Generally, the momentum and energy of incident light have to be matched to that of SPP modes, and a component of the field of the incoming wave should be oriented in the same direction as the oscillating surface charge to have incident light coupled with SPP mode.

In Figure 2.5a, a diagram for excitation of SPP modes with plane incident wave using prism method is given. The light incident inside prism with refractive index $n = \sqrt{\varepsilon_p}$ ($\varepsilon_p > 1$) and its wavevector becomes $k_P = \frac{\omega}{c}\sqrt{\varepsilon_p}$ instead of $k_0 = \frac{\omega}{c}$ in the free space. where ε_p stands for permittivity of prism and k_P represents the wavevector of light in the prism. If we project it along the interface plane ($x -$ the direction of propagation), we can get the following;

$$k_{px} = \frac{\omega}{c}\sqrt{\varepsilon_p}\sin\theta_i \tag{2.49}$$

Therefore, matching the wavevector of light travelling through the prism and SPP at the air-metal interface requires the following relation to be fulfilled:

$$k_{spp} = k_{px} = \frac{\omega}{c}\sqrt{\varepsilon_p}\sin\theta_i \tag{2.50}$$

where θ_i represents the angle of incident light inside the prism (see Figure 2.5a). Once the condition in (2.50) is fulfilled, light (evanescent fields) couples with SPP modes at a dielectric (lower refractive index medium)-conductor interface (Figures 2.5b) or conductor-dielectric (Figures 2.5c) for the two different coupling configurations via the tunnelling effect.

Moreover, this technique requires total internal reflection of light at the prism and dielectric interface; therefore, the angle of incidence inside the prism (θ_i) should be greater than the critical angle (θ_c), where $\theta_c = \sin^{-1}\left(\frac{\sqrt{\varepsilon_d}}{\sqrt{\varepsilon_p}}\right)$, with ε_d and ε_p representing permittivity of lower density dielectric medium and prism, respectively.

However, it should be noted that wavevector matching takes place at a certain angle beyond critical ($\theta_i > \theta_c$). This angle, which is also defined as SPP resonance angle (θ_{spp})[50], can be calculated from the condition set in (2.50) using (2.40) as follows;

$$\theta_{spp} = \sin^{-1}\left(\frac{k_{spp}}{k_0\sqrt{\varepsilon_p}}\right) \cong \sin^{-1}\left(\frac{1}{\sqrt{\varepsilon_p}}\sqrt{\frac{\varepsilon_2\varepsilon_d}{\varepsilon_2+\varepsilon_d}}\right) \tag{2.51}$$

where $\varepsilon_d = \varepsilon_1$ in the equation (2.40).

Equation (2.51) implies that the incident light will have its wavevector at the resonance angle matching the wavevector of SPP mode of the same frequency.

Figure 2.5 depicts the two geometry configurations commonly used for prism couplings. The first geometry, depicted in Figure 2.5b, was proposed by Andreas Otto[57]. His configuration consists of a higher index prism separated from the conductor by a lower index dielectric material, typically an air gap. Incident light in prism undergoes total internal reflection at the interface between prism and air interface when $\theta_i \geq \theta_c$, and through the tunnelling effect, SPP mode gets excited at the air-conductor interface[57, 58]. Otto prism configuration is highly recommended when direct contact with the sample being measured is undesirable, particularly for surface quality characterisation[44, 50].

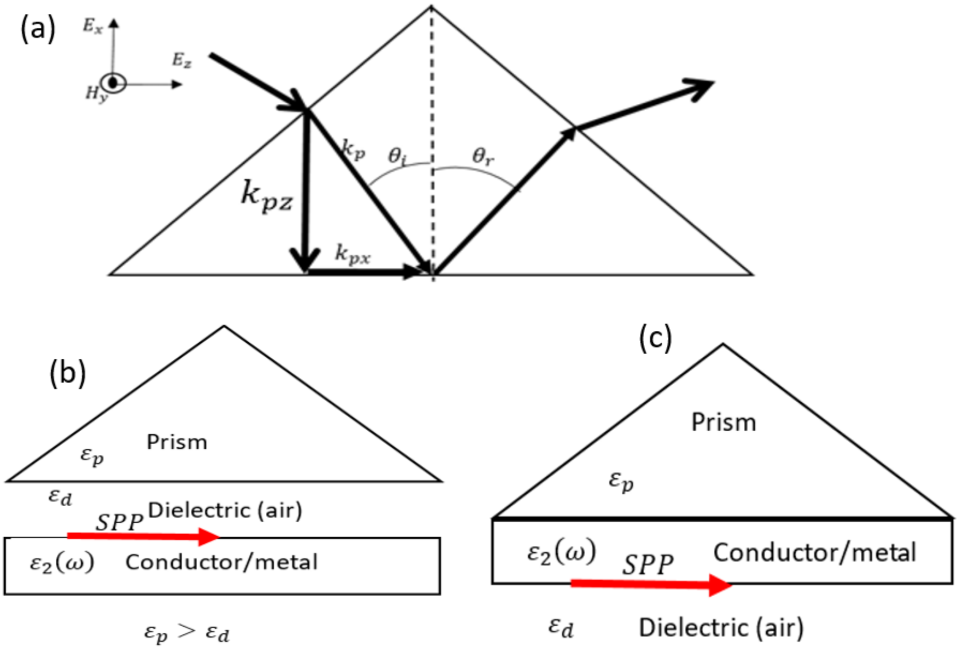

Figure 2.5. (a) Schematic of prism coupler configurations[46]. (b) Andreas Otto configuration, (c) Kretschmann- Raether configuration.

The second geometry is known as Kretschmann- Raether method[53, 59, 60], in which a metal (conductor) film is deposited on a high index prism while the other side of the conductor is covered by a lower index medium (e.g., air). Incident light travels through a prism at $\theta_i \geq \theta_c$ and tunnels through the metal film to excite SPP modes at the interface between metal and air (see Figure 2.5c).

In Figure 2.6, we report the dispersion relation of light propagating through free space and the effect of prism in overcoming the wavevector mismatch issue. As shown in Figure 2.6a, the light travelling through free space has a smaller wavevector than the wavevector of SPP in silver, and the disparity 'Δk' between their wavevector is more prominent when the incident free-space light is at an oblique angle (see solid yellow line in Figure 2.6a).

On the other hand, if light travels through a higher index prism (e.g., diamond n = 2.4) with $\theta_i > \theta_c = \theta_{spp}$, the wavevector k_{px} increases to match k_{spp} at a particular frequency near the surface plasmon frequency (ω_{spp}), see this in Figure 2.6a (the solid green line where a missing wavevector Δk is gained by passing light into diamond at 45°).

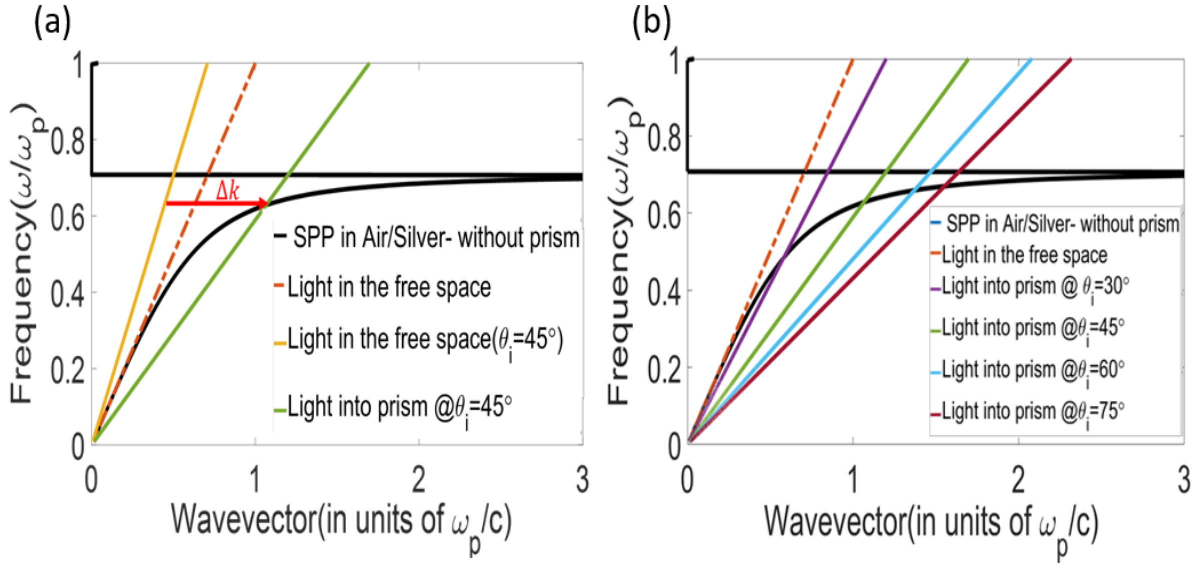

Figure 2.6. (a) The dispersion of light travelling in the different mediums compared to the dispersion of SPP modes in the air-silver system. Light in free space (broken red line), light propagating in free space at θ_i= 45° (solid yellow line), wavevector of SPP in silver (solid black curve), wavevector of light propagating into a diamond (n = 2.4) at θ_i = 45° (solid green line), a red arrow indicates a missing wavevector that can be generated via prism coupling. (b) Change in wavevector of incident light in air and diamond for the different incident angles. Data for silver are ω_p = 7.90 eV and γ = 0.06 eV[47].

The incidence angle of the light within the prism is another crucial parameter to consider to excite SPP mode using a prism coupler. From Figure 2.6b, one can see that for different incident angles, the wavevector of light into prism crosses that of SPP modes at different frequencies, showing the importance of the angle of incident light to the excitation SPP mode at the flat interface system.

2.5.2. Excitation with grating coupler

The disparity between the wavevector of SPPs and incident plane wave can also be overcome by patterning the surface of the conductor (metal) with the periodic structures in the form of grating with certain lattice constant (Λ). In Figure 2.7, a simple geometry for gratings is shown. When incident light hits a grating with a lattice constant Λ at an incident angle θ_i, in-plane wavevector changes by a factor of Δk_x. The following expression can be used to describe the in-plane wavevector.

$$k_{gx} = k_{0x} \pm m\Delta k_x \cong k_0\sqrt{\varepsilon_1}\sin\theta_i \pm m\frac{2\pi}{\Lambda} \qquad (2.52)$$

where k_{gx} and k_{0x} denotes in-plane wavevector of light at the grating grooves and in free space, respectively, while m $(1,2,3,\dots)$ is an integer number representing the diffraction order.

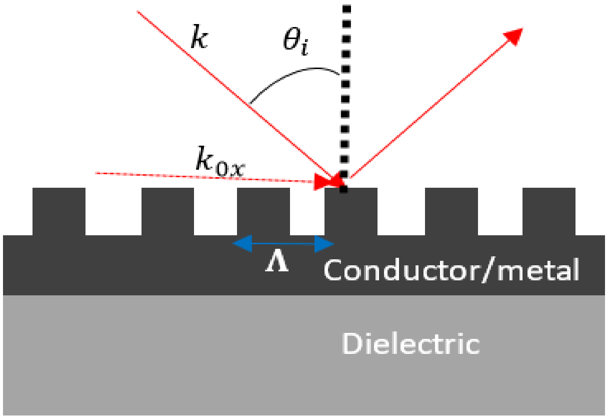

Figure 2.7. Schematic for excitation of SPPs mode with grating

For the grating coupling technique, the conservation of momentum is realised by equating the wavevector of SPP modes (2.40) with (2.52), and can be expressed by the following:

$$k_{spp} = k_0\sqrt{\varepsilon_1}\,\sin\theta_i \pm m\frac{2\pi}{\Lambda} = k_0\sqrt{\frac{\varepsilon_1\varepsilon_2}{(\varepsilon_2+\varepsilon_1)}} \qquad (2.53)$$

Unlike prism coupling, it is clear that the conservation of wavevector in grating coupling depends strongly on the lattice constant Λ and the value of m.

The plasmonics research has significantly advanced over the past few years, mainly in the visible and near-infrared (NIR) parts of the EM spectrum, where most of the metals hold their SPP resonances. There is also recent interest in the plasmonics works focusing on the surface polariton modes at the mid-infrared (MIR) to far-infrared (FIR) spectral ranges. Graphene and polar materials like SiC, GaAs, and hBN are the widely investigated alternative materials for MIR and FIR polaritons.

Hence, building from the fundamental theory of surface plasmon polariton excitation in the air-silver system, the rest of this chapter we discuss the fundamental theory and dispersion relation of surface plasmon and phonon polariton modes excited in graphene and SiC and their hybridisation in graphene/SiC system. In the next section, we start with a brief discussion on the electronic band structure of graphene.

2.6. Electronic band structure of graphene

The best way to introduce graphene is by talking about carbon, an essential material for the life and centre of all organic chemistry. Due to the flexible nature of carbon bonding, carbon-based systems display an unlimited number of different structures with a relatively large variety of physical properties resulting primarily from these structures' dimensionality[61].

Graphene is a two-dimensional (2D) material, one atom thick and an allotrope of carbon formed by SP^2 hybridised carbon atoms bonded together to form a hexagonal honeycomb lattice[62]. Graphene is considered a fundamental building block for other allotropes of carbon, such as fullerenes (0D), which are the molecule where carbon atoms are arranged in a spherical shape, carbon nanotubes (1D), and graphite (3D)[61].

Graphite, which is a three dimensional (3D) allotrope of carbon, was known since the discovery of a pencil in 1564[63], and its usage as a writing tool originated from the fact that graphite consists of the stack of graphene layers that are weakly connected by van der Waals forces[61]. Therefore, when one writes on a sheet of paper with a pencil, the graphene stacks get produced, from which graphene layers could be identified. Though graphene is a primary material for carbon allotropes, and it gets produced whenever someone writes with a pencil, it was only discovered in 2004[64]. The reasons were that nobody believed in graphene's existence in a free state and the lack of experimental instruments that can permit the study of one-atom-thick materials in the middle of the pencils rubble covering microscopic area[61, 64]. The flexible structure of graphene originates from its electronic properties.

The SP^2 hybridisation between S orbital and 2P orbitals yields a trigonal planar structure and the formation of a sigma (σ) bond between carbon atoms that are separated with 1.42Å. The robustness of the lattice structure for all carbon allotropes is due to the σ band. Due to Pauli's exclusion principle, the σ bands have a filled shell and form a deep valence band. The remaining unfilled P orbital, orthogonal to the planar structure, can form a covalent bond with neighbouring carbon atoms, creating a π band. Subsequently, as each P orbital contains one excess electron, therefore π band is half filled[61]. Traditionally, half-filled bands in transition elements played a vital role in the physics of firmly connected systems. Their strong tight-binding nature results in large Coulomb energies that lead to magnetism, collective effects, and insulating behaviour from the connecting gaps[65].

A unit cell of graphene can be represented by two lattice vectors, a_1 and a_2, as described in Figure 2.8a, which can geometrically be defined as follows,

$$\mathbf{a_1} = \frac{a}{2}\left(3, \sqrt{3}\right) \tag{2.54}$$

$$\mathbf{a_2} = \frac{a}{2}\left(3, -\sqrt{3}\right) \tag{2.55}$$

a = 1.42Å is the lattice constant lattice/distance between carbons to a carbon atom. The vectors reciprocal to the lattice vectors can be represented by (2.56) and (2.57).

$$\mathbf{b_1} = \frac{2\pi}{3a}\left(1, \sqrt{3}\right) \tag{2.56}$$

$$\mathbf{b_2} = \frac{2\pi}{3a}\left(1, -\sqrt{3}\right) \tag{2.57}$$

The two symmetric points K and K'at the corners of the Brillouin zone (BZ) are of significant importance for the physical properties of graphene (Figure 2.8b). These two points are known as the Dirac points, and their coordinates in momentum space can be described by (2.58);

$$\mathbf{K} = \left(\frac{2\pi}{3a}, \frac{2\pi}{3\sqrt{3}a}\right), \mathbf{K}' = \left(\frac{2\pi}{3a}, \frac{2\pi}{3\sqrt{3}a}\right) \tag{2.58}$$

The three closest neighbour vectors in space are defined by

$$\boldsymbol{\delta}_1 = \frac{a}{2}\left(1, \sqrt{3}\right),\ \boldsymbol{\delta}_2 = \frac{a}{2}\left(1, -\sqrt{3}\right), \boldsymbol{\delta}_3 = -a\,(1, 0) \tag{2.59}$$

While the other six-second closest neighbours are situated at $\boldsymbol{\delta}_1{}' = \pm\mathbf{a}_1$, $\boldsymbol{\delta}_2{}' = \pm\mathbf{a}_2, \boldsymbol{\delta}_3{}' = \pm(\mathbf{a}_2 - \mathbf{a}_1)$.

The electronic band structure of graphene reveals the conduction and valence band meeting at the Dirac point/a charge neutrality point characterised by a linear dispersion and a zero bandgap (see Figure 2.8c).

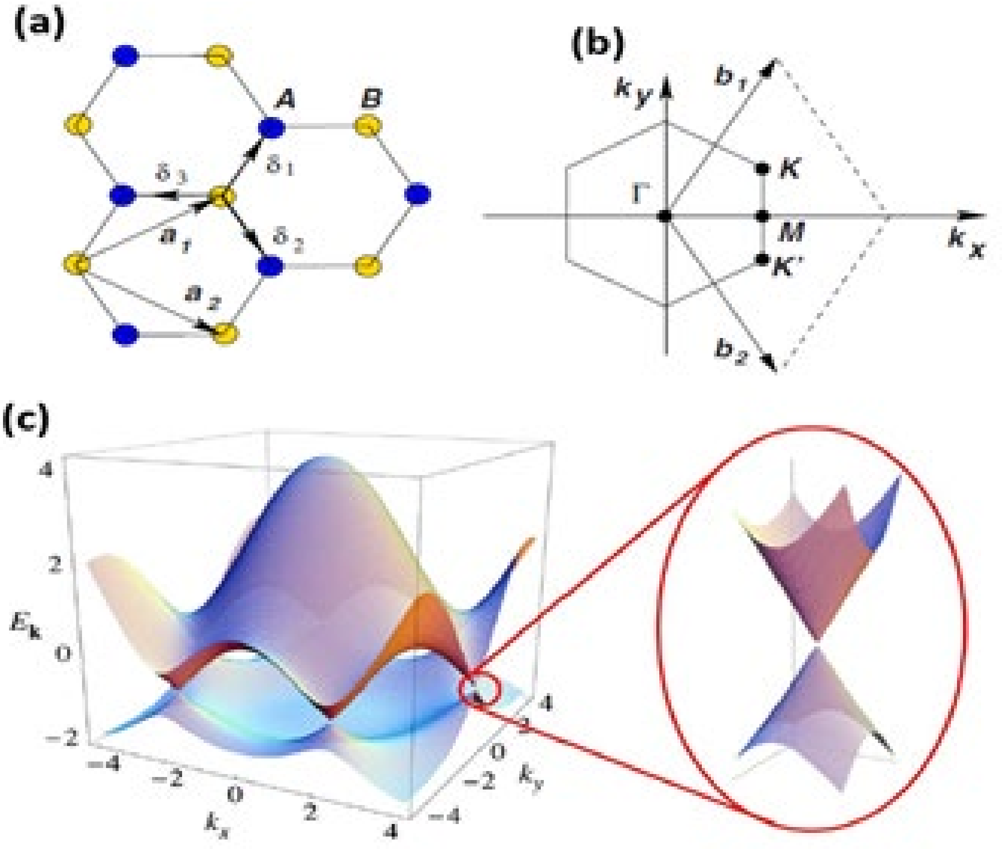

Figure 2.8. (a) Hexagonal (honeycomb) lattice representation of graphene zone (a_1 and a_2 depict the lattice unit vector while $\delta_{1,2\ \text{and} 3}$ describe the nearest neighbour vectors). (b) Brillouin zone where K and K′ points designate the location of Dirac cones. (c)Electronic dispersion/ energy bandgap of graphene showing the Dirac point, with t = 2.7 eV and t′ = -2t. Adapted with permission from [61]. Copyright ©2009 American Physical Society.

2.7. Surface plasmon in graphene

To study graphene plasmonics, it is worth starting by analysing its surface conductivity. The surface conductivity of graphene[66, 67] can be calculated using the well-known Kubo formalism[68, 69].

$$\sigma(\mu_c,\omega,T,\gamma) = -\frac{ie^2(\omega+i2\gamma)}{\pi\hbar^2}$$

$$\times\left[\frac{1}{(\omega+i2\gamma)^2}\int_0^\infty E\left(\frac{\partial f(E)}{\partial E}-\frac{\partial f(-E)}{\partial E}\right)dE - \int_0^\infty \frac{f(-E)-f(E)}{(\omega+i2\gamma)^2-4\left(\frac{E}{\hbar}\right)^2}dE\right] \quad (2.60)$$

with f(E) describing the Fermi distribution function, which is given by the following expression

$$f(E) = \left(1+e^{\left(\frac{E-\mu_c}{K_BT}\right)}\right)^{-1} \quad (2.61)$$

A simplification of equation (2.60) leads to two sets of equations (2.62) and (2.63), with one expressing intra-band (electron and phonon scattering) contributions, while the other stands for inter-band (bound electron) contributions[70, 71]:

$$\sigma_{intra} = \frac{2ie^2T}{\pi\hbar^2\,(\omega+i\tau^{-1})}\,ln\left[2cosh\left(\frac{\mu_c}{2T}\right)\right] \quad (2.62)$$

$$\sigma_{inter} = \frac{e^2}{4\hbar}\left[\frac{1}{2}+\frac{1}{\pi}arctan\left(\frac{\hbar\omega-2\mu_c}{2T}\right)-\frac{i}{2\pi}ln\frac{(\hbar\omega+2\mu_c)^2}{(\hbar\omega-2\mu_c)^2+(2T)^2}\right] \quad (2.63)$$

where μ_c designates chemical potential, T, and τ represent temperature and relaxation time, while k_B and $\hbar$ symbolise Boltzmann and reduced Plank constant, respectively.

The conductivity of graphene can be obtained by summing (2.62) and (2.63).

$$\sigma = \sigma_{intraband} + \sigma_{interband} \quad (2.64)$$

For graphene with a carrier density of $\sim 10^{12}\text{cm}^{-2}$ the intra-band contribution dominates the conductivity of graphene at MIR and FIR frequencies, while the inter-band contribution dominates graphene conductivity at the near-infrared (NIR) and visible regimes[72]. The effective permittivity of graphene ($\varepsilon_g(\omega)$) can be approximated from its conductivity[73], using equation (2.64) through the following:

$$\varepsilon_g(\omega) = \varepsilon_0 + \frac{i\sigma(\omega)}{\omega\Delta} \quad (2.65)$$

where Δ describes an effective thickness of the graphene layer.

Like conventional metal plasmonics, a TM polarised wave (2.28) can excite an SPP mode in graphene. By considering such a wave with the following field components (E_x, H_y, E_z), one can solve Maxwell's equations with appropriate boundary conditions to get the following relation for the dispersion of SPP in graphene[6, 74].

$$\frac{\varepsilon_d}{\sqrt{k_{spp}^2(\omega) - \varepsilon_d k_0^2}} + \frac{\varepsilon_m(\omega)}{\sqrt{k_{spp}^2(\omega) - \varepsilon_m(\omega) k_0^2}} = -i\frac{\sigma(\omega)}{\omega\varepsilon_0} \tag{2.66}$$

where $\sigma(\omega)$ represents the frequency-dependent conductivity of graphene (see Figure 2.9 for graphene sheet on a substrate $\varepsilon_m(\omega)$ and surrounded by a dielectric medium with permittivity ε_d).

Equation (2.66) can be solved to produce the following expression or the dispersion of SPP mode in graphene[6].

$$k_{spp}(\omega) = k_0 \frac{(\varepsilon_d + \varepsilon_m(\omega))\hbar\omega(1 + i(\tau\omega)^{-1})}{4\alpha\, E_F} \tag{2.67}$$

where $\frac{e^2}{4\pi\hbar c\, \varepsilon_0} \approx \frac{1}{137}$, is the fine structure constant. See complete derivation of equation (2.67) in Appendix B.

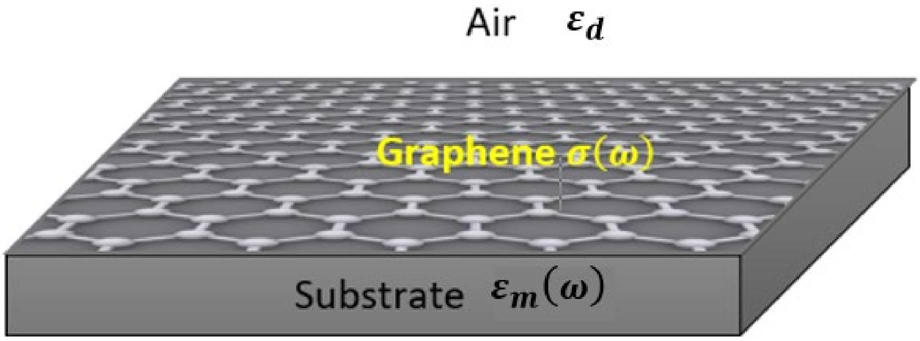

Figure 2.9. Graphene layer surrounded by air and a substrate of ε_d and $\varepsilon_m(\omega)$, respectively.

In the MIR and FIR spectral regions (~ 3 µm -300 µm), the intra-band transitions dominate the optical behaviour of graphene, causing it to act as a metallic film and support an SPP mode once the sufficient conditions for SPP excitation are fulfilled[43]. Thanks to the 2D nature of collective excitations of carriers in graphene, this SPP mode is confined significantly more than in conventional plasmonic materials, as the wavelength of graphene SPP mode can be much smaller than the wavelength of light at the same frequency[24]. Moreover, exceptional confinement of the SPP mode in graphene can be understood by comparing its dispersion with that of a thin layer of a doped semiconductor (e.g., InAs) of comparable ω_p. The SPP dispersion of a thin-film of InAs can be calculated using the following relation[75-77].

$$1+\frac{\varepsilon_1 k_{z,3}}{\varepsilon_3 k_{z,1}}=i\tan\left(k_{z,2}d\right)\left(\frac{\varepsilon_2 k_{z,3}}{\varepsilon_3 k_{z,2}}+\frac{\varepsilon_1 k_{z,2}}{\varepsilon_2 k_{z,1}}\right) \qquad 2.68$$

where d is the film thickness and $k_{z,n}=\left(\frac{\varepsilon_n\omega^2}{c^2}-k_{\parallel}\right)^{1/2}$ (n=1, 2, 3) is the longitudinal wavenumber of the SPP supported on the film and the surrounding medium and $k_{\parallel}\equiv k_{SPP}$. Using the assumption that $\frac{\varepsilon_2\omega^2}{c^2}\ll {k_{\parallel}}^2$[76], we can calculate and compare the dispersion of a 10-nm thick layer of a doped InAs to graphene.

Both graphene and InAs exhibit almost equivalent negative real permittivity values close to ω_p (Figure 2.10a). However, an apparent deviation can be noticed near this frequency in Figure 2.10b, where the wavevector for graphene's SPP is much larger than that of doped InAs near the plasma frequency (55.4 THz). It is worth restating that the plasma frequency sets the limit for the metallic behaviour of metals and doped semiconductors, and beyond this frequency, these materials do not support SPP modes (the green curve in Figure 2.10b). On the other hand, the dispersion curve of SPP in graphene is almost linear, with a larger wavevector than that of InAs at the frequencies around the InAs plasma's plasma frequency (see blue curve in Figure 2.10b). This suggests that SPP modes are confined more strongly in graphene than in doped InAs at these frequencies.

We also used the two figures of merit (FOMs)[78], to compare the performance of doped InAs against graphene qualitatively. The first FOM is associated with the propagation of an SPP mode ($FOM_{prop.}$), which is given by the propagation length (L_{SPP}) normalised to the wavelength(λ_{SPP}) of the surface plasmon polariton while the second is a measure of the vertical confinement ($FOM_{conf.}$) of SPP mode at the interface and can be calculated as the ratio between the penetration depth of SPP mode (δ_{SPP}) and the wavelength of an incident free-space light (λ_0).

$$FOM_{prop.}=\frac{L_{SPP}}{\lambda_{SPP}} \qquad (2.69)$$

$$\mathrm{FOM}_{\mathrm{conf.}} = \frac{\lambda_0}{\delta_{\mathrm{SPP}}} \tag{2.70}$$

In terms of propagation, InAs SPPs do exhibit a larger $\mathrm{FOM}_{\mathrm{prop.}}$ than graphene. It is worth noting that the relaxation time of $\tau = 88.5\ fs$ used in Figure 2.10c is low for graphene but reasonable enough to allow a sensible comparison of its dispersion with that of doped InAs.

Due to the higher polariton confinement of graphene, the 2D material is very promising for the fabrication of novel metamaterial-based devices and nanophotonic applications at the discussed spectral regions[6, 8, 10, 24, 74, 79-81].

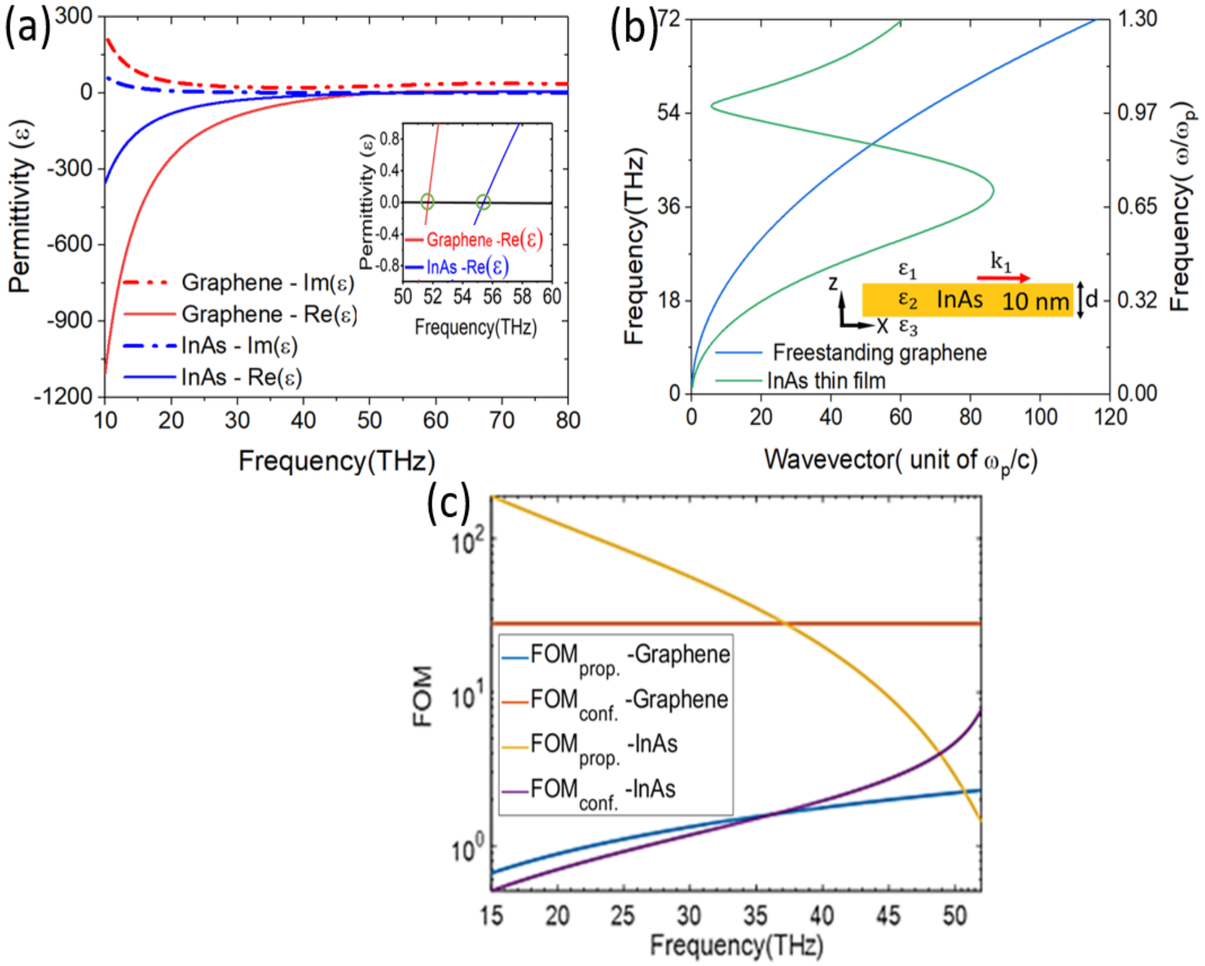

Figure 2.10. Dispersion relation of SPP in graphene compared with a doped InAs thin film. (a) The calculated permittivity inset shows the frequency where permittivity is near zero for graphene and InAs. For InAs, permittivity is zero at $\omega_{\text{p-InAs}}$ = 55.4 THz. (b) Dispersion relation of SPP modes in both materials. (c) FOM for propagation length and spatial confinement of SPP modes in graphene and doped InAs. The calculation for dispersion relations was performed using the equations (2.41) and (2.68) for the doped InAs and (2.65 & 2.67) for graphene. The epsilon near zero (ENZ) conditions are $E_F = \omega_{\text{p-InAs}}/2$= 27.7 THz (≈0.12 eV) and relaxation time τ = 88.5 fs for both materials.

2.8. Surface phonon polaritons in silicon carbide

While SPPs are derived from the coupling of coherent free-carrier oscillations with light, the collective ionic oscillations of a polar crystal enable the stimulation of SPhPs[4, 21]. These modes are analogous to SPPs and can be supported within the spectral region known as the Reststrahlen band[82, 83], which is bound between longitudinal (LO) and transverse optical phonon (TO) frequencies[84]. SPhP modes have been demonstrated in a wide variety of polar materials such as SiO_2[85], GaAs[86, 87], SiC[84, 88], hexagonal[89, 90] and cubic BN[91] , and revealed strong sub-diffraction field confinement with relatively low optical losses[21]. Moreover, due to the optical phonon nature of SPhP modes, they are resonant in the MIR to THz spectral ranges, a region of great interest for applications in thermal imaging and chemical spectroscopy. Particularly, SPhP modes have been reported with high resonance quality factors of up to 300 in the far-field and 400 in the nearfield with long lifetimes on the order of one to hundreds of picoseconds[92, 93], with a very recent record high-quality factor of 501 realised in hBN[94]. This is in comparison to SPPs, which feature quality factors typically on the order of 10, resulting from scattering lifetimes of tens to a few hundred femtoseconds[84, 95]. Thus, these effects identify polar dielectrics as low–loss materials than their SPP counterparts[4, 83, 84]. In the following section, we discuss the dispersion of SPhP modes using SiC as a case study.

2.8.1. Dispersion of surface phonon polariton in silicon carbide

In order to understand the physics associated with the excitation of SPhP modes in SiC, it is worthwhile to look back on the optical properties and phenomena that cause metals to support SPPs. Similar to metals, polar dielectric materials also exhibit high reflectivity and negative real part of the permittivity within the Reststrahlen band (Figure 2.11a-b)[4, 96]. The dielectric function of such polar materials thus deviates from Drude materials (e.g., metals and doped semiconductors) in that the negative permittivity is only observed within the Reststrahlen band, and thus is typically defined by the so-called TOLO formalism provided in equation (2.71):

$$\varepsilon(\omega) = \varepsilon_{\infty}\left(1 + \frac{\omega_{\mathrm{Lo}}^2 - \omega_{\mathrm{To}}^2}{\omega_{\mathrm{To}}^2 - \omega^2 - i\Gamma\omega}\right) \tag{2.71}$$

where ω_{TO} and ω_{LO}, represent the TO and LO phonon frequencies, while Γ defines the damping constant associated with optical phonon modes, respectively.

A plane wave incident on the surface of a polar material may stimulate an evanescent wave within the Reststrahlen band, provided methods for overcoming the momentum mismatch between the incident free-space light and the polaritonic mode are employed as described previously[3].

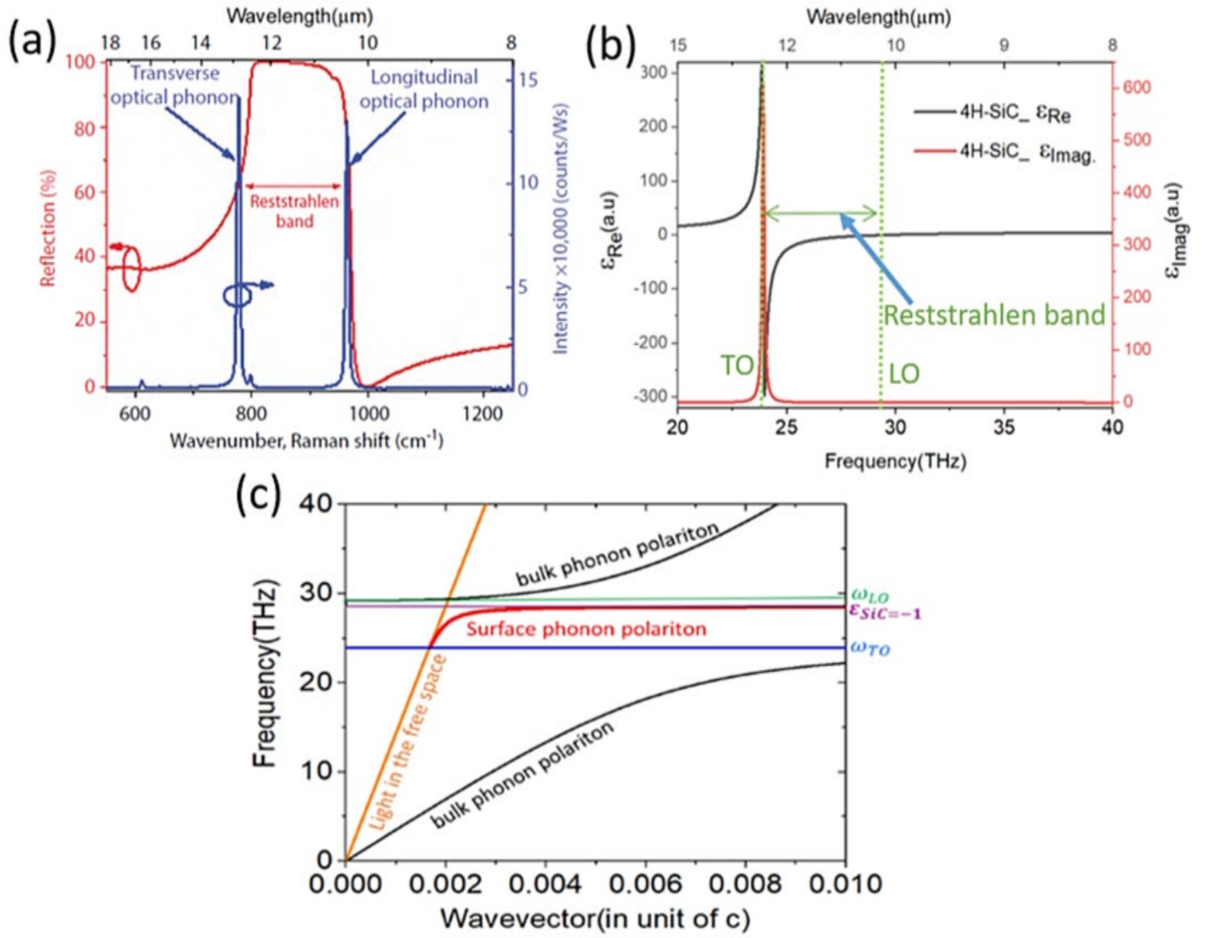

Figure 2.11. (a) Measured FT-IR spectra (red curve) of 4H-SiC indicates the high reflectivity nature of SiC within the Reststrahlen band, while the Raman spectra indicate the positions of optical phonon modes[4]. (b) The calculated dielectric function of 4H-SiC showing real and imaginary permittivity, the broken vertical black lines indicate the position of TO (left at 23.9 THz) and LO (right at 29.2THz) frequency, the two parallel vertical dashed lines (LO and TO) represent the Reststrahlen band, (c) Dispersion of surface phonon in 4H-SiC, and light is propagating in free space calculated using relation (2.40). We performed the calculations using 4H-SiC data for 4H-SiC $\omega_{TO} = 797$ cm^{-1} (23.9 THz), $\omega_{LO} = 973$ cm^{-1} (29.2THz), and $\Gamma = 4.7$ cm^{-1} (0.1 THz)[4].

2.9. Hybrid phonon-plasmon polaritons in graphene on polar materials

One of the essential aspects of graphene is that it can couple strongly to the various dielectric substrates for diverse applications[97]. However, one of the biggest challenges is to maintain its exotic properties while transferring it onto those substrates (most of the synthesis techniques are built on ex-situ growth where the transfer of graphene flakes is required for device fabrication and characterisation)[28]. For instance, suspended single-layer graphene can have carrier mobilities of about $200.000\ \mathrm{cm^2V^{-1}s^{-1}}$, but the mobility drops once graphene is placed on a dielectric or an insulating substrate such as SiO_2[98]. Surface optical phonons from the dielectric substrate induce increased scattering of the free carriers in graphene and serve as one of the predominant factors limiting the carrier mobility. This can be mitigated by placing graphene on an appropriate substrate, such as hBN[27, 99], where mobility can be much higher. Different ways to synthesise EG on silicon carbide on silicon have been developed[28, 35, 100]. The essential advantage of this growth technique is that the graphene layers are directly grown on the substrate. Thus, no transfer is required for optical/electrical characterisation and device fabrication, which prevents damage to the graphene layers, eliminates deleterious effects from residual polymers, and thus provides the most straightforward avenue towards maintaining the intrinsic properties of graphene.

This is a benefit for the development of EG-based photonic devices (e.g., photonic crystal cavities) on SiC on Si, thanks to the well-established silicon fabrication techniques and scalability[101, 102]. Moreover, one can optimise the geometry of this heteroepitaxial system containing graphene and SiC on Si to couple their SPP-SPhP modes. To understand this coupling within the EG/SiC system, in the following section, we analyse the dispersion relation for epitaxial graphene on SiC.

2.9.1. Dispersion of hybrid phonon-plasmon mode in epitaxial graphene on silicon carbide

Much of the physics of hybrid SPP-SPhP within the EG/SiC system can be extracted from the dispersion relation of this material system. However, it is worth looking back to the dispersion of each material involved in the coupling to analyse its effect. As discussed earlier, the dispersion of the large wavevectors of SPP modes in graphene at frequencies approaching the plasma frequency results in a large k-vector/momentum mismatch with free-space light. This results in extremely short polariton wavelengths and, thus, strong field confinement of SPPs in graphene. On the other hand, the dispersion curve of SPhPs in SiC coincides with the light line at the TO phonon and asymptotically approaches large momentum values near the LO phonon (Figure 2.12b). Hwang et al. realised that hybridisation between graphene and SiC polaritons modifies their dispersion curves[30], where two different energy regions arise (symbolised by $\omega_+$and ω_-) separated by a gap (forbidden zone) between surface optical phonon frequency (ω_{SO}) and ω_{TO} [30, 103]. ω_{SO} defines the asymptotic limit up to which the optical phonon mode can be stimulated on a planar surface, and it is related to ω_{TO} as $\omega_{SO} = \omega_{TO}\sqrt{\frac{\varepsilon_{st}+1}{\varepsilon_{\infty}+1}}$[30], where ε_{st} and ε_{∞} define the static and high-frequency dielectric constants of the material, respectively. One can notice from Figure 2.12c that for lower frequencies, the wavevector of the hybrid system drops towards zero ($k \rightarrow 0$), with the modes in the lower region (ω_-)

behaving more like SPP modes, while those in the upper region (ω_+) exhibiting characteristics more akin to the SPhPs and converge towards surface optical phonon frequency ($\omega_+ \rightarrow \omega_{SO}$). On the other hand, for higher wavevectors ($k \rightarrow \infty$) the mode in the lower region (ω_-) converges towards ω_{TO} and behaves more like SPhP mode (see Figure 2.12b for SPhP dispersion in 3C-SiC), while the modes in the upper ω_+ region exhibit SPP-like features (Figure 2.12a). These can be understood from the strong coupling between SPhPs supported in the substrate and the collective SPP mode and electronic degrees of freedom in graphene[6]. Note that the green lines for the dispersion curve of graphene/3C-SiC differ from the bulk phonon polariton observed in SiC, and this is because of the presence of graphene [30, 103].

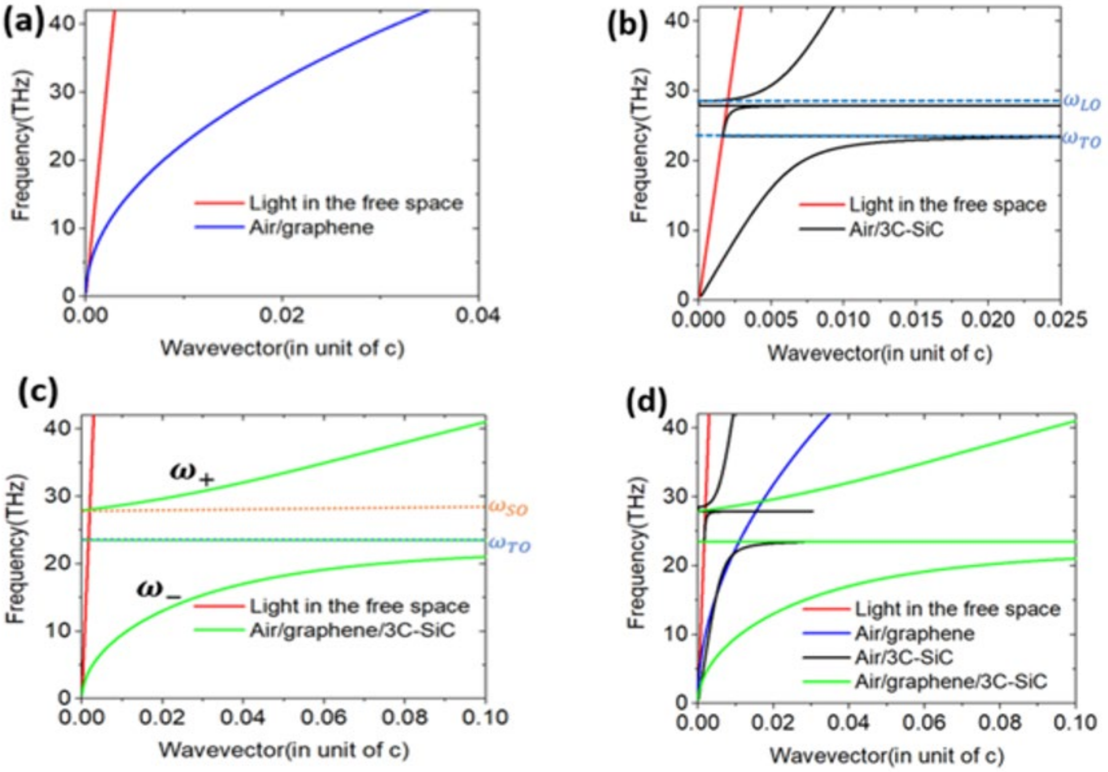

Figure 2.12. Dispersion relation of (a) SPP in the free-standing graphene (b) the dispersion of phonon polariton in a free-standing 3C-SiC. (c) The hybrid phonon-plasmon mode in air/graphene/3C-SiC material system (ω_+ and ω_- show the two regions resulting from the coupling between SPP mode in graphene and SPhP mode excited in 3C-SiC). (d) A comparison between the dispersion curve of free-standing graphene (blue), 3C-SiC (black curve), and air/graphene/3C-SiC (green curve) system. The wavevector is normalised to the speed of light in the free space "c". The calculation for the dispersion graphene on SiC was performed using equation (2.67) with Fermi energy $E_F = 1$ eV (245 THz) and dielectric properties data for 3C-SiC $\omega_{LO} = 118$ meV (28.5 THz), $\omega_{TO} = 97.3$ meV (23.5 THz), and $\Gamma = 0.6$ meV (0.1 THz)[4].

Furthermore, a comparison between individual dispersion curves (freestanding graphene and air/SiC) with the dispersion of hybrid SPhP-SPP in graphene/SiC shows a larger wavevector in hybrid graphene/SiC system (Figure 2.12d).This suggests that the resulting SPhP-SPP mode in EG/SiC exhibits strong confinement than the individual SPP and SPhP modes. The confinement and propagation length characteristics of polariton modes EG/SiC material are discussed in the next section.

2.9.2. Propagation and spatial confinement of hybrid SPP-SPhP mode in graphene on silicon carbide

As previously discussed in section 2.4, the propagation length and the degree of confinement of SPP/SPhP modes greatly influence their use in diverse photonics applications. However, it is not easy to find a plasmonic material with low propagation losses and strong confinement simultaneously. For example, the strong spatial confinement of graphene SPPs via the extremely short polariton wavelengths is understood to be limiting its propagation length to few tens of microns[104] and affects its use for some of the applications where long propagation lengths are required, such as in information processing and communications[105, 106]. As mentioned previously, the long lifetimes of SPhP modes do not necessarily result in commensurate increases in propagation lengths, with typical values reported falling in a range that is of an order comparable to that for SPPs[4, 107, 108].

To quantify the properties of the hybrid graphene/SiC material system, we used equations. (2.69) and (2.70), and calculated FOMs for graphene SPP and SiC SPhP modes and compared them with that of the hybrid SPP-SPhP mode (Figure 2.13). While SiC exhibits a slightly higher propagation FOM compared to graphene SPPs (Figure 2.13a), graphene outperforms SiC SPhPs in terms of spatial confinement (Figure 2.13b). One can notice that the hybrid graphene/SiC polaritons provide an improved FOM for spatial confinement compared to those of the individual materials (yellow and purple curves in Figure 2.13b). However, the propagation FOM for the SPP-SPhP mode in the hybrid graphene on the SiC system seems to be not as good as the FOMs of the individual SPP and SPhP modes in SiC and graphene (Figure 2.13a). As reported by Lu et al., FOMs for propagation and spatial confinement can be further improved by adjusting the chemical potential or carrier density in graphene [104]. For instance, by increasing the carrier density in graphene from $1 \times 10^{12}\ \mathrm{cm}^{-2}$ (used in the calculation for yellow curves in Figure 2.13) to $1 \times 10^{13}\ \mathrm{cm}^{-2}$ (and mobility of $\sim 100\ \frac{\mathrm{cm}^2}{\mathrm{Vs}}$ as reported in[109] for graphene/SiC system), we can improve the propagation at the expense of the confinement FOMs of hybrid SPP-SPhP mode in graphene on the SiC system (purple curves in Figure 2.13). Note that the improved FOM for propagating hybrid SPP-SPhP mode occurs near to ω_{TO} ($\sim$23.5 THz) and at the frequency ~28 THz (within the Reststrahlen band), the spectral position where SPhP mode in SiC can couple with graphene's SPP mode (see purple curve in Figure 2.13a).

Such improvements of SPP-SPhP modes was experimentally revealed for graphene coupled to hBN, which resulted in extended propagation lengths for the hybrid mode that were 1.5-2.0 times longer than the individual modes[27, 108]. Furthermore, this offers the opportunity to increase the propagation or lateral confinement depending on the desired applications.

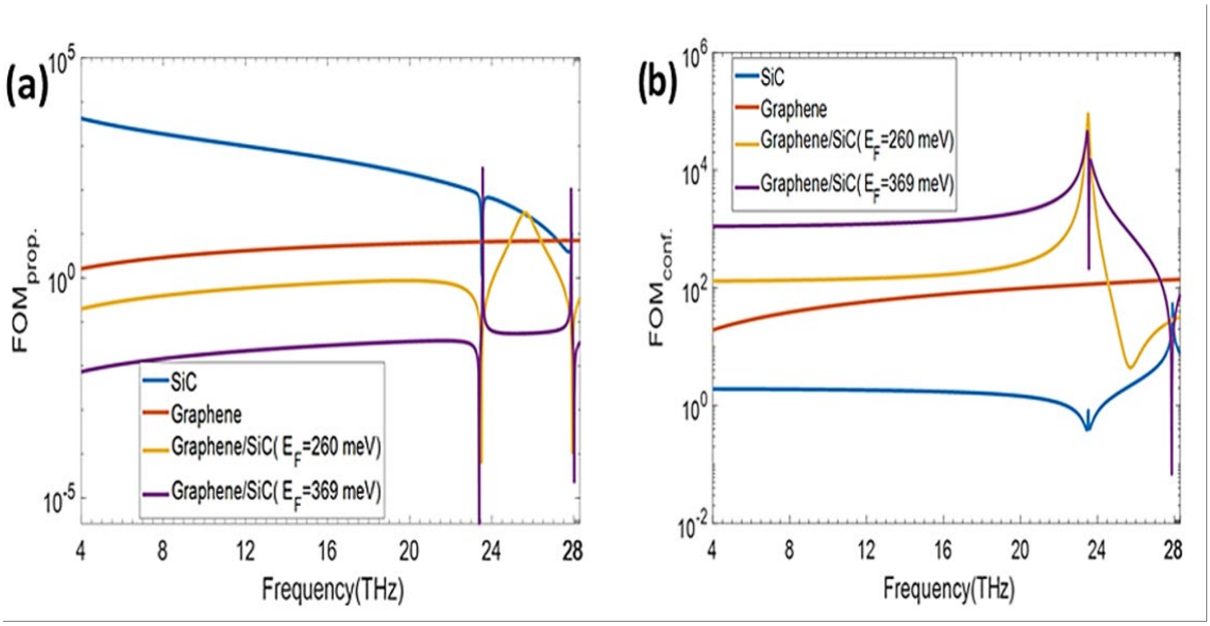

Figure 2.13. FOMs for graphene, SiC, and graphene on SiC. (a) FOM for the propagating mode (ratio of propagation length and wavelength of SPP or SPhP mode) (b) FOM for the lateral confinement of the modes (ratio of the free space wavelength and evanescent field decay in the air from air/plasmonic or phononic material interface). The yellow and purple curves show that the propagating and lateral confinement FOMs of the hybrid polariton modes in the graphene/SiC system can be improved by tuning the Fermi energy in graphene. The calculations were performed using $E_F = 260$ meV ($n \approx 1\times10^{12}$ cm^{-2}) with relaxation time $\tau = 261$ fs, and $E_F = 369$ meV ($n \approx 1\times10^{13}$ cm^{-2}) with $\tau = 4$ fs. The dielectric properties data for 3C-SiC used here are $\omega_{LO} = 118$ meV (28.5 THz), $\omega_{TO} = 97.3$ meV (23.5 THz), and $\Gamma = 0.6$ meV[4].

2.10. Summary

In this chapter, the theoretical background for excitation surface polaritons modes was discussed. First, the dispersion relation of SPP modes in a conductor and a dielectric medium were discussed. Secondly, we used the dispersion relation of air and silver planar interface to discuss the mechanism and conditions leading to the excitation of SPP modes and discussed the three-length scales of SPP modes, namely: polariton wavelength, propagation length and penetration depth. Subsequently, we extended the theory to the dispersion relation of SPP and SPhP in graphene and silicon carbide, respectively. Our calculation revealed significant modification of the individual SPP and SPhP modes' dispersions which result from the hybridisation of SPhP-SPP modes in the EG/SiC system. Furthermore, the calculations revealed this hybridisation to improve the propagation and confinement figures of merit of this system's resultant hybrid SPhP-SPP modes.

Chapter 3. Literature review

3.1. Graphene growth techniques

H.P.Boehm et al. reported producing a monolayer graphite sheet in 1962[110]. Twenty-four years later, they gave the name graphene to their monolayer graphite[111]. Since the discovery of graphene, several graphene production techniques were reported, such as micromechanical exfoliation of small mesas of highly oriented pyrolytic graphite[64], chemical vapour decomposition(CVD) on metals and insulators[112-114], unzipping of carbon nanotubes[115], chemical reduction of graphene oxide[116], and thermal decomposition of a bulk SiC substrate[29, 117, 118]. Herein, the most popular graphene growth techniques, such as mechanical exfoliation, CVD, and thermal decomposition of SiC, are discussed.

3.1.1. Micromechanical exfoliation of single-crystal graphite

Micromechanical exfoliation of monolayer graphene from highly ordered pyrolytic graphite(HOPG) was first realised by Andrei Geim and Kostya Novoselov in 2004[64]. In this technique, they used an adhesive tape on the surface of HOPG, and by exerting normal force on the HOPG surface, they obtained monolayer graphene, which was transferred to the substrate to reveal for the first time the electronic properties of graphene. This work won Geim and Novoselov a Nobel Prize in physics in 2010. The graphene produced through this technique revealed the best quality and large area flake. To date, outstanding graphene properties had been discovered with graphene produced by the mechanical exfoliation technique. However, the challenges with mechanical exfoliation are that it is a labour-intensive and time-consuming method that makes it impracticable to scale it up for industrial mass production.

Moreover, this technique requires that the produced graphene be transferred to the substrate, such as silicon and silicon oxide, for further processing and device fabrication. However, such a process degrades graphene's electrical and optical properties due to the substrate's scattering effect[119, 120]. Also, the transfer of graphene flake on the substrates can cause graphene defects, affecting graphene-based devices' quality[120]. Therefore, a more suitable method to overcome the above issues is required.

3.1.2. Chemical vapour decomposition on metals and insulators

The chemical vapour decomposition (CVD) process uses hydrocarbon gases such as methane and ethane, which are annealed at high temperature and decompose into carbon radicals on the surface of metals such as Ni, Cu, Ir, and Co, which rearrange to form a single layer or a few layers graphene[121-125]. Metals play two fundamental roles in the CVD method: first, they act as catalysts to lower the energy barrier of the reaction; second, they define the graphene deposition mechanism, which is vital for the quality of graphene produced via the CVD growth method[121].

The CVD method produces high-quality graphene over large areas. For example, in 2011, Bae et al. used a roll to roll CVD to grow large-area graphene on 30 inches wafer for transparent electrode applications, where their graphene displayed optical transparency of 97.4% and sheet resistance of 125 Ω/sq[28, 112]. When they stack together four layers of their doped graphene, they recorded sheet resistance of 30 Ω/sq and optical transmittance of 90%, higher than the commonly used indium tin oxide transparent electrodes[28, 112].

Despite the mentioned advantage of CVD graphene, however, the graphene produced in this process needs to be transferred onto the appropriate substrate for further characterisation. The main scattering mechanisms linked to the graphene produced via CVD are dislocations, lattice defects, grain boundaries, and other substrate-related disorders[28, 126]. The metals can also contaminate the quality of graphene produced, affecting graphene-based devices' performance. Therefore, to overcome these challenges, a transfer-free technique for large-area graphene production is required.

An effort to improve the CVD graphene growth method was made by growing graphene on the dielectric substrates such as SiO_2, h-BN, Al_2O_3[127-129]. For instance, the grain boundaries scattering and transfer-related contaminations are minimised with increased carrier mobility of up to 30 000 cm^2/Vs for CVD graphene grown on h-BN substrates[126]. However, the CVD growth of graphene on the dielectrics is generally difficult due to the low surface energy of the dielectrics[130], where a plasma-enhanced CVD at low temperature is required to overcome this.

Consequently, direct growth of graphene on SiC was invented as an alternative method to overcome the challenges associated with mechanical exfoliation and CVD growth techniques. Contemporary, diverse graphene growth techniques through SiC substrate were developed, and we discuss some of them in the following section.

3.1.3. Thermal decomposition of silicon carbide

Thermal decomposition of a bulk SiC substrate was introduced as a suitable alternative path to obtain a transfer-free, homogeneous, and large-area graphene for electronic and photonic application[117, 118, 131, 132]. This technique consists of sublimation of Si from the SiC sample at a high temperature ~1400°C under the vacuum/controlled atmospheric pressure conditions, as the vapour pressure of carbon is higher than silicon's, at such temperatures, the surface carbon atoms reconstruct to form graphitic layers [28, 117]. D.V.Badami reported the first thermal decomposition of bulk hexagonal SiC in 1965[133]. He annealed the SiC crystals to an extremely high temperature of ~ 2180 ºC for one hour under vacuum to realise a graphite layer on top of SiC. Ten years later, Bammel et al. reported monolayer graphite on the C face and Si face of hexagonal SiC, grown at the low temperature (~800 ºC), and ultra-high vacuum(UHV)[134]. In these early reports, graphene was identified as monolayer graphite. In 2004, the De Heer research group at the Georgia Institute of Technology, USA, reported the first transport measurements on three graphene sheets grown via thermal decomposition of 6H-SiC[29]. Their reported graphene exhibited the Dirac nature of the charge carriers with mobility over 1100 cm^2/V s, which was increased later on by improving their graphene's quality on SiC[117, 135].

Although the thermal decomposition of SiC in a high or ultra-high vacuum seems to be a promising route towards large-area production of graphene-based electronic and optoelectronic devices, the challenge is that the graphene produced through this process contains small grains of 30-200 nm with varying thickness[28, 136, 137]. These results from the morphological transformation of the SiC surface when annealed at a high temperature. Additionally, graphene produced via thermal decomposition of SiC with high/ultra-high vacuum shows poor quality due to the significant sublimation rates at low temperatures.

Emtsev et al. reported a method to improve graphene layers' morphology on the SiC surface[118]. Their method consists of annealing the SiC samples at 1650 ºC in an argon environment. Here argon environment enables the reduction of the evaporation rate of Si atoms[138]. The released silicon atoms from the surface can be reflected back to the surface by colliding with argon atoms. The high temperatures used in this experiment improved surface diffusion such that surface rearrangement occurs before graphene formation. Further improvements of graphene produced via thermal decomposition of bulk SiC were reported in the following references[117, 139, 140].

3.1.4. Direct growth of graphene on silicon substrates

Even though good quality graphene can be realised on bulk SiC via the thermal decomposition method, the challenges with this technique are the limited size of SiC wafers, their high cost, and the limitation of available micro-nano machining processing tools for bulk SiC wafers. Ideally, one would benefit from having graphene directly on a silicon substrate for diverse technological applications using conventional, complementary metal-oxide-semiconductor (CMOS) processes. Large area graphene growth on Si substrates offers the opportunity to explore the potential properties of graphene using Si technologies and enable the development of graphene-based micro- nanophotonic devices. Graphene on cubic silicon carbide (3C-SiC) emerged as an appealing route for graphene directly grown on Si substrates. The following section discusses the advancement of graphene on 3C-SiC/Si, associated challenges and opportunities.

3.1.5. Graphene on silicon through heteroepitaxial cubic silicon carbide

Although various techniques to grow graphene on 3C-SiC on Si had been proposed, here we only focus on the two most promising techniques: thermal decomposition of 3C-SiC on Si and metal-mediated graphene growth on 3C-SiC on Si.

3.1.5.1. Graphene growth through thermal decomposition of cubic silicon carbide on silicon

Thermal decomposition of 3C-SiC on Si is the most investigated technique to produce epitaxial graphene on Si substrates, and many researchers have been reporting graphene grown via this technique with a slight modification from one’s growth process conditions to the others [100, 131, 141-145].

In 2009 Suemitsu et al. successfully reported the first epitaxial graphene (EG) on Si via the thermal decomposition of 3C-SiC(111) on Si(110)[146]. Two steps were involved in their graphene growth: - the growth of 3C-SiC(111) on Si(110) substrate through gas source molecular beam epitaxy (GSMBE) with monomethyl silane (MMS) used as a single source gas, followed by– annealing the samples at high temperature ~1300 ºC for 30 minutes under ultrahigh vacuum to realise a single and two-layer graphene on 3C-SiC(111) on Si(110). Their graphene on silicon unlocked the doors toward graphene-based devices on the silicon substrate, and thus they called their technique graphene on silicon (GOS) technology. Even though they believed that graphene was grown on 3C-SiC(111)/Si(110), their later studies revealed that graphene was grown on 3C-SiC(110)/Si(110)[147]. Subsequently, in 2010 Suemits, and Fukidome successfully grew graphene on 3C-SiC(111)/Si(111) and 3C-SiC(100)/Si(100)[142], respectively. Other research groups also developed a method to grow graphene on a silicon substrate, like Ouerghi's team from CNRS in France, which used the high vacuum sublimation process at high temperature 1300 ºC to produce GOS[100, 143, 148]. Their approach consists of the degassing of SiC on Si samples at 600 ºC under ultra-high vacuum conditions followed by the removal of native oxide by annealing the samples under a low(0.1 mm per minute) Si flux at 900 ºC, followed by annealing the sample at high-temperature of 900 to 1300 ºC to obtain EG/SiC.

The quality of graphene produced through thermal decomposition of 3C-SiC on Si substrates can be affected significantly by the defects like surface roughness, crystallographic defects, and orientation of the SiC films[147, 149, 150]. For example, a significant amount of antiphase boundaries(defects) were reported for 3C-SiC heteroepitaxial films on Si(100) substrate[151]. Therefore, these antiphase boundaries can be transferred to the graphene layers on 3C-SiC on Si(100) and degrade the graphene's intrinsic properties[28]. An effort was performed by growing 3C-SiC films on off-axis(100) silicon substrates to remove these antiphase boundaries, where single domain epitaxial graphene layers were realised on the surface[144]. Alternatively, the 3C-SiC films grown on Si(111) substrates are believed to be less affected by the antiphase boundaries and thus the most preferred surface for epitaxial graphene growth[144, 145]. The surface roughness of 3C-SiC films is also a vital parameter that affects the quality of epitaxial graphene. One of the properties of epitaxial graphene strongly affected by the surface roughness is the electron mobility and misorientation of the graphene layer[147, 150]. The high-quality epitaxial graphene layer requires a surface roughness of less than 1 nm[28]. Numerous techniques were proposed to improve the 3C-SiC surface's smoothness, such as plasma-assisted polishing and chemical mechanical polishing[152-154].

There are two significant limitations with graphene grown via the thermal decomposition of SiC: the limited quality of the graphene layer produced via ultrahigh vacuum, resulting from the difficulty of controlling sublimation rates[131, 149] and the relatively higher Raman intensity ratio for D and G band $\left(\frac{I_D}{I_G} \approx 1\right)$ than the exfoliated graphene[131, 146]. Moreover, graphene growth via thermal decomposition of SiC on Si is limited to the use of 3C-SiC(111)/Si(111)[100, 147].

Consequently, a metal-mediated graphene growth on cubic silicon carbide on silicon was invented as an alternative to the thermal decomposition approach.

3.1.5.2. Metal mediated growth on cubic silicon carbide on silicon

A catalyst–based method for realising epitaxial graphene on 3C-SiC on Si substrate was introduced to overcome the limitations encountered in the thermal decomposition of 3C-SiC on Si. This method consists of deposition of a metal layer such as cobalt or nickel on the surface of 3C-SiC on Si sample followed by annealing at 750 to 1200 ºC, relatively lower than the temperature used in the thermal decomposition approaches. The metal reacts with SiC atoms during the annealing phase to form metal silicides and release carbon atoms into the system[155]. During the cooling phase, carbon atoms released during the annealing stage rearrange to form graphene. However, on most occasions, the graphene is formed on the metal surface, which still requires the transfer onto the appropriate substrates for further processing and limits its usage to small-scale device fabrication. Even though the nickel-mediated approach for amorphous and crystalline SiC on silicon appeared promising, uniformity of the graphene layer and density of the defects remained the critical challenges.

To overcome these limitations, our research group led by Professor Francesca Iacopi successfully invented an alloy-mediated catalytic approach to grow high quality and highly uniform graphene on 3C-SiC/Si (100) and 3C-SiC/Si(111) substrates using nickel and copper as the catalysts[33, 34, 37]. This method consists of depositing a double layer of nickel and copper on 3C-SiC on Si substrate, followed by heating the sample at 1100 ºC for 1 hour. After graphitisation, excess carbons and metal silicides on the sample's surface get removed through subsequent wet chemical etching. This results in high quality and uniformly distributed graphene on 2 inches Si wafer with a Raman intensity ratio for D and G band ranging between 0.2 and 0.3, revealing fewer defects for graphene grown through this approach[33, 34]. It is worth noting that the Raman intensity ratio for D and G band in this process is consistent over large areas and relatively small compared to those reported on epitaxial graphene on 3C-SiC on Si using other growth techniques[131, 147, 148]. The advantage of this synthesis process is that it offers a straightforward, site-selective and CMOS compatible platform for fabricating micro and nanostructure of any complex EG/SiC shape at a large wafer scale.

Details on an alloy-mediated catalytic approach are discussed in the methodology chapter 4.

3.2. A review on the surface polariton modes in graphene and silicon carbide

3.2.1. Overview of graphene plasmonics

As discussed specifically for graphene in a number of reviews over the past few years[6, 9, 72, 156], graphene has the major advantage of broad tunability, enabling spectral tuning over much of the MIR to FIR spectral range. While in this chapter we limit our discussion on the tunability of SPP modes in graphene, it is worth highlighting that recent work has also been able to show exotic physics, such as photodetection[157] and emission[158, 159], as well as nonlocality[160-163], and polariton properties controlled by moire lattice formation[164] in stacked layers. This highlights that while graphene plasmonics research has spanned the past decade, new phenomena are identified regularly within this material. In particular, it is worth highlighting that bilayer graphene may also hold many benefits in terms of infrared optoelectronics[156, 165, 166]. However, for this thesis, we focus the discussion on the tunable properties of graphene plasmons as it pertains to their interactions with silicon carbide.

3.2.1.1. Tunability of surface plasmon polariton in graphene

The linear dispersion of the Dirac fermions in graphene is the basis of its broadband tunability, which makes it superior to other plasmonic materials[6]. Typically, the charge carriers induced in graphene through doping can be increased from on the order of $10^{11}\ \mathrm{cm}^{-2}$ to $10^{13}\ \mathrm{cm}^{-2}$[167]. Pradeep et al. used Hall effect measurements and have recently reported carrier concentrations exceeding such values, reporting $3 \times 10^{13}\ \mathrm{cm}^{-2}$ and $7 \times 10^{13}\ \mathrm{cm}^{-2}$ for EG on SiC/Si(100) and EG on SiC/Si(111), respectively[109]. Additionally, the carrier concentration in graphene can be increased up to $10^{14}\ \mathrm{cm}^{-2}$ through electrostatic gating[168]. Such broad tunability has enabled the realisation of numerous novel photonic devices and applications, such as tunable signal modulators[97, 169-173], optical detectors[14, 79, 174, 175], and filters[176, 177], along with many others. As previously shown in equations. (2.64 and 2.67), both the conductivity and SPP dispersion of graphene depends directly upon the Fermi energy and are also strongly sensitive to the nature of the surrounding dielectric environment, frequency, electronic band structure, and densities states of the carriers[72]. For monolayer graphene, the Fermi energy can be calculated as: $\mathrm{E_F} = \sqrt{\pi \hbar^2 \mathrm{v_F^2}\ \mathrm{n}}$, where $\hbar$ represents the reduced Planck constant, while $\mathrm{v_F}$ and n represents the graphene Fermi velocity ($\approx 10^6 \frac{\mathrm{m}}{\mathrm{s}}$) and carrier concentration, respectively. Thus, the carrier density control can be simply represented via the Fermi energy in EG[178, 179] and free-standing graphene[180-182]. The roughness of the SiC film on which EG is formed can affect carrier mobility, with a roughness of about 1 nm RMS required for good-quality EG[28, 183]. Other factors that impact the intrinsic properties of EG are crystallographic defects, such as anti-phase boundaries[151], which are more prevalent in thinner films[184, 185].

Due to the strong sensitivity to local materials and interfaces in the proximity of graphene, these changes in the environment can induce doping in graphene through charge transfer processes, where p-doping can result from polymers with nitrogen, fluorine, and oxygen constituents, while n-doping can be induced in graphene on metallic samples[72]. Thus, careful materials selection is needed to control the carrier density and doping, and it has become one of the most common practices in controlling its electronic properties. For example, Hu et al. demonstrated the use of an ion-gel to induce a broadly tunable SPP mode at a fixed frequency of 1270 cm^{-1} using low voltage modulation of about 4V tuned from the Dirac point [186](see

Figure 3.1). Furthermore, by encapsulating graphene between hexagonal boron nitride layers, it is possible to maximise the propagation length[99].

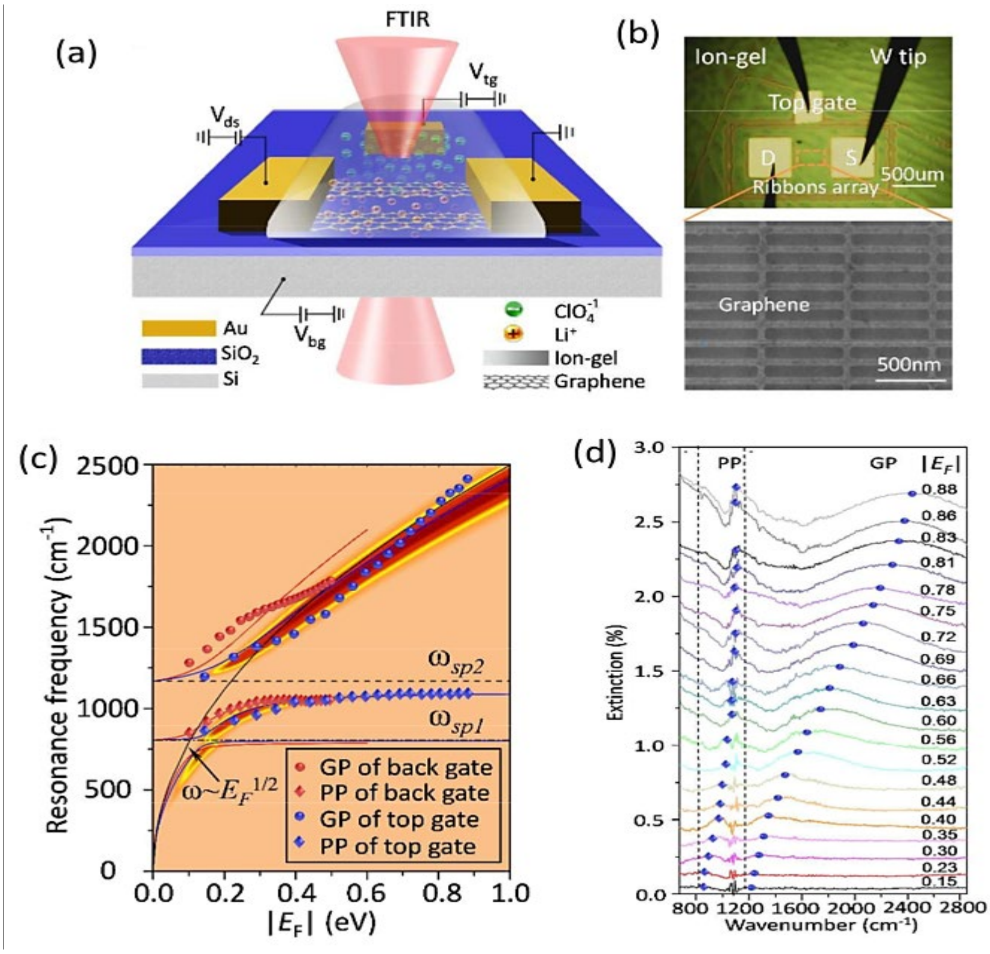

Figure 3.1. Hu et al. work on graphene tunable plasmons[186]. (a)The experiment diagram set up for graphene plasmon tunable device, (b) top image shows an optical micrograph of the fabricated graphene nanoribbon device covered with ion gel (green), and the bottom is an SEM image of graphene nanoribbon array. (c)The calculated resonance frequencies of phonon like polariton (PP) and graphene' plasmon (GP) peaks as a function of Fermi energy controlled through the top gate (blue curves) and through the back (red curves), diamond and spheres curves denote experimental results. (d) Extinction spectra of the graphene nanoribbon array at different values of Fermi energy tuned through the top ion gel. The Figures were adapted with permission from[186] Copyright © Royal Society of Chemistry 2015.

Tunable SPP modes can also be realised when coupling graphene modes with the localised SPP mode of a metal. Generally, metals exhibit lower optical losses than graphene in the visible and NIR spectrum (optical loss in graphene in the visible range is due to the interband transitions of charge carriers). A tunable SPP mode can be realised with a metal nanostructure coated with graphene with effective EM energy coupling at these frequencies. For instance, tunable and robust graphene/metal plasmon can be realised from the devices designed from graphene and metal nanoparticles, where the localised SPP resonance in the metal can be controlled by graphene. Niu et al. demonstrated this with graphene and metal nanoparticle structures which exhibit tunable SPP resonances[187]. In Figures 3.2a and 3.2b, their graphene-gold hybrid nanostructure is shown. The tunability was controlled by changing the thickness of the dielectric (Al_2O_3) spacer implanted between graphene and the metal nanoparticles. When they varied the spacer thickness from 0.3 nm to 1.8 nm, the wavelength of the surface plasmons resonance peak blue-shifted from 583 nm to 566 nm. This change in resonant frequency results from the electromagnetic field coupling strength variation between the localised SPP mode induced by metal nanoparticles and graphene film. For graphene coupled on a gold nanorod such as in[188], the resonance frequencies of localised SPP can be controlled by modifying interband transitions in graphene through electrostatic gating, and the frequency shifts are controlled by the polarity of the applied gate voltage (see Figure 3.2c and 3.2d).

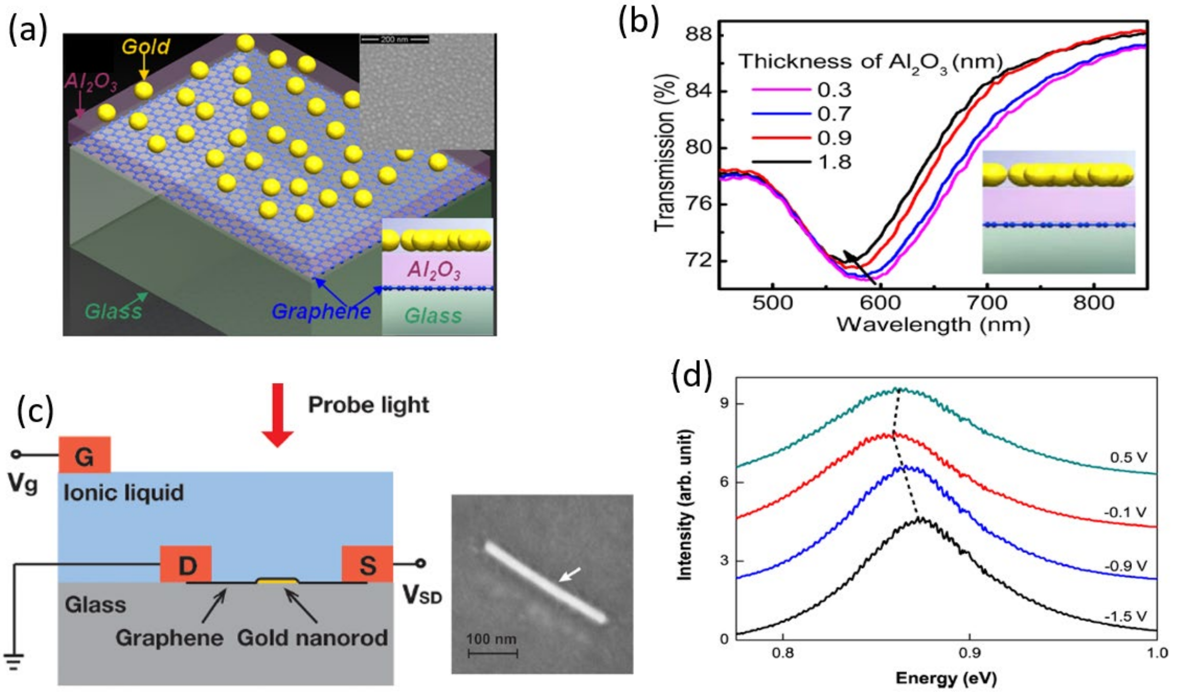

Figure 3.2. (a) A schematic of the structure with graphene embedded between the dielectric medium to induce tunability of gold nanoparticles formed on the top of dielectric (inset show SEM and the cross-sectional view of the device), (b) tunability of resonance wavelength. (c) Schematic of the device with graphene on the top of gold nanorods to show how electrolyte gate with the ionic liquid is used to tune the plasmon resonance through graphene. The inset shows an SEM image (100 nm resolution) of gold nanoribbon coated by graphene. (d) Rayleigh scattering spectra of the graphene-based device at four different gate voltages to confirm its ability to excite tunable plasmon. (a &b) adapted with permission from [187], © 2012 American Institute of Physics, and (c &d) adapted with permission from [188] Copyright © 2012 American Chemical Society.

Liu et al. proposed a highly tunable hybrid metamaterial as a high-speed THz modulator using graphene resonators as a source of SPP coupled to metal-based ring resonators. Their device can potentially be applied in sensing, nonlinear frequency generation, and photo-detector[189]. In their study, monolayer graphene sheets were grown through CVD and transferred on SiO_2/Si substrate, which was also employed as a back gate for electrostatic control of the carrier density in graphene[189]. Furthermore, graphene induced tunability through electrical doping of the graphene layer and coupling on the dielectric substrates for diverse applications were studied in [190-200]. Thanks to its lower loss nature at the THz and MIR frequencies, depending on the intended applications, effective doping of graphene can be used as a channel to tune the surface plasmon mode. For higher frequencies such as in the visible spectrum, graphene can be coupled with noble metals to tune their low loss localised surface plasmon resonance.

The following sections discuss graphene-induced tunability of hybrid SPhP-SPP modes in epitaxial graphene on silicon carbide at the MIR regions. However, before we review the works about hybridisation between SPhP-SPP in EG/SiC, let us start by reviewing the recent progress on SiC‘s based nanophotonics.

3.2.2. Silicon carbide nanophotonics

Analogous to plasmonic materials, the surface of SiC can be carefully tailored, and nanostructure patterns fabricated into it that can support long-lived localised SPhP modes[201-206]. These SPhPs modes are known to be tightly confined at subwavelength scales and exhibit high-quality factors with expected Purcell enhancements on the order of about three order magnitudes higher than what is attainable with noble-metal and doped semiconductor plasmonic structures[84, 207]. Furthermore, akin to plasmonics, nanoscale patterning of SiC can also create gratings and enable phase matching for the excitation of propagating modes[202]. The ability to couple localised resonances with propagating modes in SiC has been proposed as a means to realise photonic integrated systems similar to those with SPP modes[208]. One such hybrid localised/propagating SPhP mode is the so-called monopole resonance that results from a coupling between a propagating SPhP and a modified longitudinal dipole when nanostructures are fabricated into the same polaritonic material[95, 209-213]

Feldman[214, 215] was the pioneer in developing our understanding of optical phonons within SiC, with Nienhaus[88] and Nakashima and Harima[216] extending our understanding substantially when they revealed excitation of surface phonons in 3C, 4H, and 6H-SiC using Auger electron spectroscopy, high-resolution electron energy loss spectroscopy and with Raman scattering techniques. Tiwald et al.[217] reported a widely employed dielectric function model for SiC that subsequently enabled the seminal works of Hillenbrand et al.[218] and Greffet et al.[219], which revealed the first experimental studies of SPhPs in this material. Hillenbrand et al.[218] used scanning near field optical microscopy (SNOM) to investigate propagating SPhPs on 4H-SiC surfaces.

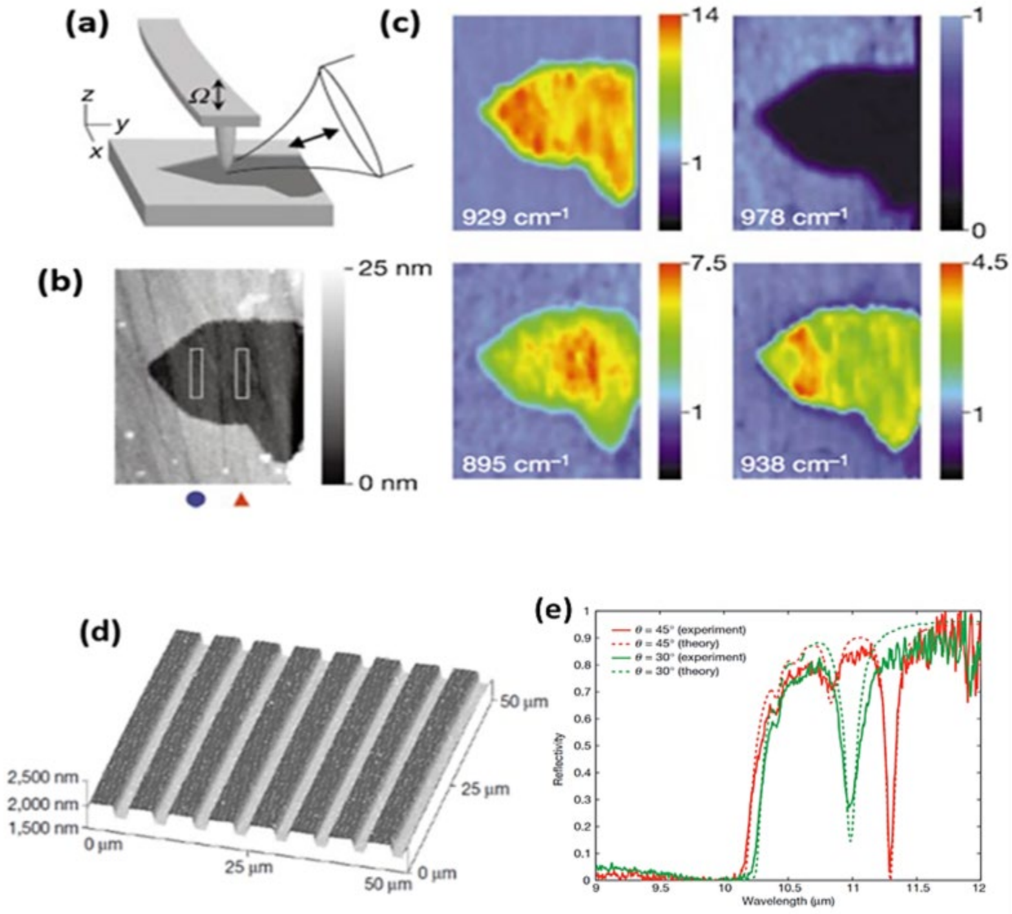

Figure 3.3. Experimental works on the propagating SPhP mode in SiC. (a) Probing of phonon in SiC using scattering-type MIR scanning near field microscopy (s-SNOM). (b) Image of Au covering SiC sample (2 rectangles shows the area used to extract the data. (c) The infrared near field images showing the scattering field amplitude taken at different illumination frequencies (the blue colour shows Au). SiC surface looks much brighter than other areas covered by Au at the phonon resonance frequency (929 cm^{-1}). The contrast reverses at 938 cm^{-1}. IR images taken from either side of the phonon resonance show a systematic local variation at 895 cm^{-1} and 938 cm^{-1}. (d) Atomic force microscopy image of SiC-based grating to support SPhP. The period of grating d=0.55λ (λ=11.46 μm) was taken so that the propagating surface wave could couple with the propagating wave at the studied frequencies. (e) Measured and calculated reflectance of SiC grating at the MIR, Showing the dependence of SPhP response on the incident angle. (a-c) adapted with permission from[218] Copyright © 2002, Springer, and (d & e) adapted with permission from[219] Copyright © 2002, Springer.

By mapping the spatial amplitude (proportional to reflection) and phase (absorption) of the infrared optical response of the material resulting from the scattering of incident infrared laser light off of a metalised atomic force microscope tip near the SiC surface, they revealed a contrast in the near field amplitude of the sample at frequencies within the Reststrahlen band. This is shown in Figure 3.3a-c, where the brightness of the SNOM image displays enhancement in the scattering amplitude of incident optical fields on the surface of 4H-SiC in comparison to the surrounding Au. At the same time, Greffet et al.[219], used SiC-based gratings to induce spatially coherent thermal emission (Figure 3.3d-e). This was followed by Taubner et al. exploring superlenses in the near field[205] and additional work from the Shvets group, which demonstrated prism coupling for chemical sensing platforms[220, 221].

Subsequently, Schuller et al. demonstrated the far-field measurements of the resonant localised modes[206] and that they could serve as the basis for a polarised narrowband IR thermal source[222]. Caldwell et al. demonstrated silicon carbide-based nano-antennas wide flexibility and tunability, where they explored sub-diffractional, localised SPhPs in nanopillar arrays fabricated in 6H-SiC[84]. Extraordinarily narrow resonance linewidths (ranging from 4 to $24\ \mathrm{cm}^{-1}$), were reported, with corresponding quality factors of about 40 to 135, which exceeded typical values in pure plasmonic resonators by about an order of magnitude (Figure 3.4a-c). Similarly, Wang et al. demonstrated the ability to realised resonant SPhP modes through creating metal apertures on the surface of SiC, which offered quality factors as high as 60[223]. More recently, a few hundred quality factors have been reported in this material system[224, 225]. The model reported by Caldwell et al.[84] revealed coupling of the localised SPhP modes to extremely small modal volumes ~ $\left(\frac{\lambda_{\mathrm{reso}}^3}{\mathrm{V}_{\mathrm{effect}}}\right)^{\frac{1}{3}}$, which yielded potential Purcell enhancements of 1.9×10^6 to 6.4×10^7, far larger than what can be theoretically realised with SPPs. Furthermore, Chen et al.[202] reported that the resonance intensities remain almost unaffected irrespective of variation in the filling fraction of the nanopillars, resulting from the strong coupling between the localised and propagating SPhPs supported in this system. Gubbin et al. (2016), built on this work, investigating the strong coupling, localisation, and propagation of SPhP modes in SiC-based resonators (cylinders of micron size)[202]. In their study, the nanoresonators were fabricated into SiC wafers to induce the localised SPhP modes and act as grating coupler for excitation of propagating SPhPs (Figure 3.4d-f). From the tunability of the SPhP dispersion, they found a spectral anti-crossing occurred between localised and propagating modes, which confirmed strong coupling between them. It is worth noting that such an anti-crossing is only achievable if the Rabi frequency (oscillation frequency of a Rabi cycle undertaken for a given atomic transition in a given EM field) exceeds the losses of the combined modes[226].

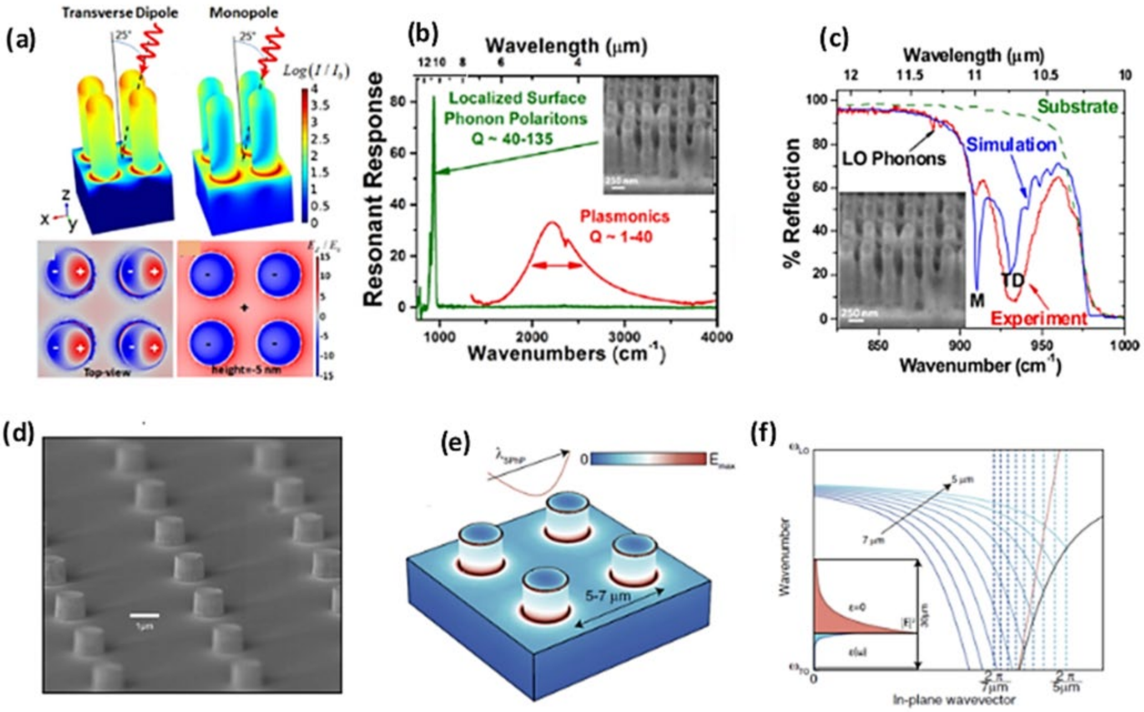

Figure 3.4. Excitation of localised SPhP in SiC. (a) The profiles of the field distributions in SiC-based nanopillars with contributions due to the transverse dipole and monopole modes. (b) depicts the spectral resonant responses of 6H- SiC-based nanopillars with a comparison between the Q factor of plasmonics mode (in plasmonic materials) and localised SPhP modes (in polar dielectric materials) for 6H-SiC, Inset shows arrays of 6H- SiC-based nanopillars. (c) FTIR reflectance spectra of the periodic array on 6H-SiC with the simulation results of the nanopillars showing the monopole (M) and transverse dipole (TD) resonances of the SiC-based device. (d)SEM image of a SiC device fabricated to excite localised SPhPs modes. (e) Electric field norm for the modes of the coupled array with the sinusoid curve to show the SPhP mode wavelength. (f) Dispersion of the SPhP mode (black curve), the solid blue line show SPhP mode folding from the edge of the first Brillouin zone for different periodicities varying from 5-7 μm, while the inset shows the norm of the electric field of the SPhP mode at air/SiC interface. (a-c)adapted with permission from[84], Copyright © 2013 American Chemical Society. (d-f) Adapted with permission from[202], © 2016 American Physical Society.

Recently, Gubbin et al. used 4H-SiC nanopillars to demonstrate strong coupling between transverse and longitudinal SPhPs and theoretically modelled this behaviour through the realisation of hybrid excitations referred to as longitudinal-transverse-phonon-polaritons (LTPP). These strongly coupled modes were observed experimentally by tuning localised SPhP monopolar resonance into the spectral proximity of a zone-folded LO phonon intrinsic in SiC polytypes with higher degrees of hexagonality[227]. Such coupling between longitudinal and transverse fields offers the potential opportunity to electrically stimulate optically active modes, with their work paving the way towards the development of novel MIR emitters. Similarly, Folland et al. recently demonstrated that SPhPs in SiC could couple to molecular vibrational transitions in a liquid, paving the way for a new methodology for creating vibrational polaritons and strong coupling in liquids[228]. Further opportunities for ultrafast modulation of SPhPs were demonstrated by Dunkelberger et al. through the injection of free carriers into localised SPhP resonators[229].

Nevertheless, the challenges associated with excitation of the SPhP modes in polar materials are that their responses are limited to the narrow, material-specific Reststrahlen bands, hindering the exploitation of these modes over broad frequency ranges[96, 108]. Further, the fast spectral dispersion in the dielectric function within this band also infers that the SPhPs will result in modes with exceptionally slow group velocities, thereby limiting propagation lengths despite the long polariton lifetimes[4]. While efforts to overcome such limitations are underway via the crystalline hybrid concept[230], these challenges remain a significant roadblock. On the other hand, the experiment conducted by combining polar materials with graphene has revealed an ability to overcome the restrictions of SPPs and SPhPs through the electromagnetic hybrid concept[230], which relies on the formation of phonon-plasmon hybrid modes[26, 30, 103, 231-233]. These experiments demonstrate the possibility of developing devices with low losses due to the long lifetimes of SPhPs and the broad spectral tunability of graphene SPPs. For instance, hybrid SPP-SPhP modes in graphene and hBN were demonstrated to propagate longer than the pure polaritons in either material[27]. Moreover, the coupling of graphene SPPs with SPhPs in polar materials is supported by recent advancements in synthesis techniques, enabling graphene to be grown directly on a given substrate, perhaps most notably on silicon [33, 35, 131]. The following section will review the current literature about hybrid SPP-SPhP modes within graphene on silicon carbide heterojunctions.

3.2.2.1. Graphene on silicon carbide photonics

The successful synthesis of EG on 3C-SiC/Si wafers was a substantial leap forward as such a system enabled large area and uniform growth of graphene on a desirable substrate, which benefits the advancement of photonic and electronic research fields[29, 234]. SiC has been used in micro/nano-electronics for many years, and studies on growing pristine graphene on different polytypes of SiC have been conducted for more than a decade[28, 29]. However, there is still a need to get further insights into the interactions between graphene and SiC, such as carrier dynamics that can be affected by the range of coupling and interference effects that result from optic-phonon/free-carrier interactions. Recent progress in obtaining graphene from hetero-epitaxial 3C-SiC on silicon[35, 37, 131] holds promise for potentially adopting and translating this powerful approach to create a platform for nanophotonics in a silicon-compatible material system.

A study investigating the coupling of SPP and SPhP modes in epitaxial graphene on SiC was conducted using dispersion measurements via angle-resolved electron energy loss spectroscopy (AREELS)[26]. In their work, graphene was epitaxially synthesised on a 6H-SiC (0001) substrate. AREELS measurements were performed on epitaxial graphene and bare hydrogen (H)-etched SiC (6H-SiC (0001)) at room temperature and pressure of 2×10^{-10} torr. Robust coupling of about 130 meV (much higher than 20 meV measured from the coupling of the SPP to SPhP modes in GaAs[235]) was observed between the dipolar E fields[236]. This coupling originated from the collective oscillation of π-electron charges in graphene and the collective vibrations of SiC. The carrier density of graphene was recorded to be in the range of $10^{13}\ \mathrm{cm}^{-2}$ as a result of the charge transferred from the surface of SiC to the graphene sheet[26]. The momentum of phonon modes in SiC caused these transferred charges to oscillate, a phenomenon which is understood to be the source of unusually strong anti-crossings observed in the measured dispersion curve of the coupled system (see Figure 3.5a). Subsequently, Kosh, Seyller & Schaefer conducted another study about plasmon and phonon coupling where high-resolution electron energy loss spectroscopy (HREELS) was utilised to reveal strong coupling of these modes in graphene on 6H-SiC (0001) with a higher carrier density in the range of $1.5 \times 10^{15}\ \mathrm{cm}^{-3}$ at the long wavelength limit[103]. The spectra of energy loss recorded (see Figure 3.4b) confirmed the existence of coupled plasmon and phonon modes separated by ω_{S0} and ω_{T0}. Coupling was also theoretically confirmed in Figure 3.5c, whereby using the dielectric function, the spectra of the energy losses and dispersion of the two coupled modes were calculated. Later, Kosh et al. again realised the coupled phonon-plasmon modes in EG on SiC[237]. Their study used HREELS and a dielectric function model to unveil coupling for epitaxial graphene to the buffer layer and in quasi-free standing graphene on both oxygen and hydrogen-intercalated SiC (0001) (See Figure 3.5d-f). They revealed the coupling of internal modes to occur even for bilayer graphene with asymmetric inversion, which results from disparity of charges across the layers. They also revealed that interface modification through intercalation cannot quench plasmon-phonon coupling in the EG on SiC substrate.

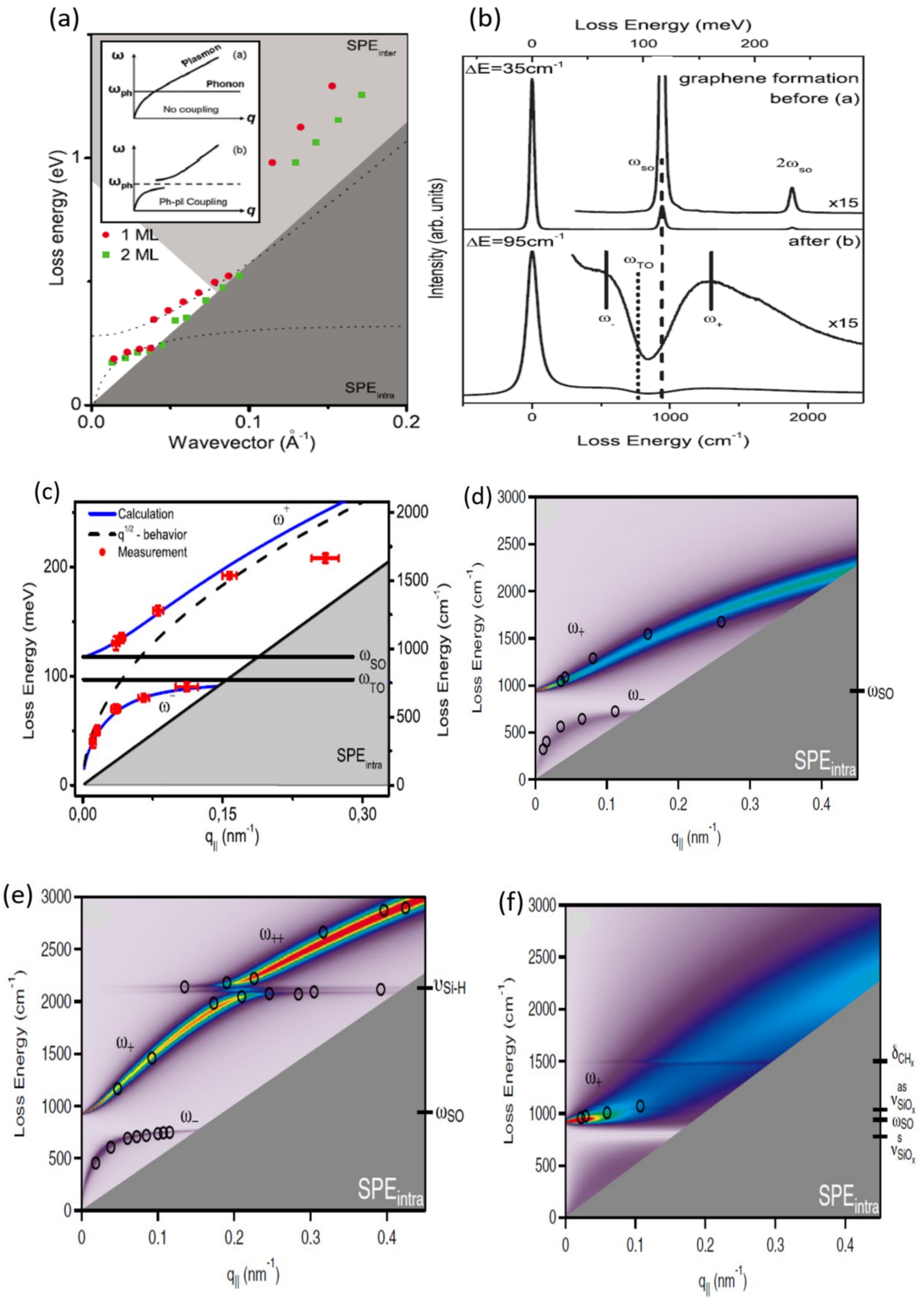

Figure 3.5. (a) Graphical representation of the peaks energy losses against wavevector in monolayer (ML) and bilayer graphene on SiC. The dashed surfaces show the area covered by single-particle excitation (SPEs) spectrum results from inter-band and intra-band transitions, while the two insets show plasmon and phonon modes before (top) and after coupling (bottom), adapted with permission from [26]. ©2010 American Physical Society. (b) Spectra of energy loss (measured by HREELS at the

resolution of 20 cm^{-1}) of hydrogen etched SiC (before graphene formation on top) and on EG SiC (001) after formation of graphene (bottom curve), (c) dispersion of SPhP-SPP modes coupled (red dots and solid blue lines represent measured and calculated results, respectively. The dashed line describes the nature of $q^{1/2}$ b &c adapted with permission from [103]. ©2010 American Physical Society. (d) Dispersion of plasmon-phonon coupled modes on monolayer graphene on SiC, (e) dispersion of plasmon-phonon coupled modes hydrogen-terminated EG on SiC (0001), and (f) dispersion of plasmon-phonon coupled modes for oxygen terminated EG on SiC (0001). The coloured images (blue and red) show the coupled plasmon-phonon modes and are marked by ω_{-}, ω_{+}, and ω_{++} while the back and white circles indicate the maximum energy losses as measured with HREELS recorded at different primary beam energies. (d-f)adapted with permission from[237]. © 2016 American Physical Society.

Moreover, the strong coupling of SPPs to localised SPhP modes in graphene and periodic gratings (micro-cavities) fabricated into SiC substrates (to induce localised and propagating modes in the system) was theoretically studied for tunable SPPs at infrared frequencies[31]. In that study, they considered monolayer graphene on a SiC grating, and they used numerical calculations with the finite element method (FEM)[238] to investigate the optical responses. It was reported that as SiC will behave as a near-perfect reflector within the Reststrahlen band, this can enable a cavity effect sufficient to launch graphene SPP standing waves[96]. Rabi splitting in the absorption spectra confirmed the presence of strong coupling of the localised SPhP resonant modes supported on the SiC grating and SPP resonances in graphene cavity modes. The resultant hybrid mode displayed the characteristics of each constituent (SPPs in graphene and SPhPs modes in SiC). The tunability of the mode in their device was also revealed by varying the chemical potential of graphene and by changing the cavity width, where they observed a shift in absorption peaks. Moreover, Qing et al.[173] theoretically demonstrated that an ultrathin layer of MoS_2 and hBN sandwiched between SiC and graphene can support extremely confined SPhPs with confinement factors over 100 and a tunable hybrid SPP-SPhP mode, which was used for an electro-optic modulator with over 95% of modulation depth. Further works on the hybrid coupling of the SPP-SPhP modes in EG on SiC were performed in the following references[32, 232, 239-241].

3.3. Summary

This chapter reviewed different graphene growth techniques such as micromechanical exfoliation of single-crystal graphite, CVD, thermal decomposition of silicon carbide, and direct graphene growth on silicon through heteroepitaxial cubic silicon carbide. The chapter revealed tremendous progress in terms of graphene synthesis techniques. The recent progress on the quality and control of epitaxial graphene grown on silicon carbide on silicon carbide showed more potential advantages due to its large wafer growth and compatibility with existing silicon processing technologies that enable the fabrication of any complex three-dimensional structures and optical characterization of graphene together with silicon carbide.

The chapter also reviewed the recent progress in graphene and silicon carbide-based nanophotonics and revealed significant progress for graphene plasmonics and silicon carbide nanophotonics individually for the past few years. The reviewed literature revealed that the coupling of graphene and polar materials improves photonic devices' performance significantly. However, only a few works were conducted on combined graphene -silicon carbide materials systems, despite recent progress on EG/SiC on a silicon substrate that eases the fabrication of photonic devices of any shape using existing CMOS technologies. Hence further studies need to be conducted on EG/SiC/Si.

Chapter 4. Methodology

4.1. Experiment

4.1.1. Graphene synthesis - A catalytic alloy graphene growth on epitaxial silicon carbide on silicon

In this project, commercial 3C-SiC films heteroepitaxially grown on (100) silicon substrates (3C-SiC/Si(100)) of 2 inches supplied from NOVASiC, France, were employed for the experimental results reported in chapter 5. For experiments performed in chapter 6, 3C-SiC nanowires on the silicon substrate (3C-SiC NW/Si) from IMEM-CNR Institute, Italy, were used. The 3C-SiC/Si wafers were diced into small samples of ~1 cm ×1 cm size for characterisation and graphene growth.

The diced 3C-SiC /Si samples were then graphitised using an alloy mediated catalytic process, a novel technique developed by our research group for epitaxial graphene growth [33, 35]. Our alloy-mediated catalytic graphitisation process involves three fundamental steps to synthesise epitaxial graphene on silicon carbide on silicon. The three steps are depicted in Figure 4.1.

The first step is the sputtering or deposition of catalyst metals on 3C-SiC on Si samples. This step begins by cleaning the samples using acetone and isopropyl alcohol (IPA) solution. The cleaned samples are then loaded into a cryopump deposition chamber with a vacuum pressure of ~ 10^{-5} mbar and a deposition current of 200 mA for nickel's (Ni) and copper (Cu) deposition on 3C-SiC/Si. After deposition of catalyst metals, alloy–mediated graphitisation step follows using a carbolyte high-temperature furnace. In this step, the samples are annealed at ~ 1100 ºC (25º C/min) for one hour under the controlled vacuum condition of ~ 10^{-5} mbar, and the samples remain in the furnace to gradually cool down (at ~2 ºC /min rate) to room temperature[33]. During the annealing phase, Ni reacts with SiC, which results in the formation of silicide groups, typically the Ni_2Si, intermixed with metals while releasing the carbon, which precipitates during the cooling phase. The intermixed layer of metal silicides, metals, and excess carbon that did not participate in graphene formation get removed by a wet freckle etch process that uses a mixture of acid solutions. The freckle solution consists of a mixture of 85% of phosphoric acid (H_3PO_4):Glacial acetic acid (CH3COOH):70% Nitric acid (HNO_3):48% Tetraflouroboric acid (HBF_4): H_2O in the ratio of 70:10:5:5:10. Lastly, the samples are rinsed using milli-Q water and dried with nitrogen gas[242].

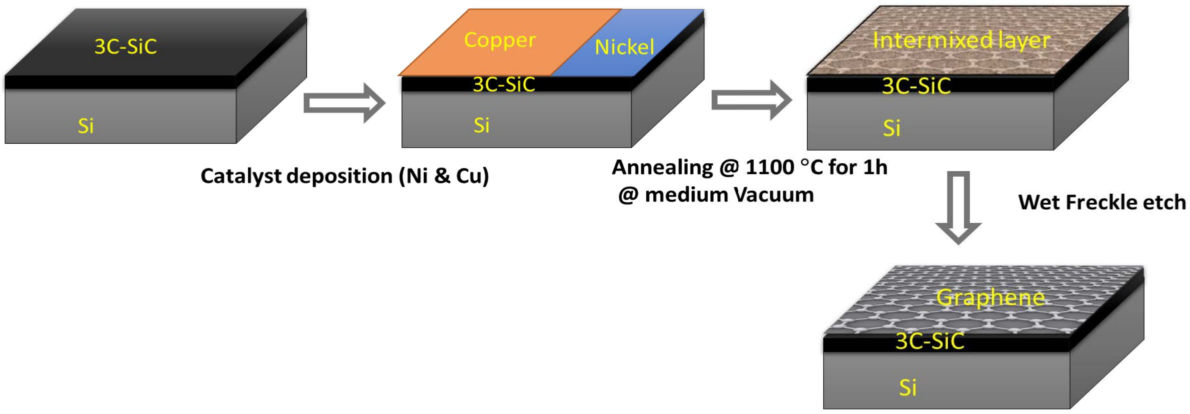

Figure 4.1. A schematic representing alloy mediated catalytic graphitisation of epitaxial graphene on cubic silicon carbide on silicon[33].

4.1.2. Scanning Electron Microscope

A scanning electron microscope (SEM) is an electron microscope that generates images of a sample. SEM employs a focused beam of electrons to illuminate and collect detailed and complex properties of the sample and display them in the image and topological form. SEM can magnify the sample from 10 to 3×10^5 times. Modern SEM had been improved that can have a resolution as high as 1 nanometer, making it a powerful tool for micro and nanostructures research[243].

To characterise the surface morphology of our samples in this thesis, we used a Zeiss SUPRA 55- VP high–resolution field emission SEM operated by the accelerating voltages ranging from 2 kV to 10 kV.

4.1.3. Raman Spectroscopy

Raman spectroscopy is an optical tool used for measuring the vibrational energy in molecules. With Raman spectroscopy, it is possible to distinguish various elements present in the sample. This tool is usually considered as a complement to IR spectroscopy. This is because IR and the Raman spectroscopies have different selection rules for the surface vibration modes excitation[242]. For IR spectroscopy, a change in the molecule's dipole moment during vibration is required to initiate interaction with the incident EM fields. However, for a vibration mode to be Raman active, a change in the polarizability is necessary. Also, while the IR spectroscopy measurement relies on the interaction between molecule and incident radiation, the Raman technique depends on the inelastic scattering in which the molecules loses or gain energy before re-radiating the incoming radiation[242]. The difference between Raman scattering and infrared absorption processes is depicted in Figure 4.2. When the incident EM field on the sample is elastically scattered, the phenomenon is called Rayleigh scattering. Otherwise, the phenomenon is called Raman scattering when it is scattered inelastically, either blue shift/anti-Stokes or red-shift/Stokes.

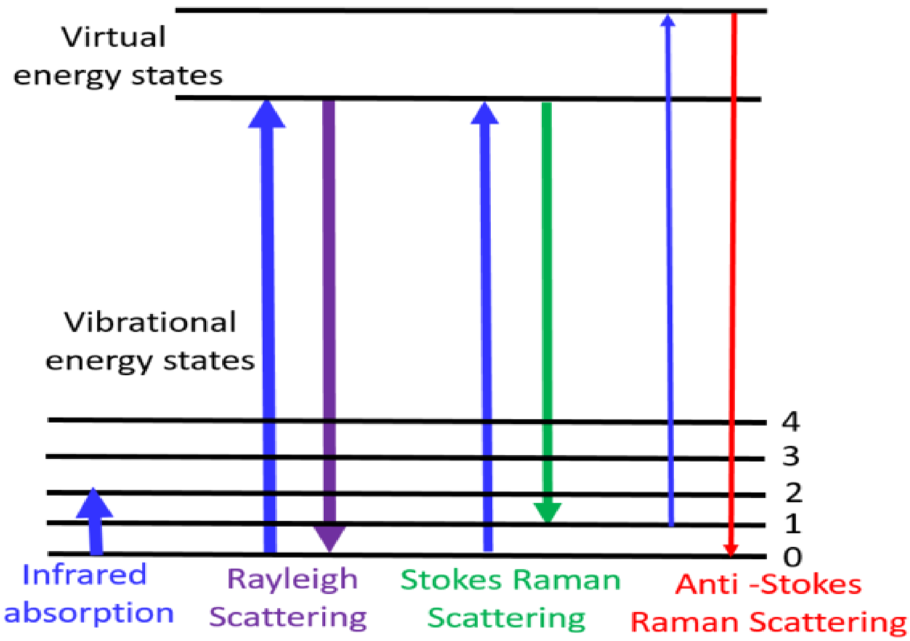

Figure 4.2. A schematic representation of infrared (IR) absorption, Rayleigh, and Raman scattering processes. The IR absorption is induced by a direct increase in the absorption energy; Rayleigh scattering comprises an elastic process in which the scattered and incident waves have the same energy; the Raman scattering takes place when the incident fields gain/loses energy as they interact with a vibrational excited/unexcited molecular system[242].

For the measurements with Raman spectroscopy, a laser as a monochromatic light source is required. The latter emits the radiation which hits the sample, and the vibration states of the sample are recorded as a spectrum of phonon modes (typically as wavenumber versus Raman intensity).

We used WITEC confocal Raman microscope and Renishaw inVia Raman microscope to characterise our samples in this thesis. For simplicity, we only discuss the WITEC Raman Renishaw measurement procedure in this chapter, while inVia Raman is discussed in chapter 6. WITEC confocal Raman microscope mapping (Figure 4.3)[244, 245], was used at room temperature in a backscattering geometry with a WITec ultra- high throughput spectrometer (UHTS) excited by 532nm (argon-ion) laser using 100X objective with a spot size of ~300 nm. Silicon was used as a reference sample to calibrate the instrument before Raman spectroscopy measurements to ensure that the Si peak's spectra position is at ~520 cm^{-1}.To keep statistical accuracy in measurement, we performed an area mapping of 10 µm × 10 µm with 0.2 µm and 0.1-second step size and integration time, respectively.

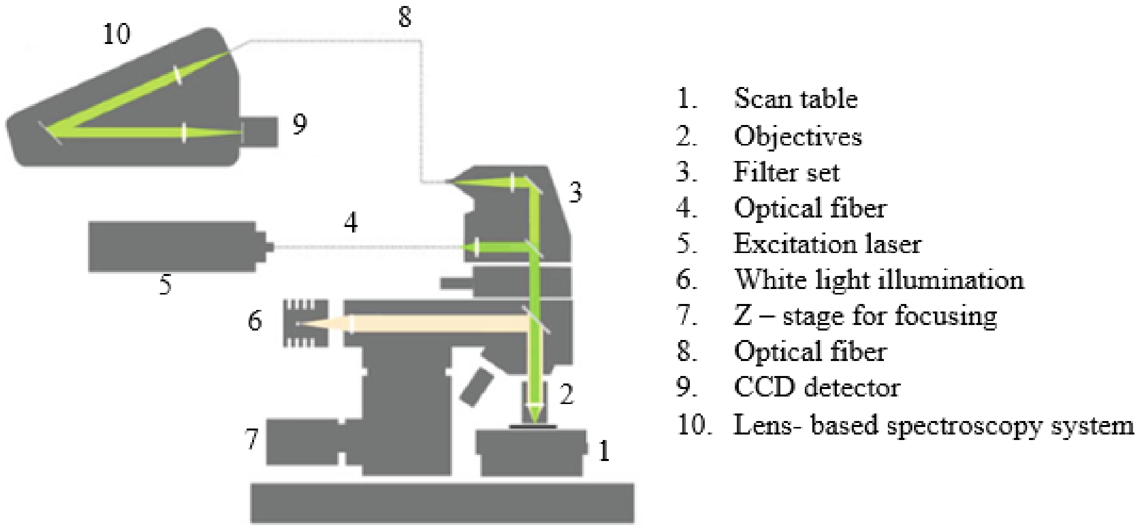

Figure 4.3. A schematic of a WITEC confocal Raman microscope. Adapted with permission from[244], © 2018 Springer International Publishing AG.

The Raman spectral positions of the D, G, and 2D bands of graphene were identified, and their intensities ratio (I_D/I_G) was calculated and recorded to evaluate the quality of the produced graphene samples. Typically the D peak appears only for the broken graphene's lattice symmetry, and its presence indicates the structure defects in graphene, such as edges and point defects[28]. The G peak in the Raman spectra of graphene arises from the in-plane vibrational mode (C-C bond in graphitic materials) due to the SP^2 hybridisation of carbon atoms. Raman intensities for the D and G peaks (I_D/I_G) ratio provide the information needed to approximate the graphene defects, where a lower ratio indicates less defective graphene. Moreover, the following relation[246]:

$$L_a = 2.4 \times 10^{-10} \lambda^4 \left(\frac{I_D}{I_G}\right)^{-1} \tag{4.1}$$

can be used to estimate the grain size of graphene from I_D/I_G and the laser's wavelength for the Raman spectrometer.

4.1.4. Fourier transformed- infrared spectroscopy

Fourier transformed infrared (FT-IR) spectroscopy is a powerful and widely used technique to identify and characterise the samples' transmission, reflection, and absorption properties in the infrared spectrum. Currently, FTIR can measure and provide the samples' spectra properties at the far-infrared, mid-infrared, and near-infrared, with only the differences being on the detectors, beamsplitters, filters, or lenses used by the tool[242]. Interferometer and Fourier transform computation are the two vital parts of an FTIR. A schematic of an interferometer is depicted in Figure 4.4. The interferometer provides information on the interference pattern between two light beams. The light beam leaving an infrared source enters into the interferometer, divided into two single light beams. After the two beams have moved through their separate paths, they couple to form one light beam and leave the interferometer. The optical path difference (OPD) of an interferometer can be defined as the difference between the distances travelled by the two different light beams. When two distinct light beams travelled equal distances, the OPD of the interferometer becomes zero, a condition which is known as zero optical path difference (ZOPD).

Different FTIR manufacturing companies use different interferometer designs, but most modern FTIRs use the Michelson interferometer, named after its inventor Albert Abraham Michelson[247]. Here we used the Michelson design to explain the interferometer's working principle, which is also applied to different interferometer types used in modern FTIRs.

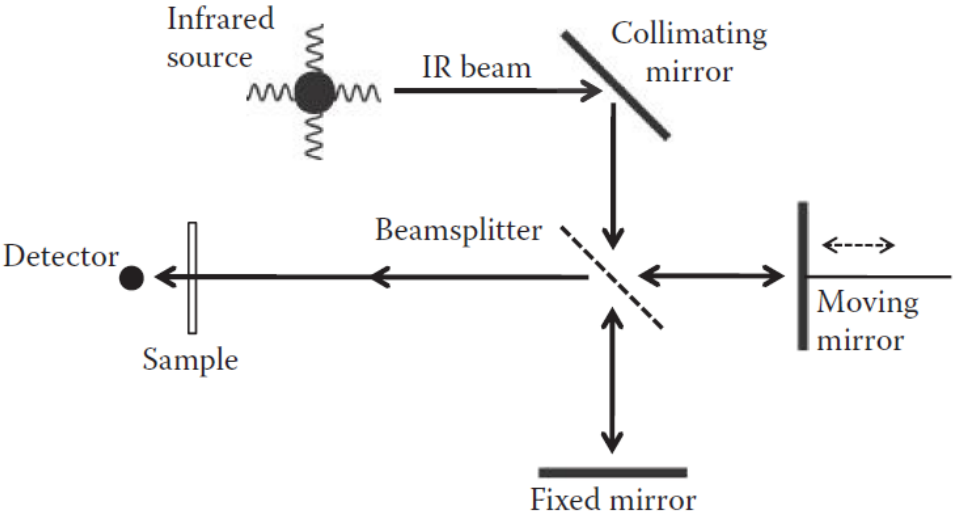

Figure 4. 4. A schematic of Michelson interferometer. Adapted with permission from [247] , © 2011 by Taylor & Francis Group, LLC.

As depicted in Figure 4.4, Michelson consists of four major components. The top part contains the infrared light source (ILS) and a collimating mirror (CM), which collects the light from the ILS and causes the beams to move parallel to each other. The bottom part contains a fixed mirror (FM). On the right, the Michelson interferometer has a moving mirror (MM), moving right and left. The left side of the Michelson interferometer has an infrared detector and the sample holder, while the central component of the interferometer is an optical beamsplitter. A beamsplitter is made to transmit part of the incident light beam while reflecting the other light incident on it—the transmitted light from the beamsplitter moves toward FM. Upon reflecting from these mirrors, the reflected light beams move back to the beamsplitter, where they recombine to form a single light beam which leaves the interferometer to interact with the samples and be collected by the detector. Recombination of the two light beams reflected from the moving and fixed mirror follows the superposition law of the two waves[248].

$$\mathrm{A_f = A_1 + A_2} \tag{4.2}$$

where $\mathrm{A_f}$, $\mathrm{A_1}$, and $\mathrm{A_2}$ describe final amplitude, fixed mirror light beam amplitude, and moving mirror light beam, respectively.

For $\mathrm{A_f}$ with higher intensity than $\mathrm{A_1}$ or $\mathrm{A_2}$, the recombination of the two light beams is called constructive interference, whereas for $\mathrm{A_f}$ lower than $\mathrm{A_1}$ or $\mathrm{A_2}$ indicates destructive interference. The intensity of the light beam is directly proportional to the square of its amplitude. Therefore, the name interferometer is given to the instrument because the two light beams interfere in the interferometer, which measures their interference pattern.

How does the interferometer produce the spectrum?

It is worth knowing how the interferometer produces a spectrum. Let us assume that the IR source excites light composed of only one wavelength, λ (typically, the IR source in FTIR excites light with several wavelengths)[247]. We can also consider a situation where an interferometer is at ZOPD. This implies that the speed and distance travelled by the light beam reflected from the fixed mirror and the light beam reflected from the moving mirror are equal. Consequently, at the beamsplitter, the two light beams recombine constructively. When the OPD of these two light beams is in phase, the following relation between the OPD and wavelength needs to be respected.

$$\mathrm{OPD} = \mathrm{n}\lambda \tag{4.3}$$

where n= 0, 1,2, ….. represents an integer number. While n=0 corresponds to ZOPD, and n=1 indicates a situation where the light beams are precisely one cycle out of phase, while n=2 corresponds to the case when the light beams are two cycles out of phase. For a non-zero OPD between the two beams, the moving mirror's distance in an interferometer is called the mirror displacement (MD). Thus, as the light beam traverses from and to the moving mirror, the OPD corresponds to 2MD. For example, a mirror displacement of 1 cm in the Michelson interferometer corresponds to 2 cm OPD. By gradually moving the mirror back and forth from the beamsplitter, constructive and destructive interferences get induced, which produces an interferogram (i.e., interference writing). Here interferogram can be defined as a plot of the light intensity against OPD. The back and forth movement of the mirror from the beamsplitter is called a scan. The interferograms resulting from several scans are Fourier transformed in computer software and produce a spectrum, so the technique is named Fourier Transform Infrared (FTIR) spectroscopy. Figure 4.5 describes the FTIR spectroscopy processes. Further details on the FTIR technique can be found in these references[247, 249].

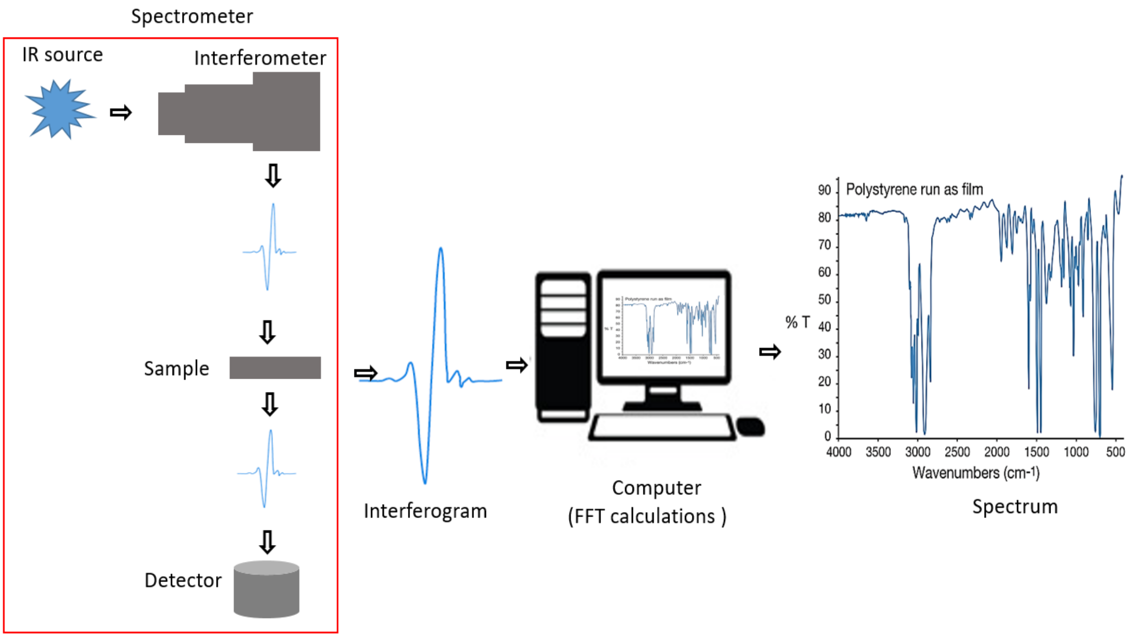

Figure 4.5. A schematic of the FTIR spectroscopy procedures showing spectrometer, interferogram, and computer system from which Fourier transformation calculation takes place to generate a spectrum of results.

FTIR has four main sampling techniques: transmission, specular reflection, attenuated total reflection, and diffuse reflection. Nevertheless, attenuated total reflection (ATR) is commonly used to analyse the samples qualitatively with less sample preparation. The main advantages of ATR sampling arise from the small sampling path length and the depth of penetration of the infrared beam into the sample. Moreover, it is used to analyse the surface plasmon or phonon polariton responses in the samples. Typically this is good for flat samples, where the ATR sampling technique offers the opportunity to excite these surface polariton modes, and the instrument crystal, usually a high refractive index prism, acts as a coupler to provide the light with enough momentum matching that of surface plasmon or surface phonon mode in the characterised samples for the polariton modes excitation.

In this thesis, a Thermo Scientific Nicolet, 6700 FTIR spectrometer, connected to ATR (diamond crystal) accessory, was used to measure the investigated samples' reflectance and absorbance characteristics.

4.2. Numerical modelling

Numerical modelling has become an essential part of science and engineering, thanks to computational power and software development advancements. The numerical methods involve using physics laws and mathematical models to design and predict the intended final product's performance.

Typically, it is challenging to know the exact behaviour of an actual complete system or different components of a system before being tested for the designed purpose. Designing and testing the system's behaviour usually results in excessive materials/samples and time consumption from the design to the production stage. In most cases, this practice is cost-ineffective. Consequently, the designers prefer using numerical software to simulate, optimise, and refine the designed system before the final physical prototype is manufactured. The simulation and numerical modelling tools play a significant role in reducing the design process's duration and the final product's total cost and exploring the new phenomena that may not be revealed experimentally due to the absence of technologies to disclose them. Nowadays, modelling and simulation techniques in the photonics research field have gained immense progress where new numerical and analytical methods have been developed, and existing ones have been upgraded to meet the researchers' purpose. Additionally, the advancement of computing power and software development enabled commercially available software and simulation tools for improving the numerical modelling of various photonic devices. Generally, these simulation tools need to be robust, accurate, fast, and user-friendly with significantly low memory and computational requirements.

Several types of numerical modelling techniques for photonic devices have been developed to meet the users' needs. Most of the invented numerical methods focus on mathematics, physics, chemistry, and engineering problems, while others had been successfully implemented to solve other disciplines' research problems[250].

Traditionally, analytical calculation methods and closed-form solutions have been predominantly used to model different photonic devices[250]. However, as the devices increasingly became more complex and analytical techniques became significantly ineffective, numerical modelling methods became a better alternative route. Additionally, this was empowered by the tremendous advancement in software development and low-cost computing power, enabling automation and computerising numerical algorithms.

Consequently, it is now possible to simulate complex structures using commercially developed software based on different numerical methods. Some of the extensively used numerical techniques for photonic modelling are the transfer matrix method[251], finite difference time domain[252], finite integration technique[253], finite element method[250, 254], transmission line matrix methods[255, 256], and many others. These techniques approximate the solutions of Maxwell's equations, which is the starting point for any investigation on the photonic devices using numerical methods.

The finite element method (FEM) used in this thesis is regarded as one of the most effective modelling techniques for investigating various optical phenomena in photonic structures. Thus, the following section discusses the basic principles of FEM, focusing on photonic device modelling using COMSOL Multiphysics.

4.2.1. Finite element method

The finite element method (FEM) is one of the leading numerical modelling techniques first introduced in the 1940s[257]. In the beginning, FEM was used for structural analysis and aircraft designs[258]. Thanks to its flexibility and ability to produce accurate and robust results for many challenging problems, FEM was later expanded to other science and engineering branches, such as heat transfer and fluid dynamics[259], electrical engineering[260], and electromagnetics[261-264]. In electromagnetic modelling, the FEM is used to find numerical solutions of partial differential equations (PDEs) or ordinary differential equations (ODEs) of boundary value problems[265, 266]. The boundary value problems generally result from the coupling of the governing PDEs and boundary conditions (Figure 4.6). The boundary conditions can be expressed in terms of mathematical equations. However, due to the complexity of mathematical equations representing the boundary value problems, it is not easy to solve them manually. Consequently, FEM uses a set of algebraic equations to approximate a solution to the problems.

Figure 4.6. General description of boundary value problems

The FEM computation involves four fundamental steps[267]: 1)segmentation of the structure into finite elements, 2)creating the governing equations for each element, 3)collection/assembly of all elements into a system of equations, and 4)finding the solutions of the system of equations.

Segmentation of the structure geometry consists of dividing the geometry of the complex structure/problem into numerous small parts ‘’elements” such that the dielectric is homogeneous in every element (Figure 4.7). This process is also known as “mesh discretisation.” The meshed structure results in small and simple elements with different geometrical shapes such as triangles, quadrilateral, tetrahedron, or hexagonal shapes, depending on the dimension of the original object “domain” and the capacity of available computational resources[266, 268]. In this thesis, triangular and tetrahedron meshes will be considered for our FEM models[269]. Usually, 2D models tend to use triangular-shaped meshes, while 3D models tend to combine triangular and tetrahedron meshes[254, 265]. These meshes are interconnected in the FEM model with nodal points called nodes and boundary lines. Figure 4.7b illustrates mesh, nodes, and boundary lines. At the connecting nodes, each adjacent element shares the degree of freedom equal to the product of the number of nodes and the values of field variables.

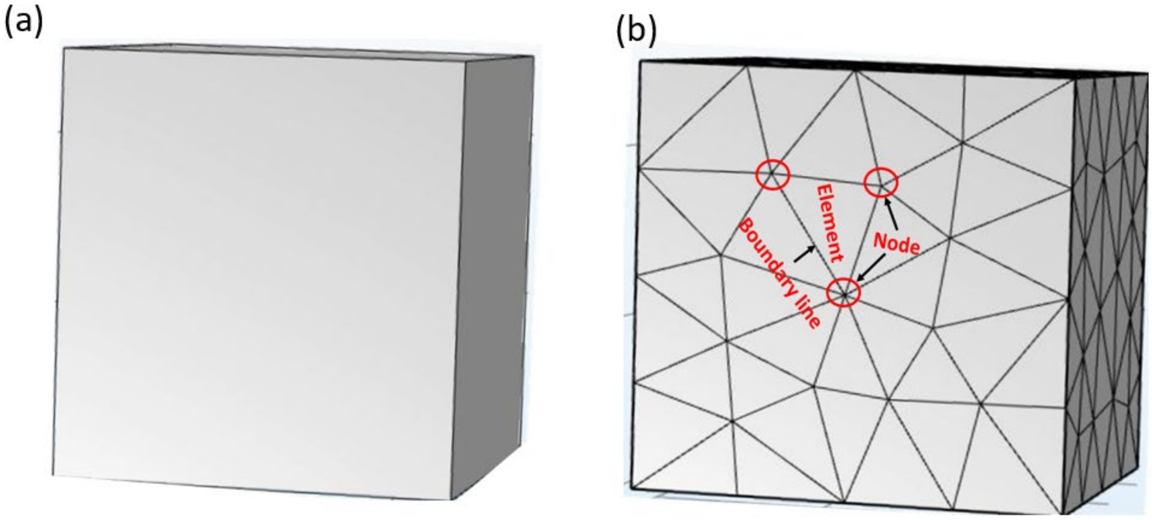

Figure 4.7. A schematic illustrating mesh discretisation in a FEM model. a) An object or model domain before mesh discretisation, b) model domain after mesh discretisation showing the nodes (red circle) interconnected by boundary lines to form an element (triangular shape).

In FEM, the computational space, also called the model domain (Figure 4.7a), is divided into a finite number of subdomains. There are several advantages of using subdomains. Subdomains can represent complex geometry and different material properties more accurately. They divide the original problem into a smaller set of simple problems; hence, they can be structured to collect more information. This solves the problem more efficiently as the FEM-based software can automatically generate the mesh using built-in algorithms. If the field distribution in each element e assumed to be φ^e, the distribution over the entire FEM structure is a linear combination of every element's distributions and can be described by the following relation;

$$\varphi(x,y) = \sum_{e=1}^{N_e} \varphi^e(x,y) \tag{4.4}$$

where N_e represents the number of elements constituent of the structure being investigated. In FEM, N_e is to be chosen such that the maximum length of the element's edge is less than a tenth of the free space wavelength$\left(\lambda_0/_{10}\right)$.

The second step in FEM modelling is developing the governing PDEs for each element. In setting up the FEM model, variational and Galerkin formulations can be used[250, 265]. Though the two formulations have different starting points, they can yield expressions that can be discretised with the FEM technique and converged to eigenvalue matrix equations[250, 265]. The variational approach requires reducing an expression/functional setup in terms of variables such as potentials and the fields with respect to the slight variation in these variables. The main principle for the variational approach is that for very small variation, the functional is stationary while the system reaches its equilibrium. The Galerkin formalism is a form or example of the weighted residual method, and it starts by creating a residual directly from the PDE connected to the boundary value problem being analysed[265, 270]. The residual is created by transferring all terms of the PDE on one side. Afterwards, the created residual is multiplied by a weight function and integrated over the domain of a single element. This is why the Galerkin formulation is a form of the weighted–residual method[264]. Galerkin's formulation was explained in a number of the FEM modelling textbook [250, 254, 264, 267, 271]. For simplicity in this chapter, we limit our discussions to the variational method.

The distribution of field variable φ for every element is extended in an appropriate basis function ψ_i^e. The ψ_i^ecan be either edge or node-based functions. For simplicity, here, it is taken to be a node-based function. The basis functions only contain a value over the element, and they disappear outside of the element, e. Moreover, the basis functions use the boundary conditions to influence the field value in the adjacent elements. To effectively represent φ^e , the basis functions have to form a complete set. The limited capacity of computation tools restricts the basis functions used in the FEM model to a few numbers, which are generally determined by the governing differential PDE equations through a continuity condition.

The expansion can be realised with the following expression by taking an element e with the nodes p.

$$\varphi^e(x,y) = \sum_{i=1}^{p} C_i^e \psi_i^e(x,y) \tag{4.5}$$

where C_i and ψ_i^e describe the unknown complex coefficients and the basis functions, respectively. The unknown complex coefficients, C_i, can be determined by substituting (4.5) into the governing differential wave equations (2.14). With variational functionals, an average satisfaction of the differential equations may be realised utilising the following expression[265].

$$F^e[\varphi^e] = \frac{1}{2}\iint_S [|\nabla\varphi^e|^2 - k^2(\varphi^e)^2]\, dxdy \tag{4.6}$$

where $[F^e]$ describes a set of equations to be solved for each element in a FEM model.

After this stage, an assembly phase follows. During the assembly phase, the structure/problem being simulated gets simplified to generate more sparse matrices, which can be solved to generate the unknown vector φ. There are several variable solvers such as lower- upper(L-U) decomposition, also called factorisation[267], parallel direct sparse solver(PARDISO)[272], and iterative solvers exist for FEM modelling and can be used depending on the problem under investigation.

Currently, different FEM modelling software tools are commercially available on the markets to simulate different photonics. These include but are not limited to Computer Simulation Technology (CST), High-Frequency Structure Simulator (HFSS), Lumerical, COMSOL Multiphysics, and many others. COMSOL Multiphysics has emerged as one of the robust simulation tools widely employed for photonic modelling and other science and engineering problems[268, 269, 273].

In this thesis, COMSOL Multiphysics was used for numerical simulations of our investigated photonic structures. Consequently, the rest of this chapter discusses setting up a FEM simulation model in COMSOL Multiphysics. Our discussion here is limited to the boundary conditions, source, and mesh settings, as these are the main components that require much care for any accurate simulations using COMSOL Multiphysics.

4.3. Building a finite element method model in COMSOL Multiphysics

COMSOL Multiphysics is a powerful simulation tool that uses FEM to model and solve several scientific and engineering problems. COMSOL Multiphysics has a robust working environment with a model builder that assists in designing different models. With COMSOL Multiphysics, various coupled physics phenomena can be solved and analysed. One of the advantages of using COMSOL Multiphysics for FEM modelling is its meshing capability, which can be generated automatically by computer with the software or manually defined and refined by the users. Although the software has a built-in materials property database, it also offers the customer users the opportunity to create their materials based on their desired properties.

4.3.1. Boundary conditions and source set up in COMSOL Multiphysics

Efficient use of boundary conditions is a recommended practice in electromagnetic simulations to reduce the problem's size. It is worth noting that it is challenging to truncate the model's geometry without introducing too many errors. Most simulation models extend to infinity or have some domains where the solution only experiences minor variations. For such a problem, two common approaches are generally used to resolve the model. One is to truncate the model geometry in an appropriate position, while the other is to apply suitable boundary conditions. In static and quasi-static problems, it is generally possible to assume that the fields are zero at the open boundary as long as the source and model are a sufficient distance away from each other.

On the other hand, special absorbing or low reflecting boundary conditions such as the perfectly matched layer (PML) in the order of a few wavelengths away from the source need to be applied to solve radiation model problems[269, 273]. Another occasion where the boundary is used in COMSOL Multiphysics is defining a thin layer in the model. For example, the perfect electric conductor (PEC) or transition boundary condition (TBC) for 2D conductive materials can replace highly conducting materials.

4.3.1.1. Periodic boundary conditions in COMSOL Multiphysics

Periodic boundary conditions (PBCs) can be employed to truncate a simulation model once assumed to be infinitely repeating in a direction with a particular period. The PBCs enable solving any infinite structure provided that a small unit cell/proportion of the whole system can be modelled and that the relationship between each unit cell constituents of the model is known. In some cases, PBCs can also be used to solve isolated structures, provide that the simulation domain is large enough to be sure that the periodicity k- vector is significantly negligible to affect the results[269, 273]. The model's periodicity can be obtained by determining the unique part of the device(unit cell) and analysing the relationship between the fields on one side of a unit cell and the fields on the other side/opposite side[274].

In COMSOL Multiphysics, the implementation of PBCs can be accomplished by using source and destination boundaries of similar shapes, as shown in Figure 4.8a. The software interpolates the source and destination boundaries variables across the boundary elements and sets the required boundary relationships. The established relationship efficiently brings the unit cell together, making a periodic structure.

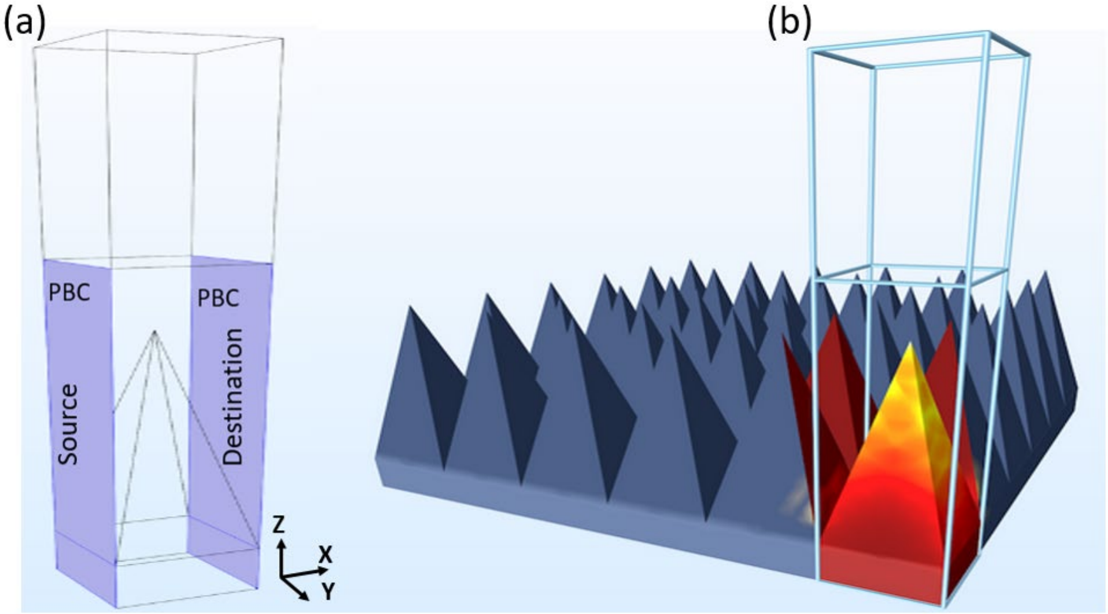

Figure 4.8. A sketch depicting an implementation of periodic boundary conditions in COMSOL Multiphysics. (a) Unit cell showing periodic boundary conditions applied on the sidewall of the model along x-direction indicating the source and destination, (b) an array of periodic structure when the periodic boundary conditions are applied along with x and y- directions of a unit cell. The fields in each are related to the adjacent unit cells by the phase shift. Figure adapted from[275].

There are three kinds of PBCs available in COMSOL Multiphysics[269]: 1) continuity in which the fields variables are equivalent on the source and destination, ($\mathbf{E}_{src} = \mathbf{E}_{\mathrm{dst}}$); 2) antiperiodicity in which the fields at the source and destination have opposite signs ($\mathbf{E}_{dst} = -\mathbf{E}_{src}$); and 3) Floquet periodicity, in which the destination and source are connected by phase shift.

Usually, the phase shift is determined by the period (distance between source and destination) and a wavevector. Implementation of Floquet periodicity in COMSOL Multiphysics is described in Figure 4.8. Assuming a periodic structure described in Figure 4.8b, with PBCs applied on each side of the unit cell, i.e., in x and y- directions, when the model is excited by an oblique incident (θ_i) plane wave, the field scattered at the destination side of the model, can be described by the Floquet-Bloch theorem[274, 276-278].

$$\mathbf{E}_{\mathrm{dst}}(\mathrm{x,y,z}) = \begin{cases} \mathbf{E}_{\mathrm{src}}(\mathrm{x} + \mathrm{x}_p, \mathrm{y}, \mathrm{z}, \omega)\mathrm{e}^{\mathrm{i}(\mathrm{k}_x x_p)} \\ \mathbf{E}_{\mathrm{src}}(\mathrm{x}, \mathrm{y} + \mathrm{y}_p)\mathrm{e}^{\mathrm{i}(\mathrm{k}_y \mathrm{y}_p)} \end{cases} \tag{4.7}$$

where, $\mathbf{E}_{src}$ and $\mathbf{E}_{dest}$ describe the electric field at the source and destination, respectively. $\mathrm{k}_x^i = -\mathrm{k}_0 sin\theta_i$ and $\mathrm{k}_y^i = -\mathrm{k}_0 sin\theta_i$ represents wavevectors of an incident plane wave whereas x_p and y_p denote the period in x and y coordinates.

4.3.1.2. The transition boundary condition for the simulation of 2D conductive materials

As hitherto mentioned, the boundary condition can be used to simulate thin layer geometry like graphene and other 2D materials. In COMSOL Multiphysics, a thin layer can be simulated with impedance matching boundary or transition boundary conditions (TBC)[269, 279]. The latter was used to simulate graphene throughout this thesis, and it is discussed in this section.

The transition boundary condition is usually employed on the interior boundaries to simulate a sheet of a material that initially is geometrically thin but does not necessarily need to be electrically thin. It is typically used to model a thin conductive layer with a relatively smaller size than the thickness and curvature of the object being simulated ($\mathrm{d} \ll \mathrm{L_c}$). That is, for example, the case of conductive 2D materials such as graphene and h-BN. Here d describes the thickness of the ultrathin conducting layer being considered for TBC and $\mathrm{L_c}$ represents the characteristic size and the curvature of the object being simulated. The TBC can also still be employed when a conductor's thickness is much thicker than that material's skin depth[279, 280]. The TBC suggests a discontinuity in the tangential electric field($\mathbf{E}_\mathrm{t}$) and can mathematically be described by electric field discontinuity and the induced surface current density($\mathbf{J}_\mathrm{s}$) relationship[269].

$$\mathbf{J}_{\mathrm{s1}} = \frac{\mathrm{Z_S}\mathbf{E}_{\mathrm{t1}} - \mathrm{Z_T}\mathbf{E}_{\mathrm{t2}}}{\mathrm{Z_S}^2 - \mathrm{Z_T}^2} \tag{4.8}$$

$$\mathbf{J}_{\mathrm{s2}} = \frac{\mathrm{Z_S}\mathbf{E}_{\mathrm{t2}} - \mathrm{Z_T}\mathbf{E}_{\mathrm{t1}}}{\mathrm{Z_S}^2 - \mathrm{Z_T}^2} \tag{4.9}$$

The indices 1 and 2 denote different sides of the film/boundary (see Figure 4.9) whereas Z_S and Z_T describe surface and transfer impedance, respectively, and can be estimated using the following expressions.

$$Z_S = \frac{-i\omega\mu}{k}\frac{1}{\tan(kd)} \tag{4.10}$$

$$Z_T = \frac{-i\omega\mu}{k}\frac{1}{\sin(kd)} \tag{4.11}$$

where k represents the propagation constant and can be calculated using (3.12),

$$k = \omega\sqrt{\left(\varepsilon + \left(\frac{\sigma}{i\omega}\right)\right)\mu} \tag{4.12}$$

Here σ represents the conductivity of the layer while ε and μ define permittivity and permeability of the conducting layer, respectively.

Implementation of TBC in COMSOL Multiphysics is described in Figure 4.9. In COMSOL Multiphysics, the TBC takes the material properties (i.e., refractive index/permittivity, permeability, and conductivity) and the film's thickness as input to the model, then computes the impedance (Z), surface, and transfer impedances of the conductive ultrathin layer. These permit the current (J_s) flowing on both sides of the film's surface to be connected.

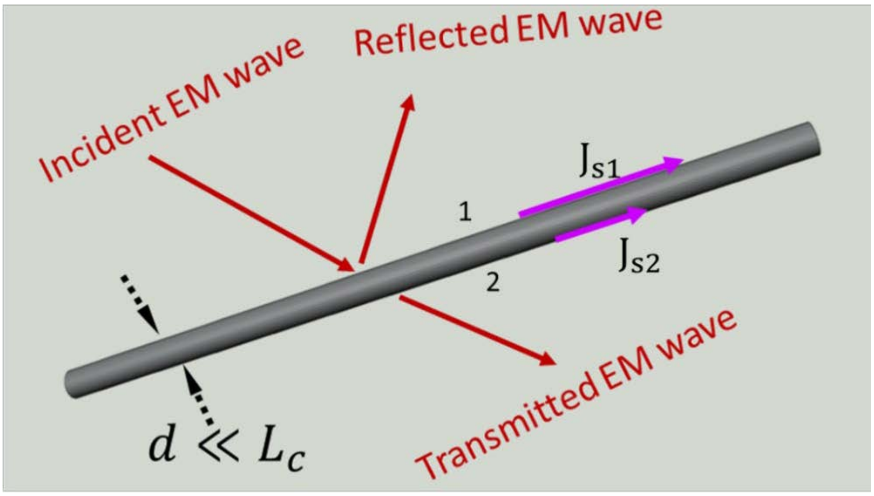

Figure 4.9. Schematic showing how the applied transition boundary condition computes the surface currents (purple arrows) on both sides of the boundary[279].

The TBC assumes that the wave propagates in the normal direction in the thin film. As a result, the wave can be incident normal to the direction of propagation, or the wave can refract to propagate in the direction normal to the thin film[269, 280]. The latter condition occurs only for the good conductors.

4.3.2. Source

After applying suitable boundary conditions to solve the model, another vital step in electromagnetic simulation is to define an appropriate electromagnetic wave source to excite the model. In COMSOL Multiphysics, there are three types of sources: point sources, line sources, and boundary sources. The line sources in the 3D formulation are equivalent to point sources in 2D formulations. The way the source is set in a simulation model significantly impacts the quantities computed from the model. The source definition in the COMSOL Multiphysics model depends on the problem's nature and geometry being solved. Generally, utilising boundary or volume sources provides more flexibility than employing line sources or point sources; however, it costs more memory and time to mesh the source domains. This thesis used the boundary sources (ports) to excite the model with an electromagnetic plane wave. An example of a port boundary source is provided in Figure 4.10.

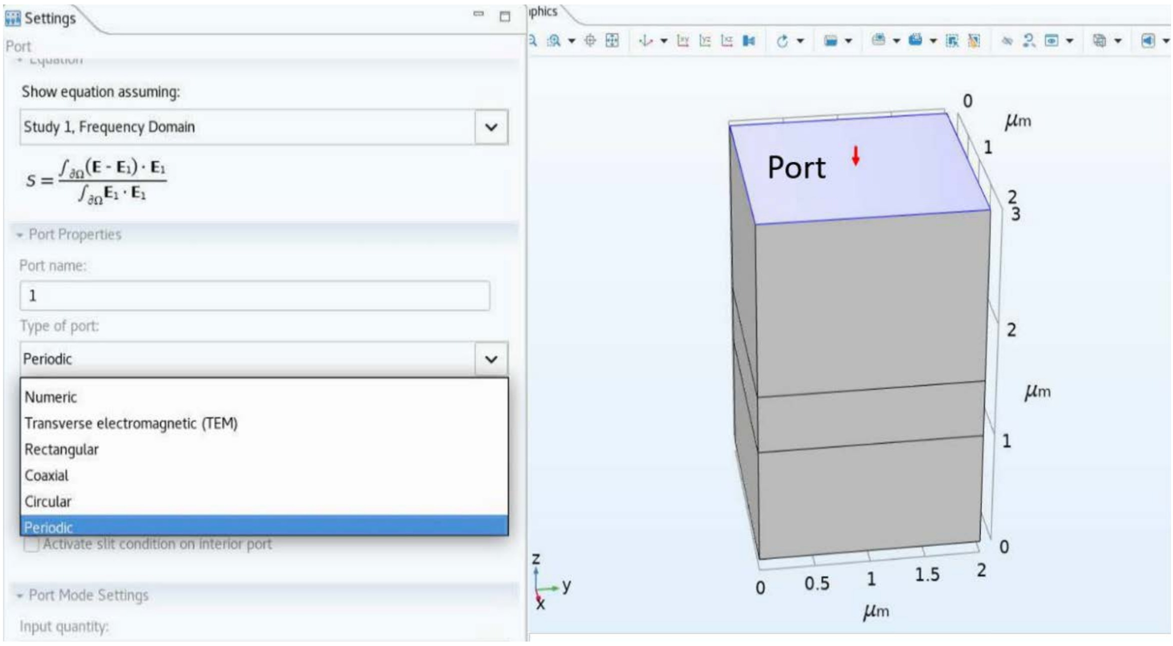
Show equation assuming: Study 1, Frequency Domain

$$S = \frac{\int_{\partial\Omega} (\mathbf{E} - \mathbf{E}_1) \cdot \mathbf{E}_1}{\int_{\partial\Omega} \mathbf{E}_1 \cdot \mathbf{E}_1}$$

Port name: 1

Type of port: Periodic

Figure 4.10. Source boundary (top highlighted in purple) setup in COMSOL Multiphysics, the red arrow pointing down indicates the input port.

It is worth mentioning that the source /port employed to excite the model must be compatible with the applied boundary conditions for accurate simulation. For example, in this thesis, we used periodic ports to match the periodic boundary conditions applied on the sidewalls of our simulation model.

COMSOL Multiphysics provides the opportunity to choose a suitable port from the ports list for accurate simulation of the investigated structure. There are six types of ports in the COMSOL Multiphysics RF module: numeric, transverse electromagnetic, rectangular, coaxial, circular, and periodic port, and each can be assigned to the simulation model depending on the nature of the simulated model and the intended simulation output. In this thesis, we focus more on the periodic port which was used for the simulation of our structures. From the port setting, one has the opportunity to assign input electric or magnetic fields, polarisation, and angle of incident electromagnetic radiation[269].

Ports also were employed here to collect the scattering parameters of the simulated models from which optical properties of the model were obtained in terms of reflectance, transmittance, and absorbance.

4.3.2.1. Scattering parameters and ports

The scattering parameters (S-parameters) are the complex quantities in matrices form, containing the frequency-dependent reflection and transmission of electromagnetic waves at different ports (source or destination) of the devices, such as antennas, filters, waveguides, and transmission lines. The S-parameters have origin from the transmission line theory[255, 269], where they are determined based on the reflected and transmitted voltage waves. However, for the high-frequency EM wave problems like the mid-infrared spectrum investigated in this thesis, voltage is not a well-defined quantity, and instead, S-parameters are expressed in terms of the electric fields[269, 281]. The main advantage of using s-parameters in the simulations is that they enable reflection and transmission coefficients and phases calculations. To accurately simulate S-parameters in a simulations model, all ports (input port and output port) must be connected to match loads/feed, i.e., no reflection directly at the port. For example, consider a model with two ports: input port 1 and output port 2. The scattering parameters representing the reflected (S_{11}) and transmitted (S_{21}) electric fields can be estimated using the expression (4.13) and (4.14).

$$S_{11} = \frac{\int port1\ (\boldsymbol{E}_c - \boldsymbol{E}_1)\,.\,\boldsymbol{E}_1^*)d\boldsymbol{A}1}{\int port1\ (\boldsymbol{E}_1.\boldsymbol{E}_1^*)\ d\boldsymbol{A}1} \tag{4.13}$$

$$S_{21} = \frac{\int port\ 1\big((\boldsymbol{E}_c - \boldsymbol{E}_2).\boldsymbol{E}_2^*\big)d\boldsymbol{A}2}{\int Port1\ (\boldsymbol{E}_2.\boldsymbol{E}_2^*)d\boldsymbol{A}2} \tag{4.14}$$

where E_c is the computed electric field at the port and comprises of the excitation (4.15) and the reflected field (4.16), whereas E_1 and E_2 denote the electric field of the fundamental modes on port1 and 2, respectively.

The computed field on the port containing excitation boundary port (port1) is calculated as follows[269];

$$\boldsymbol{E}_c = \boldsymbol{E}_1 + \sum_{i=1} S_{i1}\boldsymbol{E}_i \tag{4.15}$$

whereas the computed field on the other ports is described by (4.16);

$$\boldsymbol{E}_c = \textstyle\sum_{i=1} S_{i1}\boldsymbol{E}_i \tag{4.16}$$

with i=1, 2, 3,… describes port number.

For the structure with n number of ports, the S-parameters can be estimated using the following S -matrix[269].

$$\begin{bmatrix} \mathrm{S}_{11} & \mathrm{S}_{12} & \mathrm{S}_{13} & \cdots\cdots\cdots\cdots\cdots \;\cdots\cdots & \mathrm{S}_{1\mathrm{n}} \\ \mathrm{S}_{21} & \mathrm{S}_{22} & \mathrm{S}_{23} & \cdots\cdots\cdots\cdots\cdots\cdots\cdots & \mathrm{S}_{2\mathrm{n}} \\ \mathrm{S}_{31} & \mathrm{S}_{32} & \mathrm{S}_{33} & \cdots\cdots\cdots\cdots\cdots\cdots & \mathrm{S}_{3\mathrm{n}} \\ \cdots & \cdots & \cdots & \cdots\cdots\cdots\cdots\cdots\cdots\cdots\cdots & \cdots \\ \cdots & \cdots & \cdots & \cdots\cdots\cdots\cdots\cdots\cdots\cdots\cdots & \cdots \\ \cdots & \cdots & \cdots & \cdots\cdots\cdots\cdots\cdots\cdots\cdots\cdots & \cdots \\ \mathrm{S}_{\mathrm{n}1} & \mathrm{S}_{\mathrm{n}2} & \mathrm{S}_{\mathrm{n}3} & \cdots\cdots\cdots\cdots\cdots\cdots & \mathrm{S}_{\mathrm{nn}} \end{bmatrix} \tag{4.17}$$

The average intensity of the transmitted and reflected power can be calculated as $|\mathrm{S}_{\mathrm{ij}}|^2$.

S-parameters are automatically created by setting up the ports correctly in the COMSOL Multiphysics model and can be extracted for further analysis after the simulation[269]. The names of ports (generally represented by integer numbers) define the variable names.

For the simulation models investigated in this thesis, two ports were used. That is port 1, which is the input port to excite the electromagnetic radiation in the model. The second is the output port; port2 is also known as a listener or receiver port. The software automatically generates the variables S_{11} and S_{21}. The variable S_{11} represents the S-parameter for the reflected wave, while S_{21} contains the S-parameters for the transmitted wave. Moreover, S-parameters can be reported in a dB scale such as $\mathrm{S}_{11}\mathrm{dB}$ and $\mathrm{S}_{21}\mathrm{dB}$, which can be calculated using the following relation.

$$\mathrm{S}_{\mathrm{ij}}\mathrm{dB} = 20\log 10\left(|\mathrm{S}_{\mathrm{ij}}|\right) \tag{4.18}$$

4.3.3. Mesh set up in COMSOL Multiphysics

The finite element method provides the solutions within each element, utilising the simple shaped functions that can be constant, linear, or of a high order. Depending on the model's elements order, coarser or finer meshes are needed to approximate the solution. Generally, there exist three problem-dependent features that define the required mesh resolution[269]:

- First is the change in the solution due to the geometrical features. In COMSOL Multiphysics, the finer meshes get automatically generated where there are several fine geometrical details. Such details should be removed if they do not impact the solution as they produce several unnecessary mesh elements, which also require huge computer memory to simulate.
- The second feature is the skin effect, also known as the field variation caused by the losses. Typically, the skin depth can be estimated from permeability, conductivity, and frequency. More than two linear elements per skin depth are recommended to detect the fields' variation. When the skin depth is not analysed, or a very accurate determination of the dissipation loss profile is not required, the boundary conditions may be used to replace the regions with a small skin depth, thus saving elements. If needed to resolve the skin depth accurately, the boundary layer meshing is appropriate for getting a denser mesh around the boundary.
- The last feature that influences mesh resolution in COMSOL Multiphysics is the wavelength of incident light. To correctly resolve an electromagnetic wave, about ten linear elements per wavelength need to be employed. It is worth noting that the wavelength depends on the model's local material's properties. Section 5.2 of chapter 5 discusses the impact of mesh and mesh element size for COMSOL Multiphysics simulations results.

4.3.4. Dielectric function of silicon carbide and graphene utilised in our simulations

The frequency-dependent complex permittivity measured on our 3C-SiC membrane sample was used as input to our simulated model for the material properties of SiC. The following parameters were extracted from the fit of the measured dielectric function to Lorentz oscillator/TO LO formalism (2.71), and the fit graph is shown in Figure 4.11a: high-frequency permittivity $\varepsilon_\infty = 6.52$, TO and LO phonon frequencies $\omega_{TO=}$ 797 cm^{-1}, $\omega_{LO=}$ 973 cm^{-1} , and damping constant $\Gamma = 12\ \text{cm}^{-1}$.

The effective dielectric function of graphene $\varepsilon_g(\omega)$ was calculated using equations (2.65) described in chapter 2. The following parameter values were used as input for graphene: Fermi energy $E_F = 0.37$ eV, equivalent to the carrier concentration of $1 \times 10^{13}\ cm^{-2}$ as measured with Hall Effect[34], relaxation time $\tau = 370\ fs$, and $T = 300\ K$. The calculated frequency dependent complex permittivity of graphene is shown in Figure 4.11b.

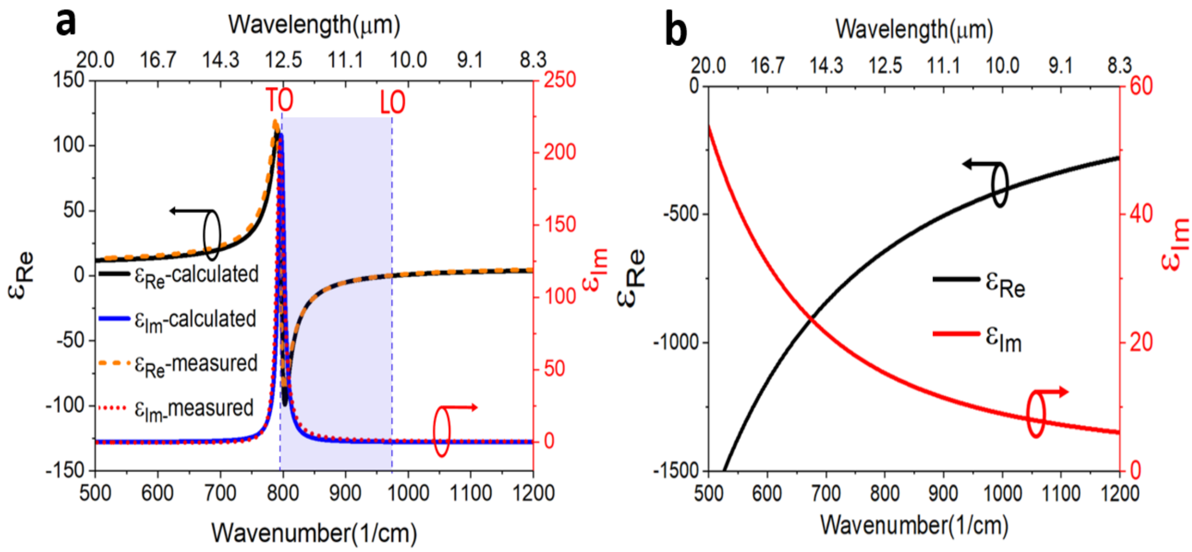

Figure 4.11. Dielectric function of SiC and graphene used in our simulations. (a) A comparison between measured permittivity in 3C-SiC and the calculated permittivity using the TOLO model (2.71) showing the best fit between measurement and calculations when ω_{TO} = 797 cm^{-1}, ω_{LO} = 973 cm^{-1}, ε_∞ = 6.52 and Γ = 12 cm^{-1} used as input parameters in equation (2.71). (b) The calculated permittivity of graphene using equation (2.65). Graphene was simulated as a monolayer with a thickness of 0.33 nm, E_F = 0.37 eV, and τ = 370 fs.

4.4. Summary

In this chapter, we have described the experimental and numerical methods used in this thesis. A catalytic alloy growth process for epitaxial growth of graphene on silicon carbide on silicon substrates was discussed. Then, we discussed the scanning electron microscope and Raman spectroscopy characterisation, Fourier transformed infrared spectroscopy techniques employed for material and infrared characterisation of our samples in this thesis. After clarification of the experimental method, we subsequently discussed the numerical method used in this study. The finite element method which is used for numerical simulation reported in this thesis was discussed in detail. Using the case of COMSOL Multiphysics, a simulation tool used in this thesis, we discussed the main factors affecting the simulation results in a FEM photonic model and revealed the importance of the boundary conditions, source, and mesh in photonic simulation using the finite element method.

In the following chapter, a photonic simulation model based on graphene and silicon carbide is built-in COMSOL Multiphysics to investigate the surface polariton modes excitation in a flat graphene/SiC/Si material system.

Chapter 5. Investigating surface polariton modes in flat graphene on cubic silicon carbide on silicon system

5.1. Introduction

Building a FEM model in the COMSOL Multiphysics model involves several steps and requires much care, such as determining the accurate mesh, appropriate boundary conditions, the source to excite the model, and materials for the different model's components. In addition, for instance, some components of the model may require special mesh refinement than others. Thus, before building a very complex simulation model, it is always advised that one should first create a simple structure and develop from it to form a more complex model.

Consequently, in this chapter, we performed the mesh benchmarking using a simple FEM simulation model to test the convergence and accuracy of the simulation results. We first built a simple silicon carbide on a silicon model, which we used to compare the numerically simulated spectral reflectance with analytical ones calculated using Matlab to validate our simulation model's accuracy. After confirming the optimal parameters/ mesh requirement for the best accurate simulations results, we subsequently build from that to the more complex silicon carbide model and graphene/SiC models to investigate surface polariton modes excitation in these materials. Analytical calculations were performed using the Fresnel reflection coefficient in Matlab, while the numerical/FEM simulations were conducted using COMSOL Multiphysics 5.5.

5.1.1. Analytical modelling - Fresnel coefficients

When an electromagnetic wave "light" interacts with an interface separating two mediums with refractive index n_1 and n_2, two phenomena, reflection, and refraction occur. The Fresnel equations can describe the fraction of reflected and transmitted waves to the incident wave and their phase shifts[248]. The Fresnel equations assume a flat interface between the two homogeneous and isotropic media[248]. Therefore, these equations offer the opportunity to resolve the EM wave problem of different polarisation, s, and p polarisations. The p -polarisation refers to the situation where the electric field part of the EM wave is in the plane of incidence while the magnetic field component of the EM wave is normal to the plane of incidence. On the other hand, s -polarisation corresponds to when the electric field part of the wave is normal to the plane of incidence while the magnetic component is in the incidence plane. Electromagnetic field polarisation was discussed in chapter 2, section 2.3, and elsewhere[44, 248]. By considering a plane wave incident at the interface between two mediums with refractive index n_1 and n_2 as one shown in Figure 5.1, the Fresnel equations enable the calculation of reflection (R) and transmission (T) at the various incidence and polarisation angles[248].

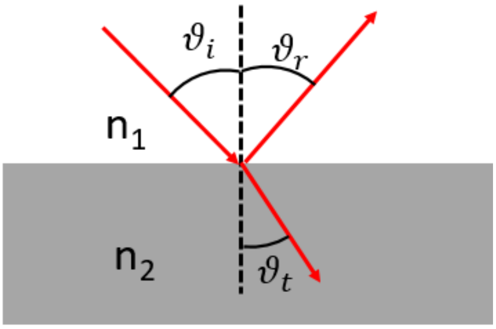

Figure 5.1. A schematic showing a plane wave incident with an oblique incidence angle (θ_i) at the interface between the two mediums of refractive index n_1 and n_2 undergoing reflection and transmission processes. θ_r depicts the angle of the reflected wave.

$$R_s = \left|\frac{n_1(\omega)\cos\vartheta_i - n_2(\omega)\cos\vartheta_t}{n_1(\omega)\cos\vartheta_i + n_2(\omega)\cos\vartheta_t}\right|^2 = \left|\frac{n_1(\omega)\cos\vartheta_i - n_{2(\omega)}\sqrt{1-\left(\frac{n_{1(\omega)}}{n_2(\omega)}\sin\vartheta_i\right)^2}}{n_1(\omega)\cos\vartheta_i + n_2(\omega)\sqrt{1-\left(\frac{n_1(\omega)}{n_2(\omega)}\sin\vartheta_i\right)^2}}\right|^2 \tag{5.1}$$

$$R_p = \left|\frac{n_2(\omega)\cos\vartheta_i - n_1(\omega)\cos\vartheta_t}{n_2(\omega)\cos\vartheta_i + n_1(\omega)\cos\vartheta_t}\right|^2 = \left|\frac{n_2(\omega)\cos\vartheta_i - n_1(\omega)\sqrt{1-\left(\frac{n_1(\omega)}{n_2(\omega)}\sin\vartheta_i\right)^2}}{n_2(\omega)\cos\vartheta_i + n_1(\omega)\sqrt{1-\left(\frac{n_1(\omega)}{n_2(\omega)}\sin\vartheta_i\right)^2}}\right|^2 \tag{5.2}$$

where ϑ_i and ϑ_t describe incidence and transmission angle

Similarly, the transmission coefficients for both s and p polarization can be calculated as follows;

$$T_s = \left|\frac{2n_2(\omega)\cos\vartheta_i}{n_1(\omega)\cos\vartheta_i + n_2(\omega)\cos\vartheta_t}\right|^2 \tag{5.3}$$

$$T_p = \left|\frac{2n_1(\omega)\cos\vartheta_i}{n_2(\omega)\cos\vartheta_i + n_1(\omega)\cos\vartheta_t}\right|^2 \tag{5.4}$$

Considering a multilayer structure comprises of air/epilayer and epilayer/substrate interfaces excited with a near-normal incidence, the Fresnel reflection coefficient can be simplified as follow;

$$r_{ij} = \frac{n_i(\omega) - n_j(\omega)}{n_i(\omega) + n_j(\omega)} \tag{5.5}$$

where indices i and j represent different regions/mediums in the model.

Subsequently, the total reflectance coefficients of such a multilayer system can be calculated using the following Cadman and Sadowski's expression[282];

$$r_T = \frac{r_{12} + r_{23}\exp(2i\beta)}{1 + r_{12}r_{23}\exp(2i\beta)} \tag{5.6}$$

where r_{12} and r_{23} represent the Fresnel reflection coefficient at air/epilayer and epilayer/substrate interfaces.

$\beta = 2\pi d\omega\sqrt{\varepsilon_2(\omega)}$, defines the phase difference, which depends on the thickness (d) and dielectric permittivity of the epilayer. The reflectance of the system can therefore be calculated using equation (5.7),

$$R = |r_T|^2 \tag{5.7}$$

We use expressions (5.6) and(5.7) for a benchmarking analysis performed in the next section, where the analytical calculation results from (5.7) are compared to the numerically simulated results in COMSOL Multiphysics to test the convergence of the simulation model.

5.2. Silicon carbide on silicon model for mesh benchmarking

In this section, we build a simple air/silicon carbide/silicon model in COMSOL Multiphysics, and the simulated reflectance is compared to the analytically calculated reflectance obtained using equations (5.6) and (5.7). Figure 5.2a shows the schematic of the silicon carbide on silicon considered in our calculation. The model consists of an airbox, silicon carbide film (C=2 μm thick), and silicon (S=3 μm thick). The structure is considered to be infinitely large, and thus, periodic boundary conditions were employed on the side of the model (the simulation window of W=2 μm). We used the boundary source/port to excite the model. The model was excited with a plane EM wave at normal incidence (θi=0). The reflectance (R) was calculated from the s- parameters S_{11} ($R = |S_{11}|^2$).

The frequency-dependent dielectric function of SiC was modelled using a Lorentz oscillator/TOLO formalism (2.71), and it is also reported in Figure 4.11 along with the material input parameters for 3C-SiC. Silicon was simulated as a nondispersive medium with a refractive index of 3.42. Figure 5.2b shows analytical reflectance and the simulated reflectance at different maximum mesh element sizes.

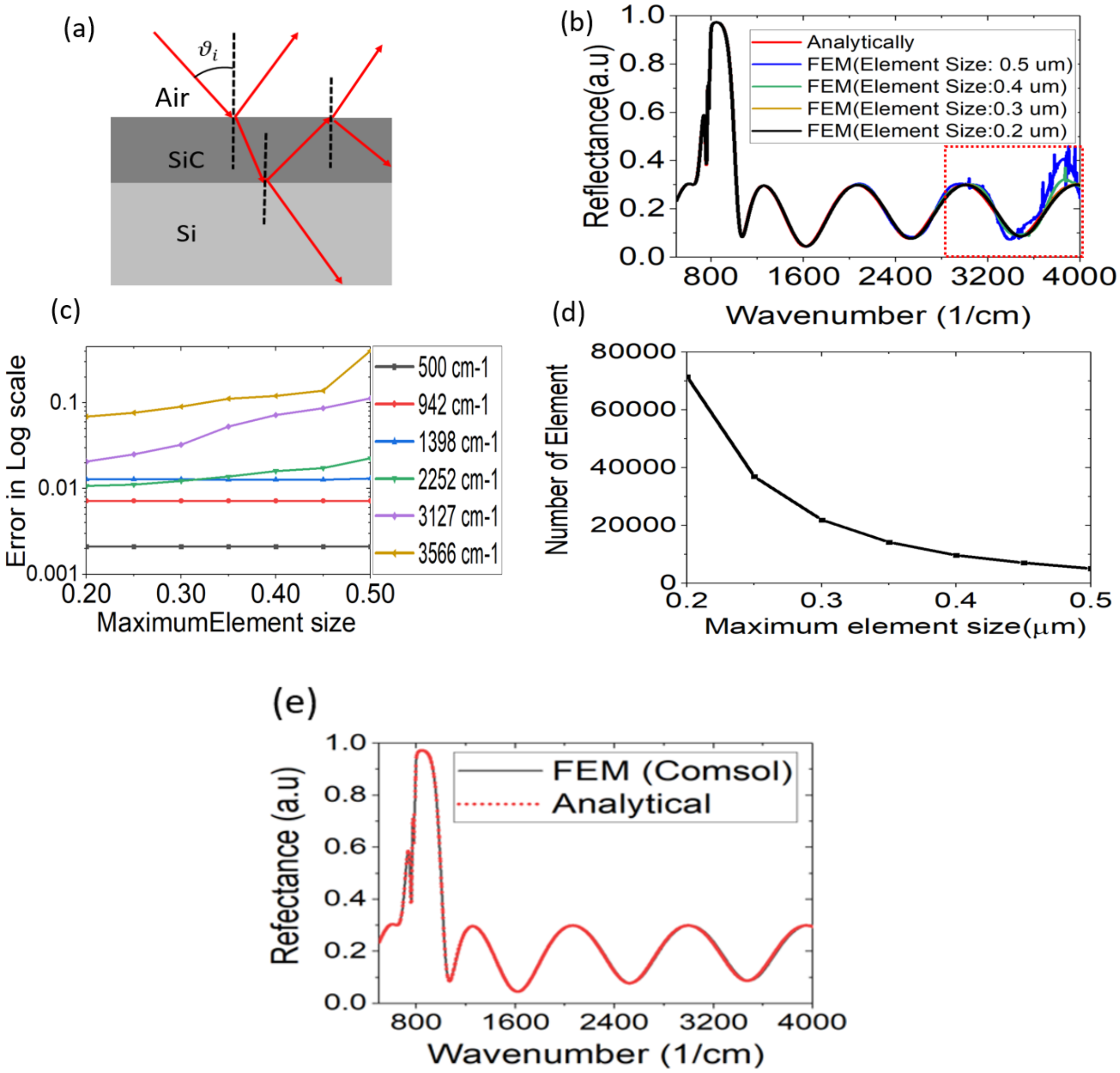

Figure 5.2. (a) The schematic of the SiC/Si model for mesh benchmarking, (b) Simulated reflectance at different maximum mesh element sizes when compared with the analytically calculated reflectance of SiC/Si model, highlighted in red, is the spectral range where the large element size (coarse meshes) failed to resolve the model and yield to noise results, (c) the calculated absolute error with respect to the maximum element showing a good match between simulated results and the analytical one when the maximum element size is small ~0.2μm, (d) The total number of elements with respect to the maximum element size revealing that large computer memory is required for smaller element size, (e)

a comparison of analytical results with numerical /FEM results simulated using COMSOL Multiphysics with a maximum element size of 0.2 μm.

The simulated reflection spectral reveals the noise (highlighted with red box) in the high-frequency range, suggesting a finer mesh requirement for better simulation results at that spectra range. Taking analytically calculated reflectance obtained with equation (5.7) as a reference result, we calculated relative error for different element sizes in the simulation model;

$$\text{Relative Error} = \left|\frac{\text{Analytical results} - \text{FEM Simulation results}}{\text{Analytical results}}\right| \tag{5.9}$$

The calculated relative errors at different maximum mesh element sizes are shown in Figure 5.2c. From Figure 5.2c, one can observe that the smaller the maximum element size is, the closer the simulated results are to the analytical one.

In the simulated structure, a thinner element size of ~ 0.2 μm displays the most accurate results. Though the smaller element size converges to the most accurate results, the structure is divided into more elements (Figure 5.2d), leading to large computation memory and time required to complete the simulation. In Figure 5.2e, the simulated reflectance results using a maximum element size of 0.2 μm are reported. The analytically calculated reflectance shows a better fit between the two methods, FEM and analytical reflectance, when a smaller maximum mesh element size of 0.2 μm is used to mesh the model corresponding to 1/10 of the thickness of SiC in the model.

The simulated FEM model matches analytical results for the simple two-layer structure investigated in this section. Therefore, we extend our FEM model to a complex structure in the following sections by adding diamond and graphene to investigate surface polariton mode excitation in these materials.

5.3. A simulation model for analysis of surface phonon polariton excitation in silicon carbide on silicon

As hitherto discussed, silicon carbide supports surface phonon polariton(SPhP) mode within the spectral region known as the Reststrahlen band[82, 83], which is bound between LO and TO frequencies [84]. Thus, this section investigates SPhP modes excitation in cubic silicon carbide film (3C-SiC/Si). It was shown in Figure 2.11 that SPhP modes are characterised by a large k- vector than the incident plane wave (photon) of the same frequency. Therefore, to couple incident photons into surface polariton mode, their momentum needs to be matched. The incident photon needs to be manipulated using a prism coupler, diffraction gratings, or scanning near field optical microscope to match its wavevector to the k- vector of surface plasmon/phonon modes[44, 46]. Here we used the prism coupler to excite SPhP in SiC/Si model.

Two configurations for prism coupling, Otto with air coupling gap[57] and Kretschmann without air gap[53], are typically employed to excite SPP and SPhP modes in a planar interface (see this in section 2.5.1 of chapter 2).

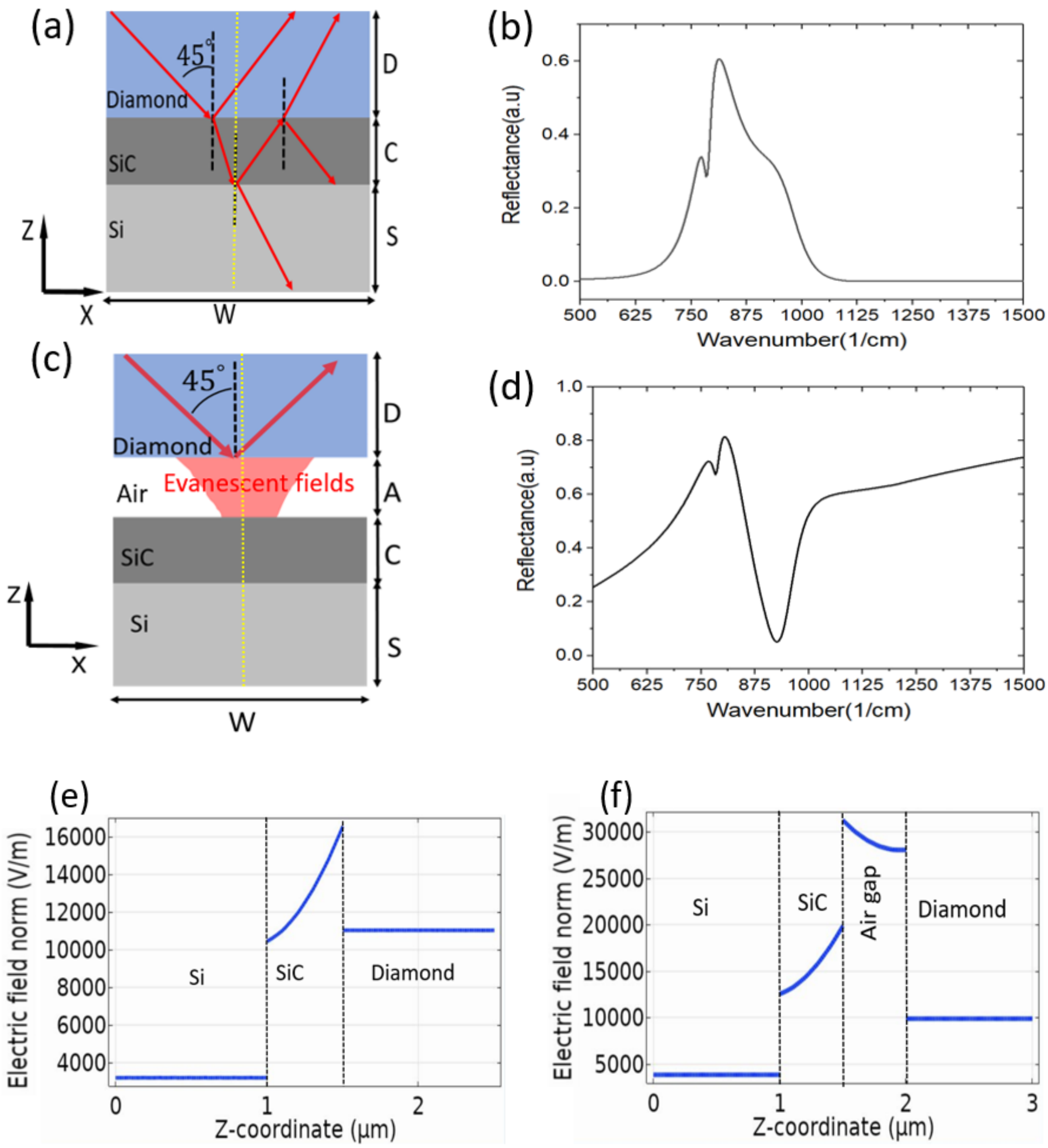

Figure 5.3. The simulation results for investigation of surface phonon polariton excitation in the SiC/Si model. (a) schematic of the bare SiC/Si simulation model using Kretschmann prism configuration (b)the simulated reflectance of SiC/Si model when Kretschmann prism configuration is used (no excitation

of SPhP mode in SiC). (c) a schematic of the bare SiC/Si simulation model using Otto prism configuration. A yellow vertical dash line in a and c shows a cutline along which the electric field was calculated. (d) The simulated reflectance of SiC/Si model when Otto prism configuration is used (showing SPhP mode excitation in SiC). (e) the calculated E-field along a cutline in the bare SiC/Si model using Kretschmann prism configuration shows the absence of evanescent field in Si to match SPhP's field nature, which hinders coupling between incident photon and surface phonon in SiC. (f) Using Otto prism configuration, the calculated E-field along a cutline in the SiC/Si model shows the evanescent field generation in air and facilitates the SPhP excitation in the air –SiC interface.

To investigate SPhP mode excitation in the 3C-SiC model, we built a FEM simulation model using Kretschmann and Otto configurations. The diamond prism with a refractive index of 2.42 was employed. This is because a diamond crystal was used for our IR characterisation in our experimental samples using the attenuated total reflection- FTIR (ATR-FTIR) system. Figure 5.3 shows the schematics of the model and simulation results for SPhP mode analysis in the SiC/Si system. As shown in Figure 5.3.a, we first used the Kretschmann configuration with the diamond in direct contact with SiC. The simulated reflectance revealed only one dip in reflectance at 797 cm^{-1}, which is a TO bulk SiC phonon mode (Figure 5.3b). This indicates that with the Kretchman prism coupling, we cannot match the momentum of an incident photon to that of SPhP in SiC for surface phonon polariton excitation in this flat SiC / Si system. Generally, this is possible if we can meet the condition of total internal reflection at the prism (high index media) and the dielectric spacer (lower refractive index media), leading to evanescent fields generation, which couple with surface phonon for SPhP mode excitation. It is shown in Figure 5.3c that after adding an air gap between diamond and SiC and exciting the model with a TM/p-polarised wave at 45° of incidence, the evanescent field was generated. This leads to the coupling of surface phonon in SiC with the evanescent field at the air- SiC interface, and hence excitation of SPhP mode happens at the resonance frequency of ~948 cm^{-1}, corresponding to a sharp dip in the reflectance spectra (Figure 5.3d).

Furthermore, we analysed the cutline field (electric field intensities calculated along the yellow dash line in Figure 5.3a and c) for SiC/Si model at the resonance frequency of 948 cm^{-1}. From Figure 5.3e, for the Kretschmann configuration, the coupling to SPhP is supposed to occur at the SiC-Si interface; however, the fields in Si are not evanescent and fall considerably in this medium due to the large refractive index of Si of 3.42. Therefore there is no excitation of SPhP mode. On the other hand, when we integrated an air gap between diamond and SiC, Otto configuration (Figure 5.3c), the calculated E-fields along the cutline in the z-coordinate show maximum E fields at the air–SiC interface. Then the fields evanescently decay inside SiC and air, respectively (see Figure 5.3f). Such a presence of an evanescent field enables the coupling between incident photon and surface phonon in SiC, leading to excitation of SPhP mode at 948 cm^{-1}.

5.3.1. Effect of air gap thickness on the resonance excitation of surface phonon polariton resonance in silicon carbide

The thickness of a dielectric space/ coupling medium, the refractive index of both the spacer and prism, polarisation and the angle of incident radiation are the three critical factors affecting the strength of surface polariton mode excited using Otto's configuration. This section analysed the effect of air gap thickness on the resonance excitation of SPhP in our SiC/Si model. The air gap thickness in Figure 5.4a was increased from 0 µm (i.e., without air gap) to 1.5 µm.

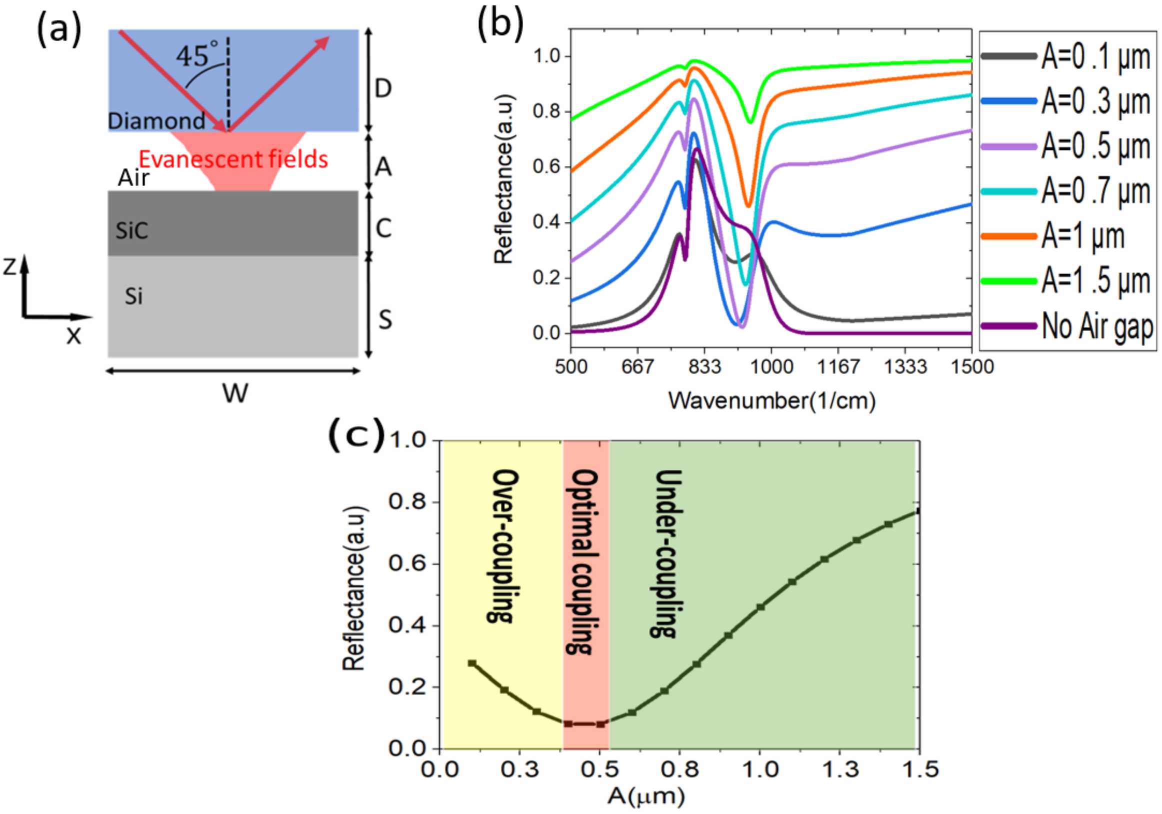

Figure 5.4. The effect of air-gap thickness on the surface phonon polariton excitation in SiC/Si model (b) simulated reflectance for different air-gap thickness, (c) calculated reflectance at 948 cm^{-1} as a function of air gap thicknesses revealed three ranges of coupling between incident light and surface phonon.

The simulated reflectance at various air gap thicknesses is reported in Figure 5.4b. It is shown in Figure 5.4b that when A=0 µm, there is no excitation of SPhP, as discussed in the previous section. However, for A > 0, SPhP mode can be excited with varying reflectance intensities (different dips in reflectance spectra). This condition holds for all air gap thicknesses comparable to the penetration depth (d_p) of the evanescent field in the coupling spacer. The penetration can be calculated as follows:

$$d_p = \frac{\lambda}{2\pi n_d \sqrt{\sin^2\theta - \left(\frac{n_d}{n_s}\right)^2}} \tag{5.10}$$

where λ and θ describe the wavelength and angle of incidence light at the diamond and coupling spacer(air) interface, n_d and n_s represent the refractive index of the prism (n_d) and the spacer (n_s), respectively. The calculated penetration depth at 45° and 948 cm^{-1} for a diamond-air interface is ~ 1.3 μm.

Three distinct coupling ranges occur for different thicknesses of the coupling medium. That is, under-coupling, optimal-coupling, and over–coupling[283]. For the diamond/air/SiC/Si model, optimal coupling corresponds to the A~ 0.5 μm, while under and over- coupling ranges correspond to thicker and thinner than 0.5 μm, respectively (Figure 5.4c).

5.3.2. Effect of the polarisation and incident angle of electromagnetic wave on the resonant excitation of surface phonon polariton

As discussed in chapter 2, excitation of surface modes on a planar interface requires an incident EM radiation to be a TM/ p- polarised source. This means that the magnetic component of EM fields is purely transverse to the direction of propagation (k- vector). Consequently, we investigated the effect of different polarisation of incidence waves on the resonance excitation of SPhP mode in the SiC/Si model (Figure 5.5a). In Figure 5.5b, the simulated reflectance results for TE (an electric component of the fields is purely transverse to the direction of propagation) and TM polarisation are provided. As expected, when incident radiation is TE wave, there is no excitation of SPhP modes for the SiC/Si model. This is because the surface phonon at the air-SiC planar interface has an electric field component perpendicular to the interface and vanishing evanescently in both mediums and a parallel component of the field along the direction of propagation. When the model is then excited by the TE source, there is no perpendicular component of the E field; only a parallel component of the E field is present, and it is not along the direction of propagation, preventing SPhP mode excitation.

On the other hand, when we excite the model with a TM polarisation, we have a perpendicular component of E field and a parallel component along the direction of propagation matching with that of surface phonon in SiC. Hence this leads to the excitation of SPhP mode at the air-SiC planar interface at the resonance frequency of 948 cm^{-1}. It is worth noting that the resonance excitation of SPhP mode occurs at a particular incident angle called ‘surface polariton resonance angle[50]. The resonance angle of the surface polariton model can be calculated using equation (2.51) as described in chapter 2, section 2.5.

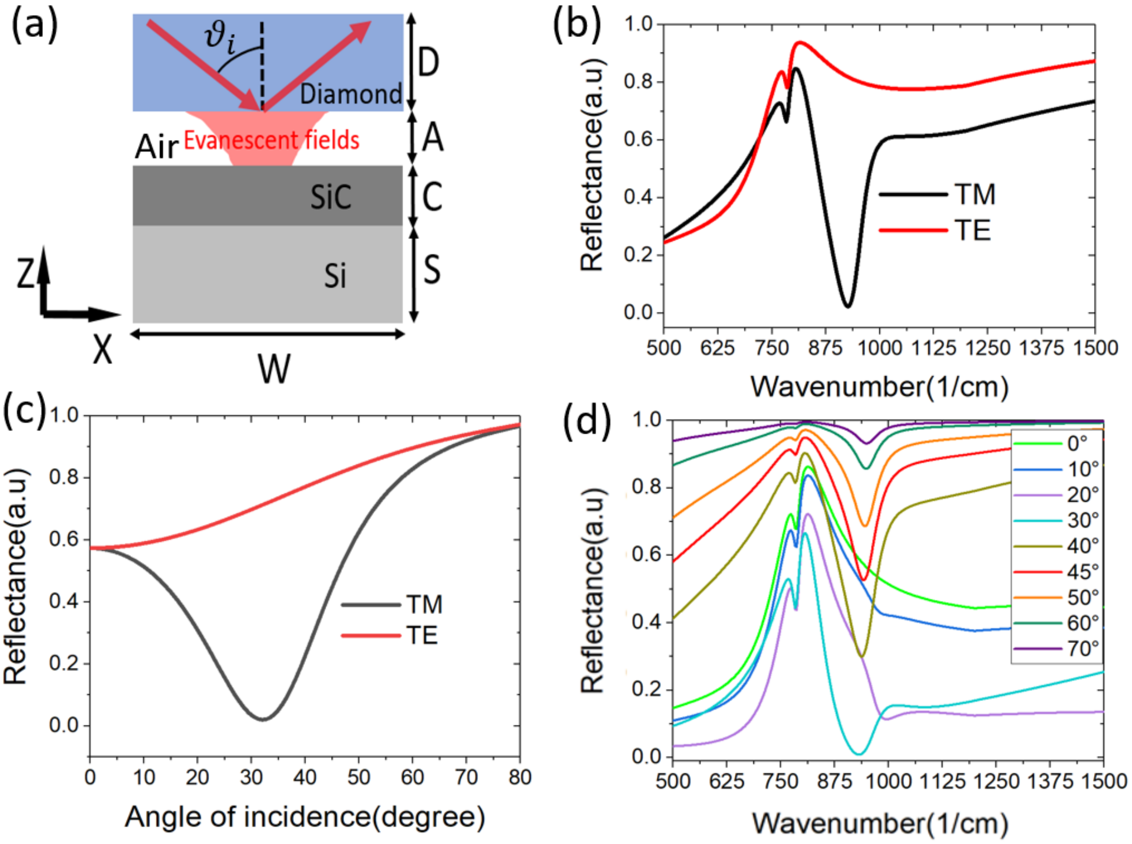

Figure 5.5. Polarisation and incident angle dependency on SPhP mode excitation in SiC/Si model. (a) a schematic of the simulated SiC/Si model (excited with TM wave). (b) Simulated spectra reflectance for TM and TE polarised EM source. (c) Simulated angular dependent reflectance at different polarisation TM and TE showing the resonance excitation of SPhP at the resonance angle of θ_R~32°, and (d) spectral reflectance at different incident angles when the source is TM polarised.

To analyse the resonance angle for SPhP mode excitation in SiC/Si model, we performed the simulation at the varying incident angles (θi) of the EM wave for TE and TM polarisation at a fixed frequency of 948 cm^{-1}. It can be observed in Figure 5.5c that the lowest dip (~0) in the reflectance was realised at the resonant angle θ_R~32° when the model was excited by a TM source. This coincides with the analytically calculated θ_R of ~30° obtained using (2.51) for diamond/Air/SiC/Si system.

Lastly, we investigated the spectral reflectance of the SiC/Si model under different incident angles, as shown in Figure 5.5d. To excite surface polariton at the planar interface between a conductor and a dielectric, one needs to excite the model with an incident angle larger than the critical angle ($\theta i > \theta c$). In the diamond/air/SiC/Si system, the critical angle at the diamond air interface is θ_c~24°. As shown in Figure 4.5d, for incident angles below 20°, there is no dip in the reflectance. However, as the angle of incident radiation starts approaching the critical angle (24°), the evanescent field is generated; hence the SPhP mode is excited. Moreover, the sharp dip in reflectances is realised at the incident angles closer to the resonant angle (θ_R~32°) and begins to decrease for higher incident angles.

5.4. Exploring the excitation of surface plasmon polariton in epitaxial graphene on silicon carbide on Silicon

5.4.1. Validity of graphene FEM model - A comparison of graphene's simulation in COMSOL Multiphysics with a graphene reference transfer matrix method model

Accurately simulating graphene in this thesis is vital since graphene is the main material in this study. Hence, in this section, we tested our COMSOL Multiphysics model by comparing our results to the transfer matrix method model from the literature. The reference model is a multilayer structure containing graphene embedded between the dielectric materials(Figure 5.6a) and exhibiting surface plasmon resonance[284]. Figure 5.6b shows the simulated surface plasmon resonance modes, which were calculated at a fixed central frequency of 1THz using the transfer matrix method[284]. We used our COMSOL Multiphysics model, where graphene was simulated as a transition boundary, to compare to the reference model (Figure 5.6a). Figures 5.5c and 5.5d show the simulated results with our COMSOL Multiphysics model, with and without graphene in the model, respectively.

As shown in Figure 5.6c, the simulated results without graphene reveal a ~100% flat reflectance for the simulated structure for all incident angles above 15°. However, after adding graphene using COMSOL's TBC (see Figure 5.6a), we realised three surface plasmon polaritons resonances indicated by the sharp dip in the reflectance of the structure. The simulated results in our COMSOL model agree well with the reference results calculated using the transfer matrix method[284].

This implies that graphene can be accurately simulated with TBC in our COMSOL Multiphysics model. Hence in the next section, we build a COMSOL Multiphysics model based on our epitaxial graphene on silicon carbide material system to investigate the excitation of surface plasmon polariton in EG.

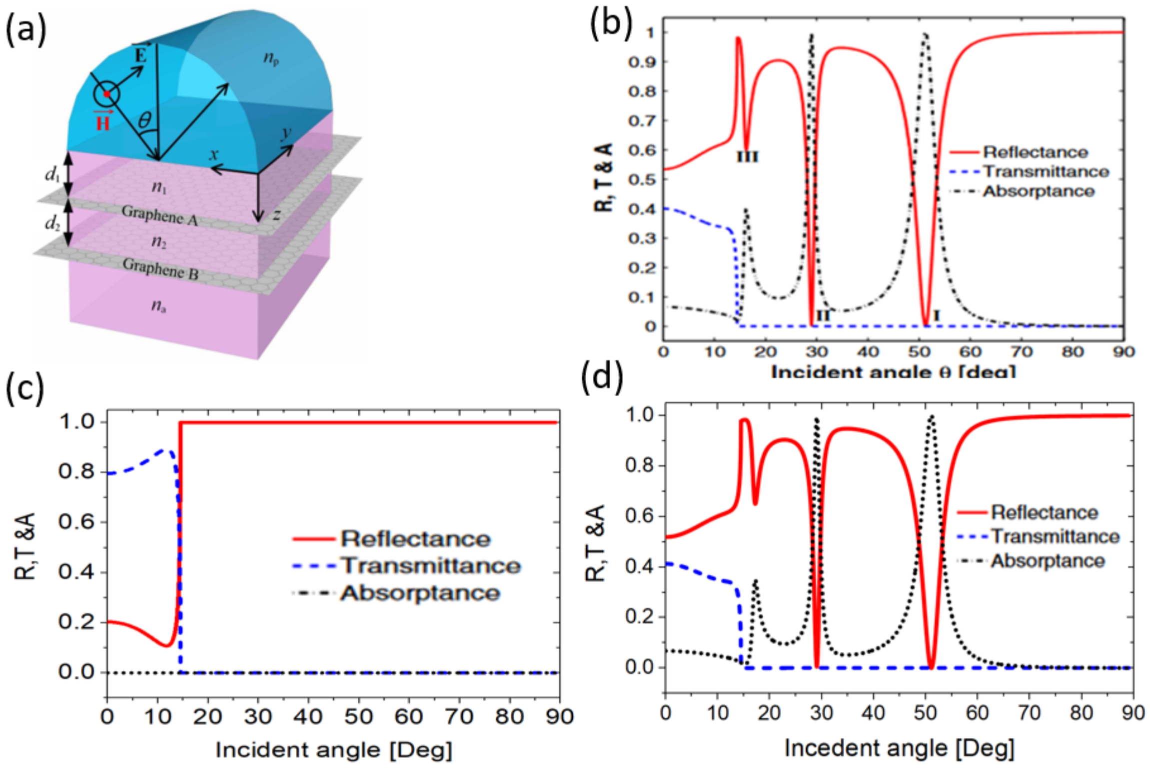

Figure 5.6. (a) A schematic of the reproduced graphene stratified slab model embedded between prism ad semi-infinite dielectric layer(Otto prism configuration excited by TM-wave incidence) as reported in [284]. (b)The simulated angular dependent absorbance, transmittance, and reflectance at 1 THz using the transfer matrix method. (c) The calculated angular dependent absorbance, transmittance, and reflectance at 1 THz using our model in COMSOL multiphysics, without graphene, and (d) the calculated angular dependent absorbance, transmittance, and reflectance at 1 THz using our COMSOL Multiphysics model with graphene (simulated as TBC) embedded between the dielectric mediums (n_1=1.8, n_2=1.4, n_a=1, and germanium prism with n_p=4).

5.4.2. Analysing the excitation of surface plasmon polariton in graphene on silicon carbide at the planar interface

To investigate the graphene plasmon polariton response in EG/3C-SiC/Si material system, we added a graphene layer in our SiC/Si model. Figure 5.7b describes the simulated reflectance with graphene and without graphene in the model.

It is noticeable from the inset of Figure 5.7b that the presence of graphene on SiC has a slightly noticeable effect on the reflectance of the bare SiC/Si model. It is believed that surface plasmon polariton in graphene and phonon polariton in SiC would have different polariton resonance angles, implying that EG/SiC system would have a different resonance angle to SiC/Si system. Thus we performed the reflectance simulations of the graphene/SiC/Si model at different incident angles, which revealed a similar resonance angle of 32° to the one obtained in the bare SiC/Si model for SPhP resonance angle (Figure 5.7c). This indicates that we are unable to excite the propagating SPP mode in the graphene on SiC with a flat interface. The reason is that graphene plasmon has a larger k-vector than incident EM radiation, which hinders their coupling for graphene SPP mode excitation.

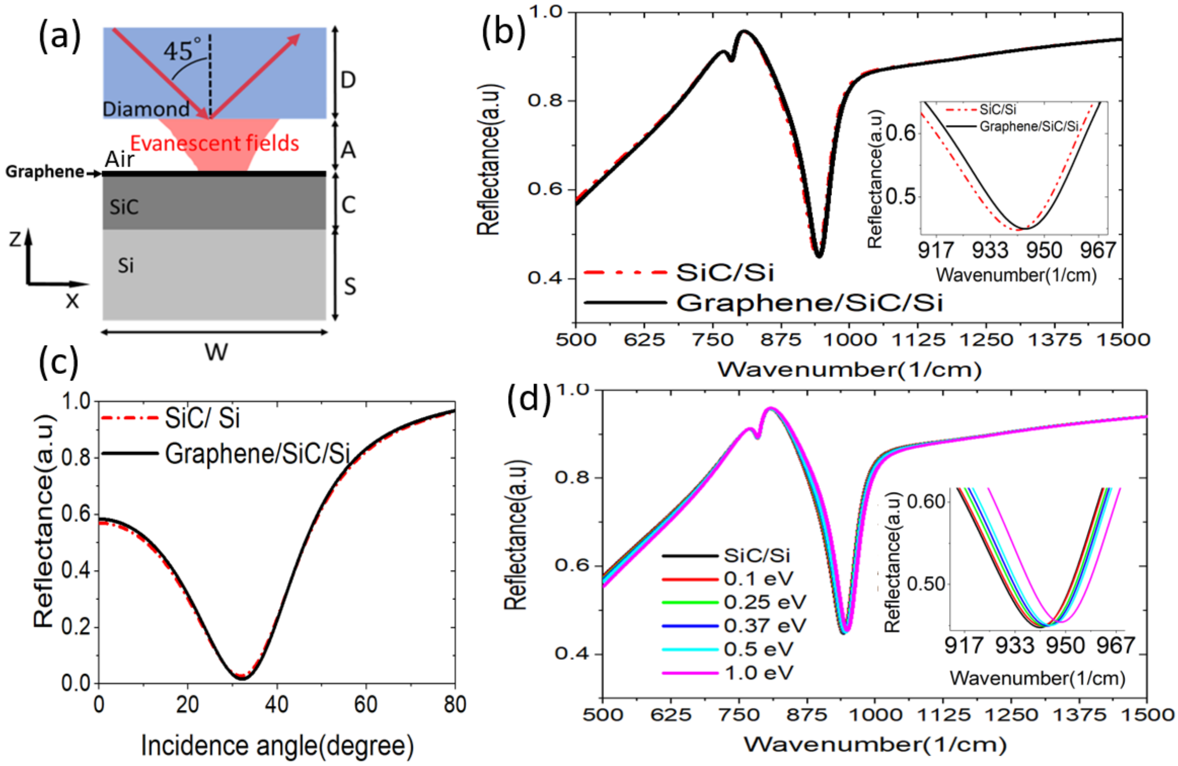

Figure 5.7. Investigation of surface plasmon polariton excitation in graphene/SiC/Si model. (a) schematic of the simulated model. (b) Simulated spectral reflectance of bare SiC/Si and graphene/SiC/Si model(inset shows slight blue shift for the SPhP mode when graphene is added to the SiC/Si model). (c) Angular dependent reflectance of bare SiC/Si and graphene/SiC/Si model(adding graphene on SiC/Si shows no noticeable impact on the SPhP resonance angle of the system). (d) Simulated reflectance at different graphene Fermi energy(E_F) showing a slight blue shift of the mode when E_F is increased to high values.

Furthermore, we performed the simulation with different Fermi energy in graphene. This was performed to analyse if graphene can tune the resonance frequency of the graphene plasmon polariton modes and enable us to analyse them. As shown in the inset of Figure 5.7d, by increasing the E_F from 0.1 eV to 1 eV, a slight blue shift of the mode at the surface phonon polariton resonance can be noticed. This suggests that we need to investigate a different model where graphene is on a patterned SiC to excite graphene plasmon polariton. This will be addressed in chapter 6.

5.5. Experimental characterisation of surface polariton in epitaxial graphene on silicon carbide at the planar interface

Lastly, we conducted experiments and infrared characterisation on the bare SiC/Si(100) and EG/3C-SiC/Si(100) samples to confirm the simulation results. First, the epitaxial graphene on cubic silicon carbide on silicon (EG/3C-SiC/Si) was grown using a catalytic graphitisation process[33, 34] as described in section 4.1.1 of chapter 4 (see Figure 4.1). Second, we performed Raman spectroscopy analysis of the EG/3C-SiC/Si sample using a WITEC confocal Raman microscope excited by 532nm (argon-ion) laser with 100 × objective with a spot size of ~300 nm (see section 4.1.3). Figure 5.8a depicts Raman spectra measured on EG/3C-SiC/Si (100). The reported spectrum is an average collected over 10 μm × 10 μm area on the sample with 0.2 μm step size and 0.1-second integration time. The Raman characteristics of the sample revealed the ratio of I_D/I_G and LO/2D of 0.25 and 0.24, respectively, which is in line with the Raman characteristics of the best EG produced in our catalytic graphitisation process[33-35].

Infrared characterisation of bare and EG/3C-SiC/Si samples using FTIR-ATR is shown in Figure 5.8b. As expected, the measured reflectance showed three reflectance dips at 610 cm^{-1}, 797 cm^{-1}, and 940cm^{-1}. The dip at ~610 cm^{-1} is a bulk silicon mode and was not considered in our numerical simulations. The second dip at 797 cm^{-1} is a bulk SiC mode, corresponding to the transverse optical phonon (TO). At ~940 cm-1, the dip occurs within the SiC'S Reststrahlend spectral band, where SiC has the surface phonon polariton mode.

Thus, the reflectance measured on the EG/3C-SiC/Si sample, in agreement with simulation, did not reveal a very pronounced effect of graphene compared to the measured reflectance on the bare 3C-SiC/Si except for the noticed weak reflection dip at ~1060 cm-1 which is a consequence of epoxy-functional groups such as silicon oxycarbide (SiOC) present in the graphitised 3C-SiC/Si samples[35, 285]. After our catalytic graphitisation process, these epoxy functional groups appear on our samples and have their vibrational resonances around this spectra frequency[35]. They were not considered in our numerical simulations.

The fact that the reflectance measured on the EG/3C-SiC/Si failed to reveal a pronounced difference compared to the bare 3C-SiC/Si reflectance confirms the momentum mismatch between incident photon and surface plasmon in EG/SiC/Si system, which could be overcome by growing graphene on the structured (no flat) SiC substrate.

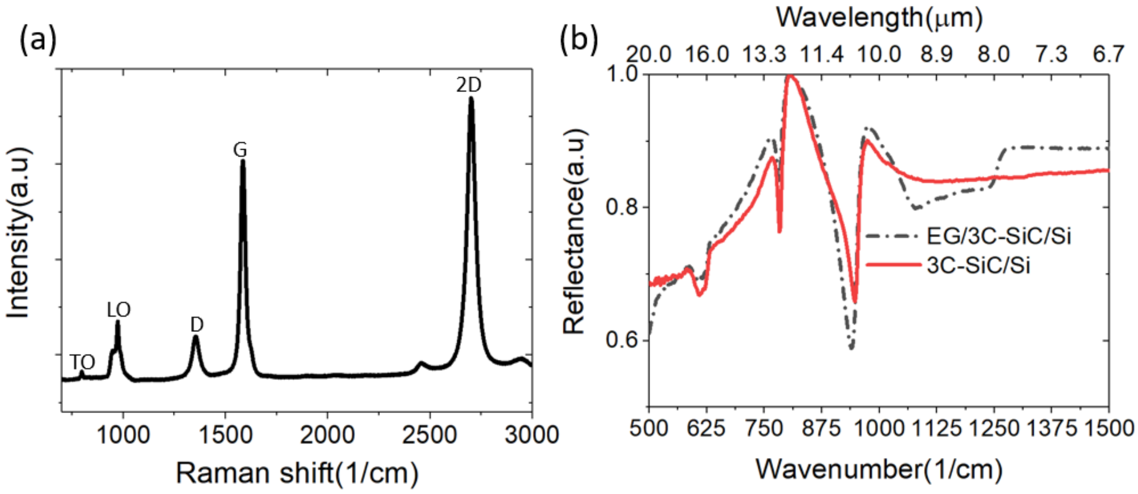

Figure 5.8. The experimental characterisation for surface phonon excitation in EG/3C-SiC/Si. (a) Raman characterisation of EG/3C-SiC/Si(100), (b) FTIR-ATR characterisation of bare 3C-SiC/Si and EG/3C-SiC/Si revealing the surface phonon polariton response at 940 cm^{-1} for both the bare SiC and EG/3C-SiC on silicon.

5.6. Summary

In this chapter, a flat finite element method simulation model based on epitaxial graphene on silicon carbide on silicon was created and characterised using COMSOL Multiphysics to investigate surface phonon and surface plasmon polariton excitation in these materials systems. First, simple bare silicon carbide on silicon model excited with a plane wave was proposed and validated by comparing the analytical results with the simulation results at different mesh sizes in the COMSOL model to confirm the accuracy of our simulations. Second, we investigated the surface phonon polariton excitation in a bare silicon carbide model. It was realised that Otto prism coupling configuration with an air gap of thickness comparable to the penetration depth is required for excitation of SPhP polariton in a SiC/Si system with a flat interface. We further demonstrated the dependency of SPhP resonances excitation on the polarisation and angle of incident radiation with a TM/p- polarisation and incident angle of 32° required for resonant excitation of SPhP modes in our SiC/Si model. We integrated graphene into SiC/Si FEM model to investigate graphene’s surface plasmon polariton excitation in epitaxial graphene on silicon carbide on silicon (EG/SiC/Si) system. Our simulation results revealed that graphene had a negligible effect on the reflectance of the model and that silicon carbide SPhP’s response dominated the simulated results. Lastly, we conducted experiments and infrared measurements to investigate further the surface polariton responses in EG/3C-SiC/Si material system. IR characterisation of the bare 3C-SiC/Si and EG/3C-SiC/Si samples confirmed the simulation results where only SiC surface phonon polariton response was realised and indicated by the dip in the reflectance at ~ 940 cm^{-1}. It is believed that graphene SPP modes can be excited if graphene is grown on the patterned silicon carbide substrate, where the structures can provide a missing momentum to the incident photon to match the momentum of graphene's surface plasmon. Thus, in the following chapter, we investigate surface plasmon, surface phonon excitation, and their hybridisation in graphene-coated silicon carbide cylindrical nanowires.

Chapter 6. Hybrid surface phonon-plasmon polariton in graphene-coated silicon carbide nanowires for mid-infrared nanophotonics

6.1. Introduction

Over the recent years, researchers have been investigating surface plasmon polariton in curved graphene sheets such as carbon nanotubes (hollow cylinders rolled up from graphene sheets) [286-291]. For example, Hartmann et al. studied the launching of propagating SPP modes in carbon nanotube dipolar emitter[292]. They showed that the semiconducting single-walled carbon nanotubes act as directional near-infrared point dipole sources to excite propagating surface plasmons along the nanotube axis. Subsequently, Chiu et al. revealed strong and broadly tunable plasmon resonances in a thick film of aligned carbon nanotubes[293]. They indicated that the outstanding nanotube alignment enables 99% of attenuation to be linearly polarised along the nanotube axis.

On the other hand, adding a shell consisting of a different material onto a metal nanoparticle has been shown in some cases to enhance absorption and broaden the tunability range of the localised plasmon resonance by adjusting the shell's thickness. Several two-layered systems, such as metal nanoparticles with dielectric shell[294] or Si core with metal shell[295], were demonstrated for optical wavelengths. While metal-dielectric-metal[296, 297] or Si-dielectric-metal[298] configurations, which are of particular interest for biomedical applications[299], have been well-studied, fewer examples of three-layered multi-shell nanostructures have been reported. There is great interest in three-layered nanostructures as it has been generally shown that the addition of a dielectric spacer layer drastically changes the electric field distribution within the structures, opening the possibility for subwavelength confinement and enhancement of the field within the spacer[297, 298].

An analogy can be drawn between metal nanoparticles in the optical regime and SiC phonon polariton response within the Reststrahlen band at the MIR range. A few initial studies on SiC-graphene nanoparticles have been published[300, 301], but only limited theoretical research was conducted on curved multilayer metal-graphene[302, 303] or more general SiC-graphene nanostructures[304, 305]. Hence, further research is needed to investigate the MIR characteristics of core-shell SiC-graphene nanoparticles and nanowires, particularly now that a clear path exists to obtain such structures experimentally.

This chapter combines experiments and COMSOL Multiphysics simulations to investigate the localised surface phonon and plasmon polariton modes excitation and their hybridisation in EG-coated silicon carbide nanowires (3C-SiC NWs) system.

6.2. Theoretical characterisation of mid-infrared photon response in core/shell silicon carbide/graphene nanowires

6.2.1. Numerical simulation model

A schematic of the SiC/graphene core/shell nanowires is shown in Figure 6.1a. The model consists of SiC NW coated with graphene on Si substrate, including a silicon oxycarbide (SiOC) layer sandwiched between the graphene and the SiC core. Numerical simulations to investigate the MIR responses of the NWs were performed in COMSOL Multiphysics[269] using the finite element method (FEM). We modelled a single NW of a total 50 nm diameter, consisting of a SiC core diameter of 42 nm and an oxide shell thickness of 4 nm, replicated at a regular pitch of W=500 nm by applying periodic boundary conditions (PBC) in x and y coordinates. The pitch size was chosen to minimise cross-wire interactions.

The model utilises a TM/p polarised wave incident at $\vartheta_i = 45°$ into the diamond (D=100 nm) with a refractive index $n_d \approx 2.4$ in order to match the ATR-FTIR experimental conditions. An evanescent field with dominant vertical E_z component and negligible Ex or Ey components is excited in the air gap (A=120 nm) after total internal reflection from the air-diamond interface, which couples to the surface plasmon and phonon in graphene and SiC, respectively. Input frequency-dependent complex permittivity for graphene and silicon carbide are provided in section 4.3.4 of chapter 4. Silicon (S= 200 nm) was treated as a non-dispersive medium with a refractive index $n_s = 3.42$. The oxide layer between graphene and SiC NW is a silicon oxycarbide (SiOC) with a refractive index n=1.5[306]. Absorption A=1-R-T was calculated from reflectance R and transmittance T and is shown in Figure 6.1b.

We also built additional intermediate models for SiC NW/Si and graphene/SiC NW/Si with a total wire diameter of 50 nm in all cases (also graphene/air/Si in Appendix C, Figure C.1).

The simulated absorbance of a bare SiC NW (blue dotted line in Figure 6.1b) revealed two weak absorption peaks at 797 cm^{-1} and 940.5 cm^{-1}. The first corresponds to the SiC's bulk transverse optical (TO) phonon mode. The second peak, which appears within the SiC Reststrahlen window (shown in blue shading), is attributed to a Fröhlich/localised dipole surface phonon polariton (LSPhP) mode.

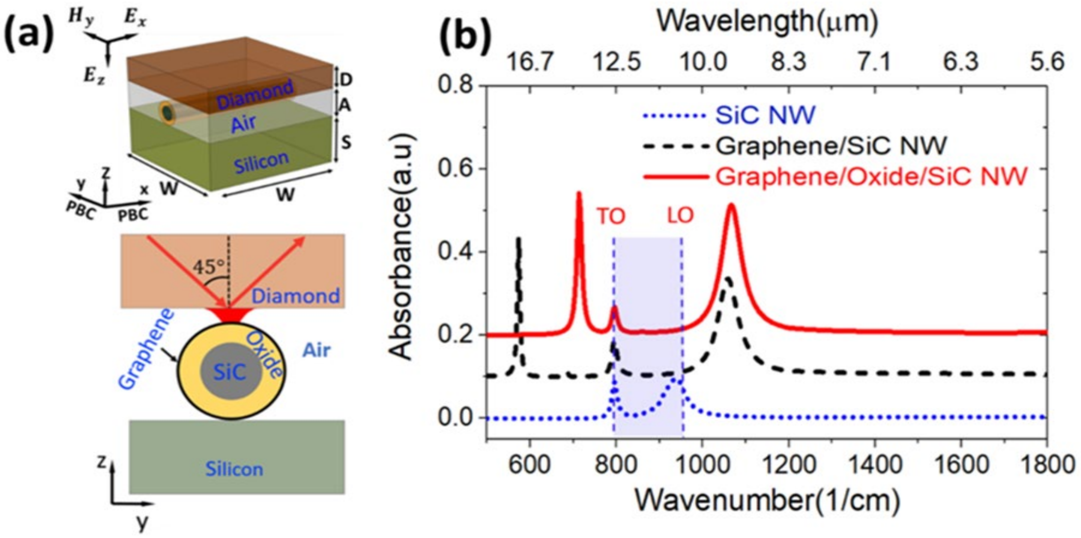

Figure 6.1. (a) Schematic of the graphene/oxide/SiC NW simulation model in 3D view (upper graph) and cross-section view (lower graph), (b) the simulated absorbance for SiC NW, Graphene/SiC NW, and Graphene/Oxide/SiC NW models. W=500 nm, S=200 nm, A=120 nm, D=100nm. The total diameter of NW is 50 nm consisting of the oxide shell thickness of 4 nm and SiC diameter of 42 nm.

The simulation conducted with graphene-coated SiC NW, without considering an oxide layer in between (black dashed line in Figure 6.1b), showed the splitting of the modes resulting in three absorption peaks: a sharp absorption at ~574 cm^{-1}, plus the SiC's bulk TO mode, and another broader peak at 1060 cm^{-1}. The splitting of the peaks results from the hybridisation of graphene's SPP mode with SiC localised dipole SPhP mode in a core-shell type configuration, resulting in localised phonon-plasmon coupled modes M1 and M2.

The simulated results on the graphene/oxide/SiC NW model (red solid line in Figure 6.1b) show three absorption peaks at 714 cm^{-1} (M1), 797 cm^{-1} (TO mode), and at 1067 cm^{-1} (M2). The presence of oxide also leads to a blueshift of the modes. There is a higher contrast between the permittivity of SiC and oxide at the lower frequency mode than at the higher frequency mode. The weaker absorption of the TO peak, a bulk mode, is expected due to the reduction in the total volume of the SiC core from 50 nm to 42 nm diameter in the model.

6.2.2. Modes and field analysis

Resonant frequencies of cylindrical nanostructures can be calculated as poles of electric polarisability derived from the electrostatic approximation of Lorenz-Mie theory[296, 307, 308]. The theory applies to both metallic and dielectric nanoparticles. Localised dipolar SPP and SPhP are considered due to the orientation of the incident evanescent vertical electric field perpendicular to the nanowires. While metal core-shell nanoparticles are represented with layers of finite thickness, graphene is usually treated as a conductive boundary due to its negligible thickness, which allows adding conductivity term to the polarisability expression rather than increasing the number of layers. For a two-layer SiC/graphene core-shell nanoparticle, the resonant frequencies can be determined by setting the denominator of electric polarizability to zero[304, 305]:

$$\alpha(\omega) = 4\pi R^3 \frac{\varepsilon_{SiC}(\omega) - \varepsilon_{air} + 2g(\omega)}{\varepsilon_{SiC}(\omega) + 2\varepsilon_{air} + 2g(\omega)} \tag{6.1}$$

$$g(\omega) = \frac{i\sigma(\omega)}{\varepsilon_0 \omega R} \tag{6.2}$$

where R is the total radius of the particle, ε_0 is the permittivity of free space, σ is graphene conductivity, ε_{SiC} and ε_{air} are permittivities of SiC and surrounding air correspondingly. SiC permittivity is frequency-dependent and can take positive and negative (metallic) values, so the resonance condition can be satisfied at multiple frequencies, representing hybridisation of graphene's shell SPP mode with SiC core SPhP mode and resulting in phonon-plasmon coupled modes M1 for lower frequency and M2 for higher frequency. The presence of a dielectric different to air, such as oxide, is known to shift plasmonic resonance in metallic nanoparticles; however, it does not lead to the appearance of new resonances. In the absence of graphene (g=0), equation (6.1) gives Fröhlich resonance condition of a bare SiC nanoparticle, 940.5 cm^{-1}.

Further, we analysed the field distribution at the resonances for bare SiC NW and graphene/oxide/SiC NW models. Figures 6.2a-b show the calculated electric field distribution (|E|) for bare SiC NW/Si at the resonances for TO mode and LSPhP (at 940.5 cm^{-1}) where maximum electric fields are around the SiC NW surface. This is also shown by the magnitude of electric fields calculated along a cutline in the z-direction (yellow vertical dash lines in Figure 6.2a-b), showing a high electric field at the surface of the SiC NW exponentially decaying inside the SiC core (Figure 6.2c).

We subsequently calculated electric field distribution profiles of the graphene/ oxide/ SiC NW model for M1, TO, and M2 modes (Figure 6.2d-f). After introducing oxide between graphene and SiC NW, the electric field distribution became significantly confined within the oxide layer. This is explained by the calculated magnitude of electric fields along the cutline (yellow vertical dash lines in Figure 6.2d-f), showing the electric field increasing inside the oxide and exponentially dropping inside the SiC (Figure 6.2g). It is noticeable that the magnitude of electric field intensity in the graphene/oxide/SiC NW is one order of magnitude higher than the calculated electric fields on the bare SiC NW model (Figure 6.2c and Figure 6.2g). Vector plots of the fields for M1 and M2 can be found in Appendix C, Figure.C.2.

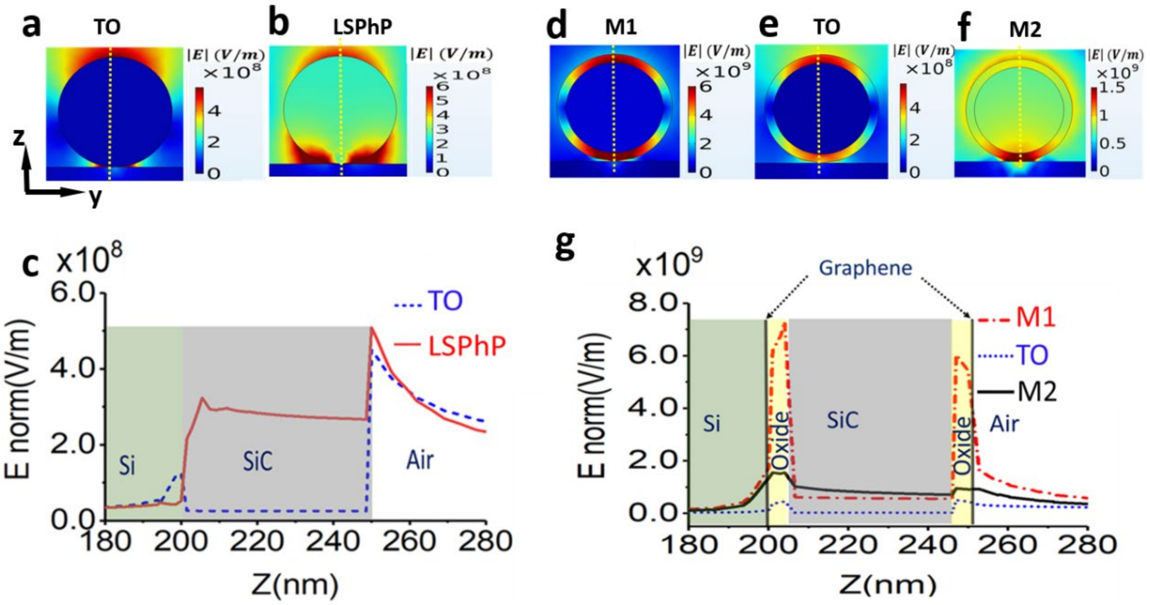

Figure 6.2. Simulated electric field distribution profiles and the magnitude of electric field intensities. (a) & (b) simulated electric field distribution profile on bare SiC NW for TO mode at 797 cm^{-1}and LSPhP at 940.5 cm^{-1} showing the majority of field concentrated around the SiC NW surface, (c) magnitude of electric field intensity calculated along the cutline (yellow vertical dash lines in a&b) on bare SiC NW for TO and LSPhP modes, (d) -(f) calculated electric field distribution profiles on graphene/oxide (4 nm)/SiC NW for M1 mode at 714 cm^{-1}, TO mode at 797 cm^{-1} and M2 mode at 1067 cm^{-1} showing maximum fields concentrated inside the oxide layer (g) the calculated magnitude of electric field intensity along the cutline (yellow vertical dash lines in d-f) for the graphene/oxide/SiC NW for M1 mode at 714 cm^{-1}, TO mode at 797 cm^{-1} and M2 mode at 1067 cm^{-1} demonstrating strong enhancement of the field within the oxide shell layer.

6.2.3. The effect of the oxide shell thickness and refractive index on the MIR response: sensitivity studies

As the experimental nanowires forest is expected to have varying NW diameters and hence also varying oxide thicknesses, we examined the effect of the oxide shell thickness on the system's absorbance and electric field intensities. The simulations were performed for oxide shell thickness between zero (no oxide, only graphene shell) and 15 nm, while the NW's total diameter was kept constant at 50 nm, i.e., the reduced size of the SiC core is compensated by oxide thickness. In Figure 6.3a, the simulated absorbance at different oxide layer thicknesses revealed a blue shift of the modes when the oxide thickness is increased. Also, the absorption intensity of M1 is weakened while the absorption intensity for M2 is enhanced. We also note that for an oxide thickness between ~6 and 10 nm, the M1 position falls in close proximity to the bulk TO mode, leading to complete overlap for an oxide shell of about 7-8nm thickness and creating a misleading impression of an enhanced TO peak.

We subsequently calculated electric field enhancement for M1 and M2 using equation (6.3):

$$\boldsymbol{E}_{enhancement} = \frac{|\boldsymbol{E}|}{|\boldsymbol{E}_0|} \tag{6.3}$$

where $\boldsymbol{E}$ represents electric field calculated along the vertical cutline (yellow vertical line in Figure 6.2d-f) in graphene/oxide/SiC NW model, while $\boldsymbol{E}_0$ is electric field calculated at the same point along the cutline without graphene/oxide/SiC NW in the model.

The calculated peak field enhancement showed a more substantial field enhancement of M1 than M2 (Figure 6.3b). The strongest peak field enhancement for M1 corresponds to oxide with a smaller thickness. Three scenarios occurred for M1 while varying the oxide thickness: under-coupling, optimal coupling, and over-coupling[283]. From Figure 6.3b, optimal coupling for M1 corresponds to an oxide thickness of ~ 1 nm, where a maximum peak field enhancement of about 60 is calculated. Below 1 nm, different physics might apply due to the 2D nature of the material. However, for an oxide shell thickness of zero, i.e., no oxide between the SiC core and the graphene outer shell, the M1 enhancement drops dramatically (over-coupling), as well as for thicknesses over 10nm (under-coupling). It is also worth noting that the oxide layer appears to have a more dramatic influence on M1 than M2.

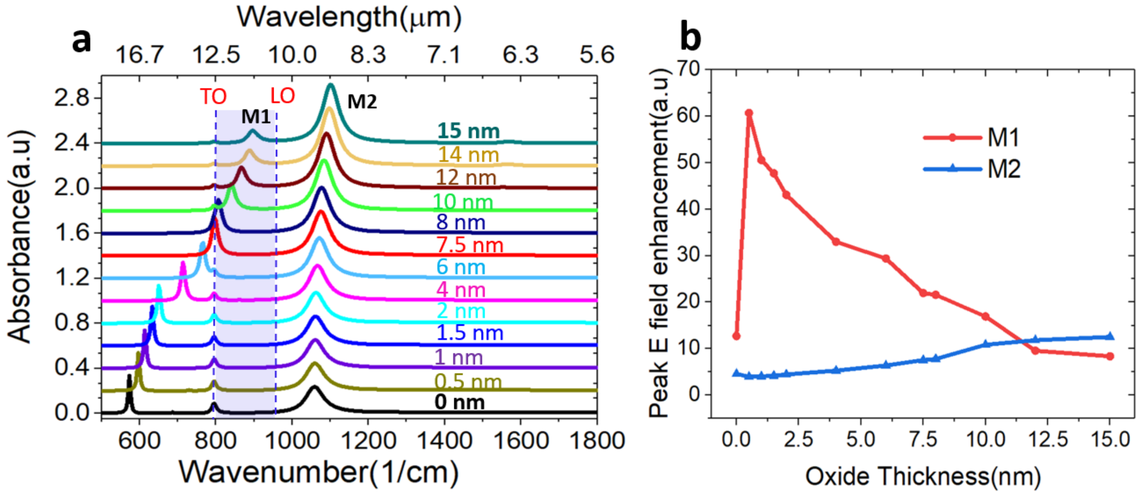

Figure 6.3. (a) Simulated absorbance of graphene-coated SiC nanowires at different oxide layer thicknesses, (b) The calculated peak field enhancement for different oxide shell thicknesses. Field

enhancement was calculated at the peak absorption for each oxide shell thickness. Note that for an oxide shell thickness of zero, i.e., no oxide between the SiC core and the graphene outer shell, the M1 field enhancement drops dramatically, as well as for thicknesses over 10nm.

In addition, we performed a sensitivity study by varying the oxide shell refractive index (n) and observing the effect on the MIR response of the graphene/oxide/SiC NWs. The shell of the graphitised 3C-SiC nanowires consists of a low-density SiOC medium[35, 36], where the SiC has been gradually depleted of its carbon due to the solid-source graphitisation process. Therefore, it is safe to assume that its refractive index would not be uniform through the entire shell. Hence, we performed the simulation by varying the refractive index of the oxide between 1 (air gap) and 2.5 (pure silicon carbide, as if no oxide was present between SiC and graphene). Figures 6.4a and b show the absorption spectra and profile map calculated for a fixed nanowire size of 50 nm diameter (thickness of oxide=7.5 nm and diameter of SiC=35 nm). Both M1 and M2 redshift, the absorption intensity of M1 is enhanced, while the intensity of M2 weakens when the oxide shell refractive index is increased.

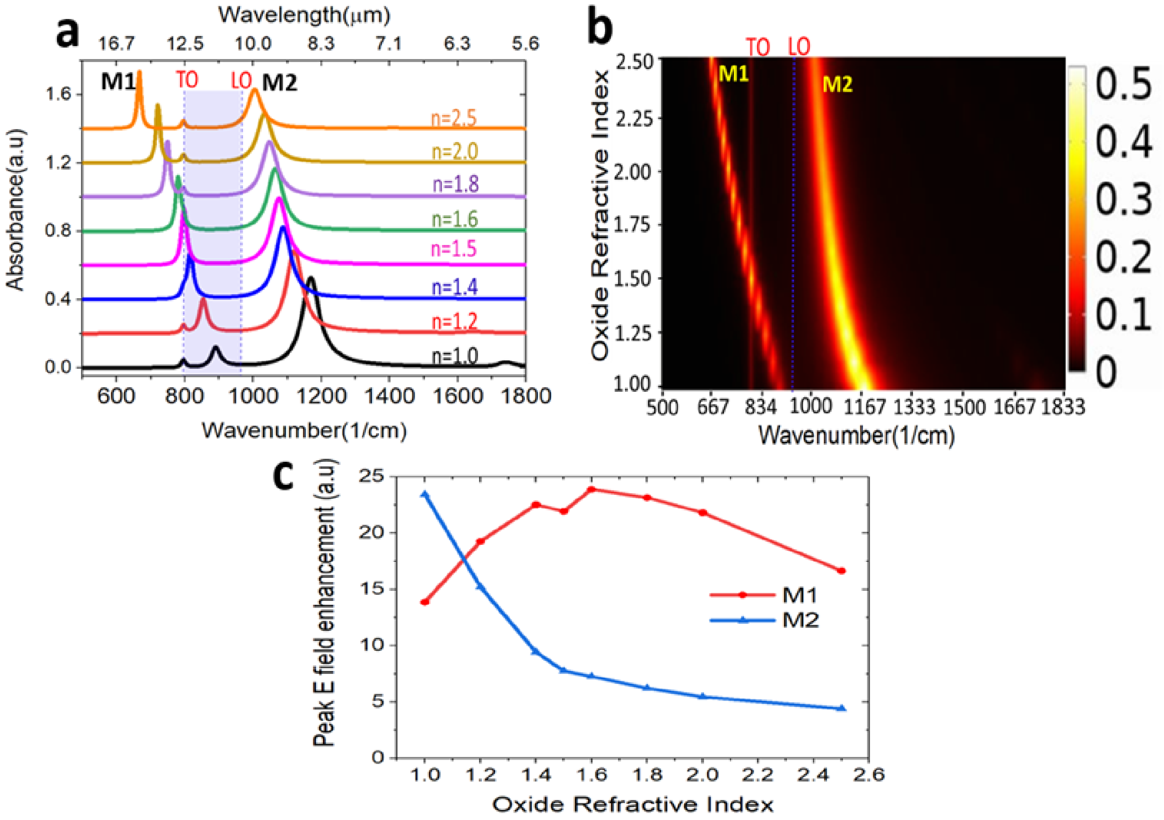

Figure 6.4. Simulated data of graphene/oxide/SiC NW at a different oxide's refractive index, (a) absorbance spectra, (b) mode position and intensity for different oxide refractive index, (c) peak electric field enhancement.

We also analysed the electric field enhancement at the resonance for different oxide refractive indexes using equation (6.3). The calculation revealed the high field enhancement of ~24 for M1, corresponding to n ~1.6 (Figure 6.4c). This happens as a result of M1 being located closer to the TO frequency, where SiC exhibits the largest permittivity, which is vital for highly confined surface modes[309, 310]. The calculated peak electric field enhancement for M2 revealed the highest enhancement of ~24 when n=1 (air) is used for the shell between SiC and graphene, then dropping monotonically for higher refractive indexes.

6.2.4. The effect of silicon carbide core diameter on the MIR response of core/shell silicon carbide/graphene nanowires

We performed a sensitivity study by varying the diameter of the SiC core and recording the effect on the MIR response of the graphene/oxide/SiC NWs. We increased the diameter of SiC from 10 nm to 90 nm and kept oxide shell thickness fix to 7.5 nm. The simulated absorption spectra and profile map at different SiC diameters are shown in Figure 6.5a and Figure 6.5b.

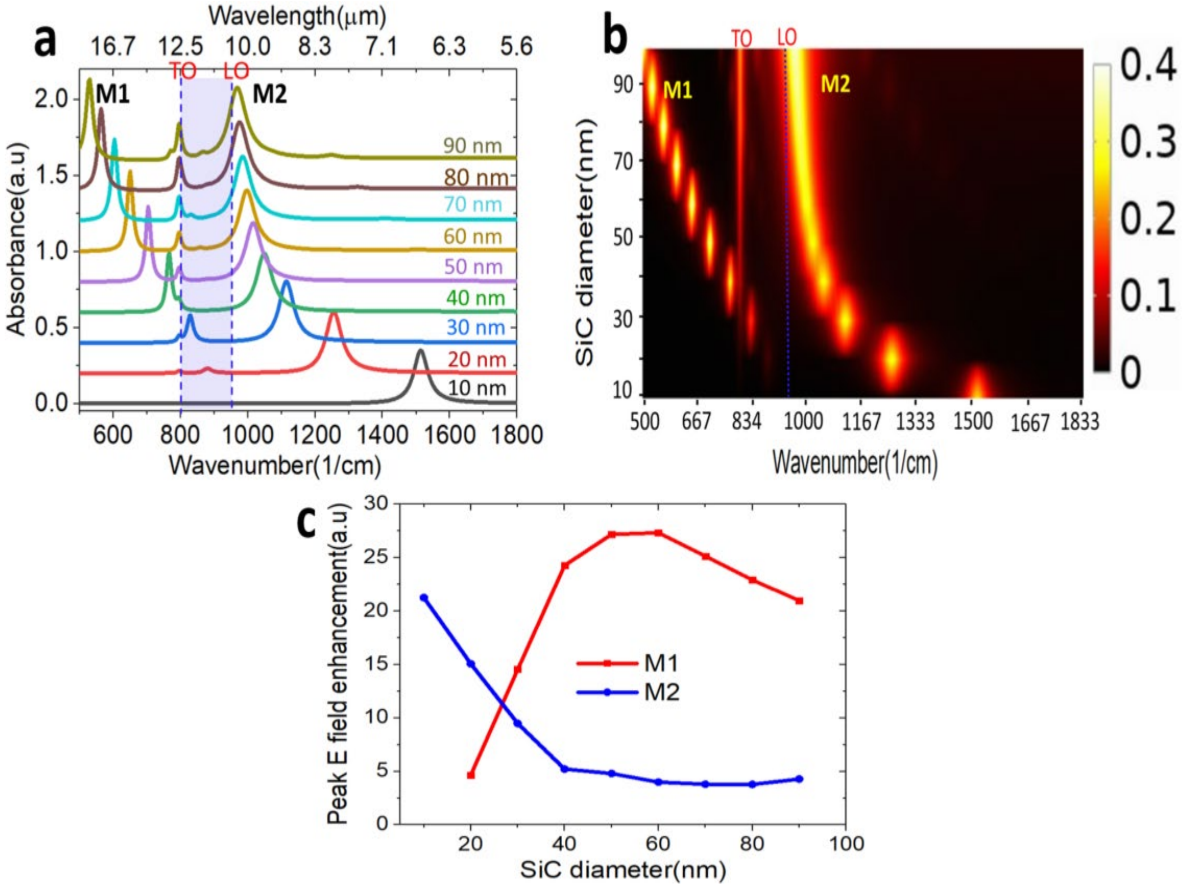

Figure 6.5. Effect of the diameter of SiC core on the absorption and field enhancement of graphene/oxide /SiC NW model. (a)Simulated spectra absorption and (b) colour profile map showing

the spectra absorption profile at different SiC diameters, (c) peak field enhancement at different SiC core diameters.

The simulated absorbance revealed a redshift effect for both M1 and M2 when the diameter of SiC is increased. For a smaller diameter of 10 nm, the TO mode is not noticeable in the absorbance spectra as this is a bulk mode which intensity is entirely dependent on the size of SiC. We also noticed that the intensity of M1 becomes very weak for smaller SiC diameters and disappears for diameters below 20 nm while it gets enhanced for larger SiC diameters.

Moreover, we calculated the electric field enhancement for different SiC diameters. As shown in Figure 6.5c, the calculated peak electric field enhancement increases with increasing SiC diameter and reaches the highest enhancement value of ~27 when the diameter of SiC is ~ 50 nm and dropping monotonically for diameters >50 nm. For M2, the field enhancement is higher for smaller SiC diameters, with the highest enhancement of ~22 realised for SiC diameter of 10 nm, while electric field enhancement drops significantly for larger SiC diameters.

6.2.5. Dynamic tunability analysis at different graphene Fermi energy

Among the exciting properties of graphene is its electrostatic gate- tunability of the carrier concentrations/Fermi energy, which makes the SPP modes supported in this material dynamically tunable. The carrier concentrations in graphene can be increased from ~ 10^{11} cm^{-2} to 10^{13} cm^{-2}as a consequence of the Dirac fermions linear dispersion in this material[6]. To investigate the dynamic tunability of the modes in our graphene/oxide/SiC NW system, we fixed the diameter of nanowires to 50 nm (thickness of oxide=7.5 nm and diameter of SiC=35 nm) and refractive index of oxide to 1.5. We also assumed a constant relaxation rate $\tau = 370\ fs$ in equation (2.65). Then we performed the simulation at varying Fermi energy (E_F) ranging from 0.212 eV to 0.40 eV according to the reported value of carrier concentrations in EG on flat 3C-SiC/Si[34]. The simulated absorbance spectra and the absorption profile map showing the tunability of M1 and M2 in graphene/oxide/SiC NW are shown in Figure 6.6a and Figure 6.6b. A blueshift effect of ~ 150 cm^{-1} for M1 and ~128 cm^{-1} for M2 was realised by increasing graphene's Fermi energy from 0.212 eV to 0.4 eV.

Moreover, the calculated E-field enhancement at the resonance frequencies for different E_F revealed up to ~26 enhancement of the field for M1 corresponding to graphene's E_F of ~ 0.3 eV (Figure 6.6c). It was also noticed that the E field for M2 gets enhancement as the E_F increases with maximum field enhancement of ~10 realised when the E_F of graphene is 0.4 eV.

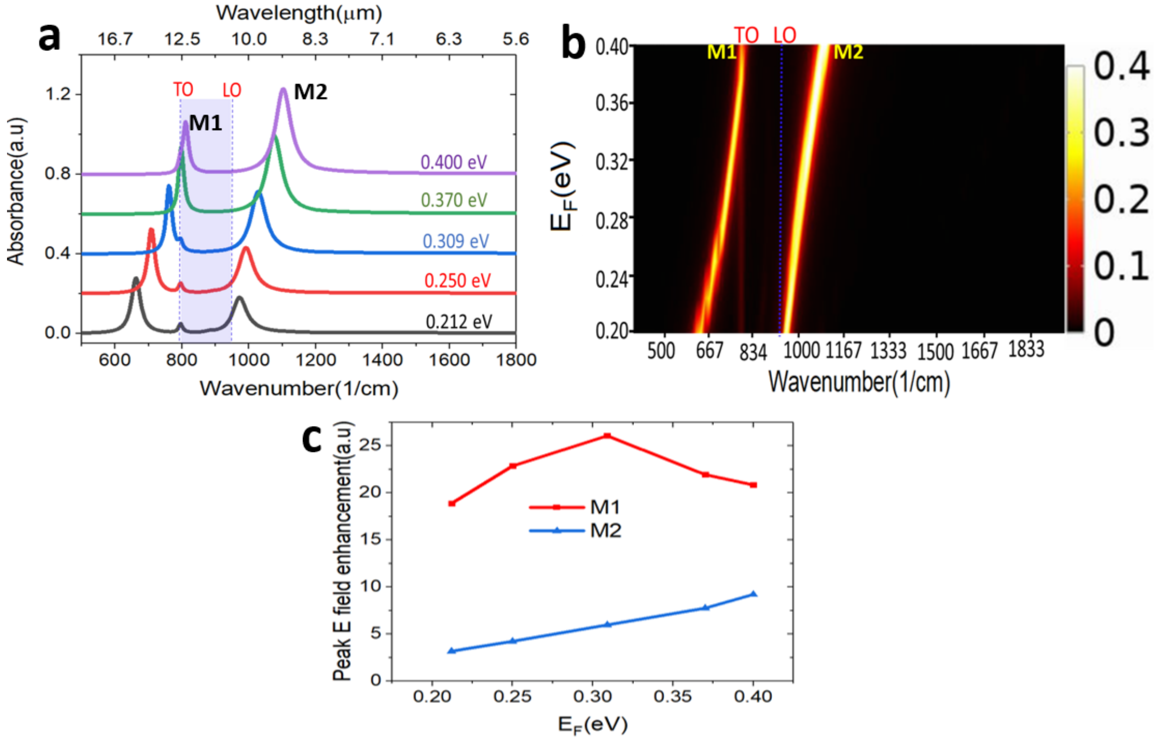

Figure 6.6. Dynamic tunability analysis for M1 and M2 in graphene/oxide/SiC NW. (a) The simulated absorptions spectra showing a blue shift effect on M1 and M2 when the Fermi energy (E_F) in graphene is increased, (b) colour profile map showing the spectra absorption profile at different graphene's Fermi energy E_F, (c) peak field enhancement for different Fermi energy showing high peak field enhancement of ~26 for M1 and ~10 for M2.

6.3. Experimental characterisation of mid-infrared photon response in core/shell silicon carbide/graphene nanowires

6.3.1. Graphitisation and material characterisation

The bare 3C-SiC NWs were grown on Si (100) substrates at the IMEM-CNR Institute, Italy, using a chemical vapour deposition reactor at 1100°C, with Nickel nitrate [$Ni(NO_3)_2$] and carbon monoxide used as a catalyst and gaseous precursor, respectively. More details about the growth of 3C-SiC NWs on Si substrates were reported in[311]. The as-grown nanowires possess two characteristics: 1) they are of a core-shell type, where the core is cubic SiC, and the shell is composed of a very thin oxygen-rich layer 2) their growth temperature of 1100 °C, together with the presence of oxygen and nickel may lead to a sporadic and incomplete graphitisation of the wires surface concurrently to their growth[36]. In this work, we have investigated two batches of SiC nanowires with different amounts of unintended graphitisation, the first with barely any (bare SiC nanowires) and the second one with a greater extent of graphitisation (weakly graphitised).

The graphitisation of 3C-SiC NWs was performed using Ni/Cu catalytic alloy mediated growth using the SiC nanowires as a solid source of carbon[33, 36]. Thanks to the liquid phase epitaxial growth nature of this synthesis technique and hence the long and efficient adatom diffusion, the graphene grown via this process can conformally coat the nanowires. In addition, a few nm thick, highly oxidised (silicon oxycarbide) layer is simultaneously formed in between graphene layers and SiC[35, 36]. A catalytic graphitisation process of the 3C-SiC NWs is shown in Figure 6.7.

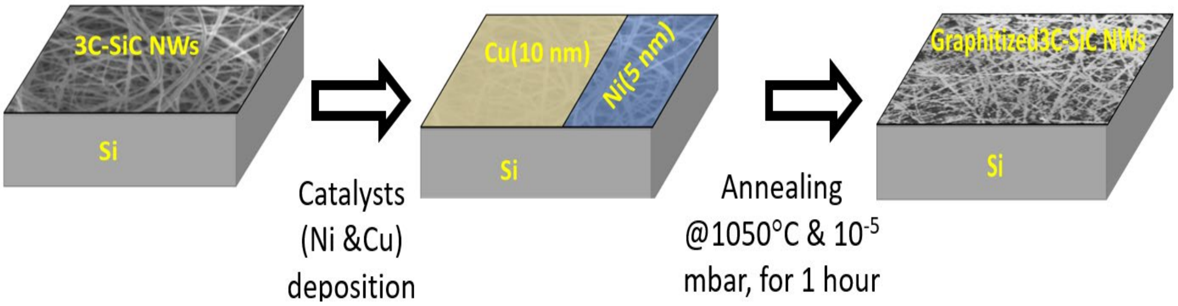

Figure 6.7. Schematic demonstrating a catalytic graphitisation process for epitaxial graphene growth on silicon carbide nanowires on a silicon substrate.

Using a Cryopump deposition chamber with a vacuum pressure of ~ 10^{-5} mbar and deposition current of 200 mA current, a double blanket layer of Nickel (Ni ~ 5 nm) and copper (Cu~ 10nm) were sputtered on 3C-SiC NWs/Si substrates. Ni/Cu/3C-SiC NWs/Si samples were then annealed at a high temperature of ~ 1050° C (25° C/min) for an hour under the medium vacuum condition of ~ 10^{-5} mbar and then gradually cooled down to the room temperature. Note that no final wet etch was performed on the graphitised nanowires to remove residual metal catalysts and excess carbon due to the low adhesion of the nanowires to their substrate.

6.3.2. Surface morphology and Raman characterisation of graphitised silicon carbide nanowires

Surface morphology characterisation of the NWs samples before and after graphitisation was performed using a Zeiss Supra 55 VP high-resolution emission scanning electron microscope operated at 2 kV. The scanning electron microscope (SEM) images of the bare and graphitised 3C-SiC NWs samples are shown in Figures 6.8a and b. The average diameter of as-grown 3C-SiC NWs varies between 40 nm and 50 nm (Figure 6.8a). More morphology characteristics along with energy-dispersive X-ray spectroscopy (EDS) and transmission electron microscope (TEM) data of as grown 3C-SiC NWs was reported in[36]. A decrease in the diameter of SiC NW and increased granularity is seen after graphitisation as the nanowires are a solid source for the carbon in the graphene (Figure 6.8b). The diameter distributions of the nanowires estimated from the SEM images before and after graphitisation are reported in Appendix C (Figure B.4). The fully graphitised SiC NWs possess a shell of low-density oxide (silicon oxycarbide) medium between the graphene and SiC NWs. This directly results from the catalytic graphitisation of 3C-SiC NWs and also occurs on flat surfaces[33, 35, 36]. The formed oxide medium has varying thicknesses due to the varying diameter of the as-grown bare SiC NWs, as shown by transmission electron microscope (TEM) data[36].

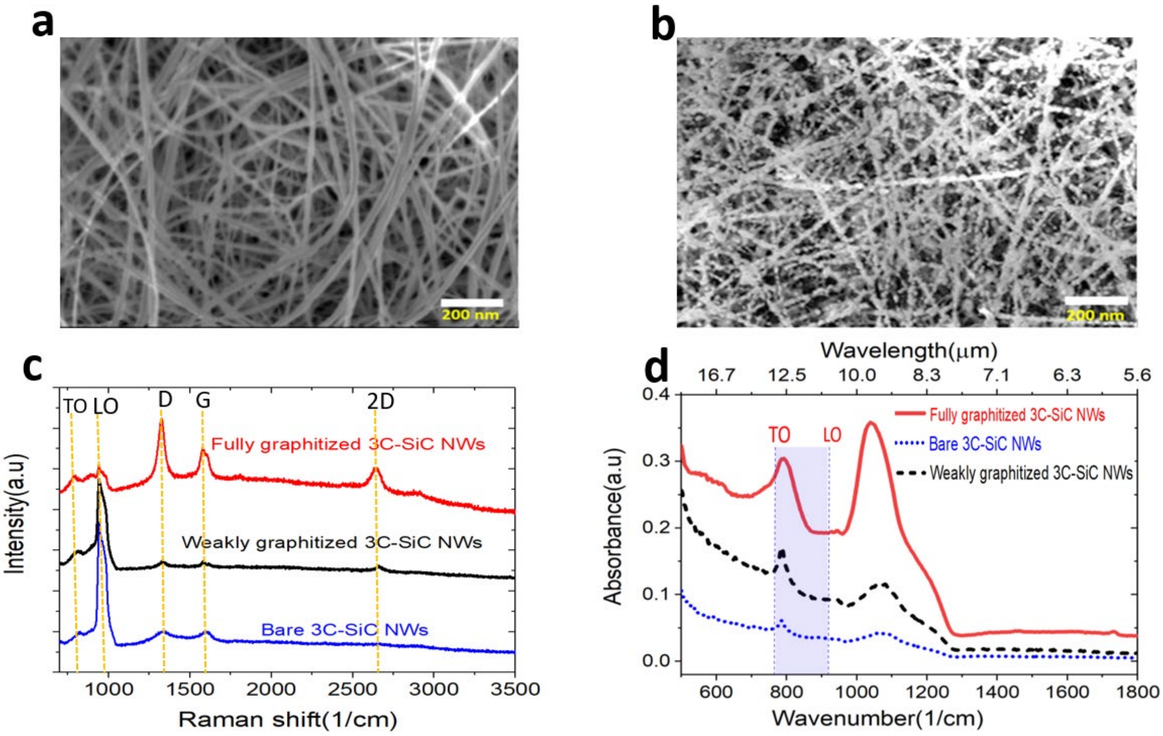

Figure 6.8. Morphology, Raman, and infrared characterisation of the 3C-SiC NWs samples. SEM images of (a) bare and (b) graphitised 3C-SiC NWs. (c) The measured Raman spectra for bare 3C-SiC NWs, the weakly and fully graphitised 3C-SiC NWs. Note that the Raman spectra are intentionally offset for comparison. (d) The measured absorbance for bare 3C-SiC NWs, the weakly and fully graphitised 3C-SiC NWs. The highlighted spectral range between TO and LO represents the Reststrahlen band, where SiC can support a surface phonon polariton mode.

Raman spectroscopy of the nanowires was performed with a Renishaw inVia Raman microscope activated by a 633 nm laser. The measurements were conducted on 9 different spots on 1 cm × 1 cm size samples, and the D and G and 2D spectral intensities were recorded. In Figure 6.8c, the Raman spectrum of bare SiC NWs revealed the TO and LO phonon modes at 797 cm^{-1} and 973 cm^{-1}, respectively, which are the characteristics of 3C-SiC. The LO peak is convoluted with the Raman response from the silicon substrate, as expected[36, 312, 313].

Extremely weak peaks around the positions of the D and G bands of graphene are observed for the bare 3C-SiC NWs, showing a negligible extent of unintended graphitisation of the wires. This effect is more prominent on the second batch of as-grown SiC nanowires, which henceforth we refer to as "weakly graphitised." The Raman spectrum of the weakly graphitised NWs shows, in addition, a faint fingerprint of the 2D peak at 2684 cm^{-1}.

Fully (and intentionally) graphitised 3C-SiC NWs revealed prominent D, G, and 2D bands at 1340 cm^{-1}, 1578 cm^{-1}, and 2684 cm^{-1}, respectively, matching the characteristic of epitaxial graphene on 3C-SiC on Si[33]. However, a large average D over G band intensity ratio (I_D/I_G) of 1.13 as compared to the I_D/I_G of ~0.2 in the normal epitaxial graphene grown on flat 3C-SiC on Si samples[34] is a characteristic of the graphitised SiC NWs due to their small diameter of 40-50nm.

6.3.3. Infrared characterisation of graphitised silicon carbide nanowires

The IR spectroscopy of the samples was performed at room temperature with a Thermo Scientific Nicolet 6700 using an Attenuated Total Reflectance Fourier Transformed Infrared (ATR-FTIR) spectrometer. The diamond crystal with 45° of the incident radiation was used for the ATR system. The samples' absorption spectra were collected using 100 scans, and the average intensity was reported in arbitrary units. The IR absorption characteristics of the as-grown and graphitised SiC NWs are reported in Figure 6.8d.

A comparison of the experimental data from Figure 6.8d and simulated results for oxide thickness =7.5 nm (red curve from Figure 6.3a) is shown in Figure 6.9. Both experimental and simulated absorbance of the bare SiC nanowires shows low IR absorption with a weak but sharp absorption peak at ~797 cm^{-1}, corresponding to the 3C-SiC TO mode. The simulated LSPhP mode at ~940.5 cm^{-1} is weak and broad in measured absorbance spectra on the bare SiC nanowires sample, making it unlikely to be observed in our experimental forest of nanowires. The weak broad absorption measured around 1050 cm^{-1} cannot be attributed to a phonon-polariton as it is outside of the SiC Reststrahlen band and hence is attributed to vibrational resonances of hydroxyls and epoxy functional groups[314, 315] stemming from the oxide in the outer shell of the as-grown SiC nanowires[36, 311]. The IR absorption spectra of the weakly graphitised NWs (Figure 6.8d) show similar fingerprints but with an increased absorbance.

The experimental IR spectrum of fully graphitised SiC nanowires reveals a substantial 5 to 9 -fold enhancement for the two measured absorption modes, as compared to the bare SiC nanowires. Interestingly, one of the experimental modes seems to overlap with the SiC TO, around 797 cm^{-1}. An absorption enhancement of the bulk TO mode can be excluded, as in fact the total volume size of SiC nanowires is expected to decrease after graphitisation because of the consumption of the SiC, solid source for the catalytic graphitisation, while the oxide outer shell in between the SiC and the graphene is increased to a typical value of ~8-10 nm as observed experimentally with transmission electron microscope[36, 311]. From the simulated spectra in Figure 6.3a, oxide shells roughly in the 6-10 nm thickness range would lead effectively to the overlap of TO and M1 modes (see also Figure 6.5 for absorption of SiC at different nanowire diameters). Simulated oxide shell thickness of 7.5nm and a refractive index of 1.5, corresponding to a generic silicon oxycarbide medium[306], was chosen for comparison of simulation and experiment. Therefore, we suggest that there is an overlap between the TO and M1 responses. This all indicates that surface polariton phenomena are at work in this material system.

The second mode at around 1050 cm^{-1} from the measured absorbance on the fully graphitised SiC nanowires is particularly broad and shows a significant enhancement. While we expect that the hybridised mode M2 would correspond to the experimental position of this second mode, as shown by the simulated spectrum in Figure 6.9, it is worth noting that here we are likely to observe a convoluted response caused by the vibrational resonances of epoxy-functional groups present in the nanowires sample. In addition, the fact that those groups are physically concentrated in the oxide shell between the SiC core and the graphene outer shell would likely lead to further amplification of their IR fingerprint, thanks to the field concentration taking place in the oxide, as shown in the electrical fields in Figure 6.2g.

The regular simulated pattern with minimal cross-talk between wires (Figure 6.1a) is clearly highly simplified with respect to the highly irregular experimental NWs forest in the SEM images (Figure 6.8a and b), with random wire pitch, orientation, and varying diameters (see distribution in Appendix C, Figure C.4). However, the simplified model provides enough fundamental information to interpret the more complex response from the experimental forest of nanowires.

The key differing aspects are those of varying spatial orientation, varying dimensions, and the presence of cross-wire interactions. The response of randomly oriented nanowires effectively provides a combined response to irradiation by incident waves with electric field orientation both along and across the wires. Note that the predominantly vertical E_Z field leads to similar dipolar responses for either orientation of the incident electric field, except that the TO peak is absent when there is no field component along the wire (as shown in Appendix C, Figure C.3). The experimental size distribution is expected to introduce a strong peak broadening (see Figure 6.5 for spectra simulated for different nanowire sizes) and the additional cross-wire interactions that were neglected in the numerical model but are not expected to change the fundamental nature of the response.

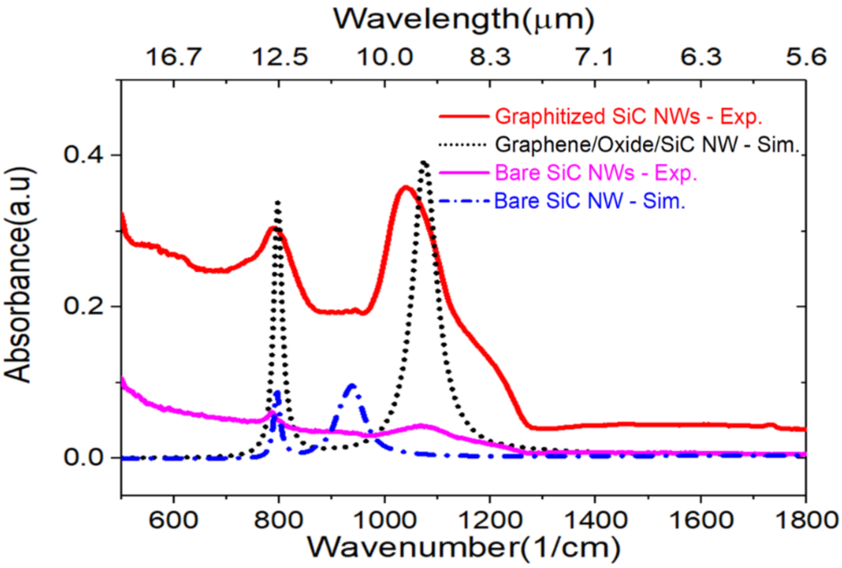

Figure 6.9. A comparison of the measured IR absorbance spectral of bare and fully graphitised 3C-SiC NWs and the simulated absorbance on bare SiC NW and graphene/oxide/SiC NW with an oxide shell thickness of 7.5nm and refractive index of 1.5.

6.4. Summary

In this chapter, we have shown an experimental 9-fold absorption enhancement in graphene-coated SiC nanowires as compared to the absorption of as-grown, bare SiC nanowires. With the help of finite element multiphysics modelling, we attribute this effect to the hybridisation of the surface phonon in SiC and the surface plasmon response in graphene. Furthermore, we revealed this hybridisation to generate a mode splitting and extend the graphitised nanowires' spectral resonances beyond the SiC's Reststrahlen band.

We also show that the oxide layer between the graphene shell and the SiC core acts as a coupling medium, leading to a substantial absorption and electric field enhancement. We indicate extreme subwavelength confinement for a MIR wavelength of around ~ 10 μm within a few nanometers (< 10 nm) of the oxide shell medium. Additionally, the model indicates that a more ordered and periodic nanowire structure could potentially lead to even higher enhancement factors up to 60 times, and we indicate that this effect can also be used to enhance the IR fingerprint of molecules physically trapped in the intermediate shell (epoxy molecules, in this case). We believe that these findings open up a promising avenue towards tunable MIR molecular sensors and detectors based on graphene/3C-SiC nanostructures.

Chapter 7. Conclusions and Future works

7.1. Conclusions

In order to realise sub-diffraction photonics, the choice of the constituent materials and tailoring of the operational spectrum are two critical factors that need special consideration. Photonic systems with low optical losses and dynamically tunable can offer a broader range of spectral and functional flexibility, and graphene can offer such opportunities while supporting the sub-diffraction confinement of optical fields. The coupling of graphene with polar materials that support low loss SPhPs offers further opportunities to improve the loss characteristics beyond what is achievable in graphene SPPs alone in MIR and FIR frequencies.

This study shows that the realisation of high-performance (low optical losses and tunable) nanophotonic systems could be best achieved via a tailored combination of graphene and polar material to generate hybrid phonon plasmon polariton modes in a device. While previously, the coupling between SPPs in graphene with SPhPs in polar substrates was achieved using mechanically transferred graphene[28, 316, 317], EG offers the opportunity to realise epitaxially grown graphene directly on SiC[29, 135, 318]. Notably, our alloy catalytic growth method enables EG growth on SiC on silicon[28, 33-35], offering unique opportunities to couple tunable graphene SPPs with long-lifetime SPhPs in SiC in a single versatile optical platform. The recent progress in the quality and control of epitaxial graphene on SiC on silicon opens unique opportunities for the fabrication over large scales of any complex three-dimensional nanophotonics, which could also be integrated with silicon processing technologies.

In this thesis, we first demonstrated the excitation of propagating surface phonon polariton in a flat SiC/Si system and revealed a large wavevectors /momentum mismatch between graphene's plasmon and incident photon that impedes graphene's SPP mode excitation in a flat EG/SiC/Si system.

Second, we have used epitaxial graphene on silicon carbide nanowires, grown bottom-up as a disordered "forest", as a test platform to reveal the fundamental optical properties of EG on cubic silicon nanostructures. We have shown that the momentum mismatch can be overcome using the graphene/SiC nanowires system via the excitation of localised surface phonon and surface plasmon polariton modes in SiC and graphene. Subsequently, we have demonstrated a substantial enhancement of the MIR photons absorption and broadening spectral resonances outside the SiC's Reststrahlen band, which resulted from the hybridisation of localised SPhP-SPP modes in the graphene/SiC nanowires system.

Furthermore, we have revealed extreme subwavelength confinement of the MIR photons of ~ 10 μm wavelength within a few nanometers (< 10 nm) thick oxide layer between the graphene and SiC. This intermediate oxide shell layer is inherently realised during our EG alloy catalytic growth method and acts as a coupling medium between the SiC core and graphene outer shell. The study also demonstrated the potential for dynamic tunability of hybrid polariton modes in the graphene/SiC nanowire model, as revealed by the modes' resonances shift when graphene's Fermi energy is tuned according to the measured carrier concentrations on our EG/3C-SiC/Si samples.

The sensitivity studies performed on the graphene/SiC nanowire model suggested further enhancement of the MIR photons absorption and field confinement for EG/SiC-based metasurfaces with periodically ordered patterns on silicon.

7.2. Future works

- Design, fabricate and develop periodically ordered metasurfaces using a top-down approach utilising the EG on SiC on silicon platform[33-35] to achieve various objectives such as ultra-compact multi-modal MIR detector for image detection and remote and molecular sensing. This can be now achieved by using the platform developed in our group[37, 319].
- Design and investigate the fabricated metasurfaces' sensitivity to polarisation, phase and different angles of incident electromagnetic radiation.
- Examine the dynamic tunability capability of the fabricated EG/SiC/Si-based metasurfaces using the gate-tuning approach.

Appendices

Appendix A. Derivation of the equation for the dispersion of surface polariton at the planar interface between a conductor and a dielectric medium

We define the magnetic field component in the y-direction to be $\boldsymbol{H}_{yi}(z) = \boldsymbol{H}_{0i}e^{ik_x x \pm k_{zi}z}$ (i=1, 2 for the medium 1 and 2 in Figure 2.2).

For $z > 0$, equation (2.27) can be rewritten as

$$\boldsymbol{H}_{y1}(z) = \boldsymbol{H}_{01}e^{ik_x x - k_{z1}z} \tag{A.1}$$

$$\boldsymbol{E}_{x1} = i\frac{k_{z1}}{\omega\varepsilon_0\varepsilon_1}\boldsymbol{H}_{y1}(z) \tag{A.2}$$

$$\boldsymbol{E}_{z1} = -\frac{k_x}{\omega\varepsilon_0\varepsilon_1}\boldsymbol{H}_{y1}(z) \tag{A.3}$$

While for $z < 0$, it can be modified to

$$H_{y2}(z) = \boldsymbol{H}_{02}e^{ik_x x + k_{z2}z} \tag{A.4}$$

$$\boldsymbol{E}_{x2} = -i\frac{k_{z2}}{\omega\varepsilon_0\varepsilon_2(\omega)}\boldsymbol{H}_{y2}(z) \tag{A.5}$$

$$\boldsymbol{E}_{z2} = -\frac{k_x}{\omega\varepsilon_0\varepsilon_2(\omega)}\boldsymbol{H}_{y2}(z) \tag{A.6}$$

The continuity relation suggests that, $\boldsymbol{E}_{x1} = \boldsymbol{E}_{x2}$ and $\boldsymbol{H}_{y1} = \boldsymbol{H}_{y2}$, and it yields the following,

$$i\frac{k_{z1}}{\omega\varepsilon_0\varepsilon_1}\boldsymbol{H}_{y1}(z) = -i\frac{k_{z2}}{\omega\varepsilon_0\varepsilon_2(\omega)}\boldsymbol{H}_{y2}(z) \tag{A.7a}$$

$$\frac{k_{z1}}{\varepsilon_1} = -\frac{k_{z2}}{\varepsilon_2(\omega)} \tag{A.7b}$$

Using $\boldsymbol{H}_{yi}(z) = \boldsymbol{H}_0 e^{ik_{xi}x \pm k_{zi}z}$ and $\frac{\partial^2 H_{yi}}{\partial z^2} = k_{zi}^2\boldsymbol{H}_{yi}$ we can modify (2.28) as follows,

For $z > 0$,

$$k_{z1}^2\boldsymbol{H}_{y1} + (k_0^2\varepsilon_1 - k_x^2)\boldsymbol{H}_{y1} = 0 \tag{A.8a}$$

$$\left(k_{z1}^2 + (k_0^2\varepsilon_1 - k_x^2)\right)\boldsymbol{H}_{y1} = 0 \tag{A.8b}$$

Since $\boldsymbol{H}_{y1} \neq 0$, therefore, $\left(k_{z1}^2 + (k_0^2\varepsilon_1 - k_x^2)\right) = 0$

$$k_{z1}^2 = k_x^2 - k_0^2\varepsilon_1 \qquad (A.9)$$

For $z < 0$,

$$k_{z2}^2\boldsymbol{H}_{y2} + (k_0^2\varepsilon_2(\omega) - k_x^2)\boldsymbol{H}_{y2} = 0 \qquad (A.10a)$$

$$\left(k_{z2}^2 + (k_0^2\varepsilon_2(\omega) - k_x^2)\right)\boldsymbol{H}_{y2} = 0 \qquad (A.10b)$$

$$k_{z2}^2 = k_x^2 - k_0^2\varepsilon_2(\omega) \qquad (A.10c)$$

We can divide (A.10c) by (A.9) to obtain the following (A.11);

$$\frac{k_{z2}^2}{k_{z1}^2} = \frac{k_x^2 - k_0^2\varepsilon_2(\omega)}{k_x^2 - k_0^2\varepsilon_1} \qquad (A.11)$$

We can rearrange (A.7b) to get (A.12)

$$\frac{k_{z2}}{k_{z1}} = -\frac{\varepsilon_2(\omega)}{\varepsilon_1} \qquad (A.12)$$

Equality relation between (A.11) and (A.12) suggests,

$$\left(-\frac{\varepsilon_2(\omega)}{\varepsilon_1}\right)^2 = \frac{k_x^2 - k_0^2\varepsilon_2(\omega)}{k_x^2 - k_0^2\varepsilon_1} \qquad (A.13a)$$

$$\varepsilon_2^2(\omega)k_x^2 - \varepsilon_2^2(\omega)\varepsilon_1 k_0^2 = \varepsilon_1^2 k_x^2 - \varepsilon_1^2\varepsilon_2(\omega)k_0^2 \qquad (A.13b)$$

$$k_x^2(\varepsilon_2(\omega) - \varepsilon_1)(\varepsilon_2(\omega) + \varepsilon_1) = k_0^2(\varepsilon_2(\omega) - \varepsilon_1)\varepsilon_1\varepsilon_2(\omega) \qquad (A.13c)$$

Simplification of (A.13c) leads us to the expression (2.40) representing the dispersion of surface polariton mode at the planar surface between a conductor and a dielectric medium.

$$k_x \equiv k_{SPP} = k_0\sqrt{\frac{\varepsilon_1\varepsilon_2(\omega)}{(\varepsilon_2(\omega) + \varepsilon_1)}}$$

Appendix B. Derivation of the equation for the dispersion relation of surface plasmon polariton in graphene

Equation ((A. 7b)can be rearranged into the following;

$$\frac{\varepsilon_1}{k_{z1}} = -\frac{\varepsilon_2(\omega)}{k_{z2}} \qquad (B.1)$$

By including the conductivity of graphene above equation (B.1) becomes (B.2),

$$\frac{\varepsilon_1}{k_{z1}} + \frac{\varepsilon_2(\omega)}{k_{z2}} + i\frac{\sigma(\omega)}{\omega\varepsilon_0} = 0 \qquad (B.2)$$

Inserting the value of k_{z1} and k_{z2} from relation (A.9) and (A.10c) into (B.2), we can get (B.3);

$$\frac{\varepsilon_1}{\sqrt{k_{spp}^2(\omega) - \frac{\varepsilon_1\omega^2}{c^2}}} + \frac{\varepsilon_2(\omega)}{\sqrt{k_{spp}^2(\omega) - \frac{\varepsilon_2(\omega)\omega^2}{c^2}}} = -i\frac{\sigma(\omega)}{\omega\varepsilon_0} \qquad (B.3)$$

where $k_x = k_{SPP}$

We consider a nonretarded regime where the wavevector of surface plasmon is much higher than that of the light passing through the vacuum (i.e., $k_{spp} \gg \frac{\omega}{c}$)[72, 74]. Therefore expression (B.3) can be simplified into the following expressions:

$$\frac{\varepsilon_1}{\sqrt{k_{spp}^2(\omega)}} + \frac{\varepsilon_2(\omega)}{\sqrt{k_{spp}^2(\omega)}} = -i\frac{\sigma(\omega)}{\omega\varepsilon_0} \qquad (B.4a)$$

$$k_{spp}(\omega) = \frac{i\omega\varepsilon_0\big(\varepsilon_1 + \varepsilon_2(\omega)\big)}{\sigma(\omega)} \qquad (B.4b)$$

$$k_{spp}(\omega) = \frac{i\omega\ \varepsilon_0(\varepsilon_2(\omega) + \varepsilon_1)}{\sigma(\omega)} \qquad (B.4c)$$

At the low frequency and high doping regions, the fermi wavevector (k_F) is greater than the k_{spp} and also, the Fermi energy is superior to the energy of incident light (i.e.,$E_F \gg \hbar\omega$), causing graphene conductivity to be dominated by the intraband electronic contribution and take the form of Drude model as follow.

$$\sigma(\omega) = i\frac{e^2 E_F}{\pi\hbar^2\,(\omega + i\tau^{-1})} \qquad (B.5)$$

where τ is the carrier relaxation time. Replacing conductivity by its expression, k_{spp} becomes;

$$k_{spp}(\omega) = \frac{i\omega\, \varepsilon_0\big(\varepsilon_1 + \varepsilon_2(\omega)\big)}{i\dfrac{e^2 E_F}{\pi\hbar^2\,(\omega + i\tau^{-1})}} \qquad (B.6a)$$

$$k_{spp}(\omega) = \frac{\omega\, \varepsilon_0\big(\varepsilon_1 + \varepsilon_2(\omega)\big)\pi\hbar^2\,(\omega + i\tau^{-1})}{e^2 E_F} \qquad (B.6b)$$

By multiplying and dividing c on the above equation (B.6b), the equality will be kept as in the following equation;

$$k_{spp}(\omega) = \frac{\omega}{c}\frac{c\, \varepsilon_0\big(\varepsilon_1 + \varepsilon_2(\omega)\big)\pi\hbar^2\,(\omega + i\tau^{-1})}{e^2 E_F} \qquad (B.7a)$$

$$k_{spp}(\omega) = k_0\frac{c\, \varepsilon_0\big(\varepsilon_1 + \varepsilon_2(\omega)\big)\pi\hbar^2\,(\omega + i\tau^{-1})}{e^2 E_F} \qquad (B.7b)$$

$$k_{spp}(\omega) = k_0\frac{\big(\varepsilon_1 + \varepsilon_2(\omega)\big)\hbar(\omega + i\tau^{-1})}{4\, E_F} \times \frac{4\pi\hbar c\, \varepsilon_0}{e^2} \qquad (B.7c)$$

Simplification of (B.7c) leads us to the equation for the dispersion relation of surface plasmon polariton in graphene.

$$k_{spp}(\omega) = k_0\frac{\big(\varepsilon_1 + \varepsilon_2(\omega)\big)\hbar\omega(1 + i(\tau\omega)^{-1})}{4\alpha\, E_F} \qquad (B.8)$$

$\alpha = \frac{e^2}{4\pi\hbar c\, \varepsilon_0} \approx \frac{1}{137}$, is a fine structure constant that defines the strength of electromagnetic interaction between elementary charged particles.

Appendix C. Supporting information for chapter 6

C1. Additional simulation models

Four models were built and investigated, as shown in Figure C.1a. We first built a SiC NW/Si model, graphene/air/Si, followed by a graphene/SiC NW/Si model, and then finally, we created a graphene/oxide/SiC NW/Si model. The simulated absorbances for four different models are shown in Figure C.1b.

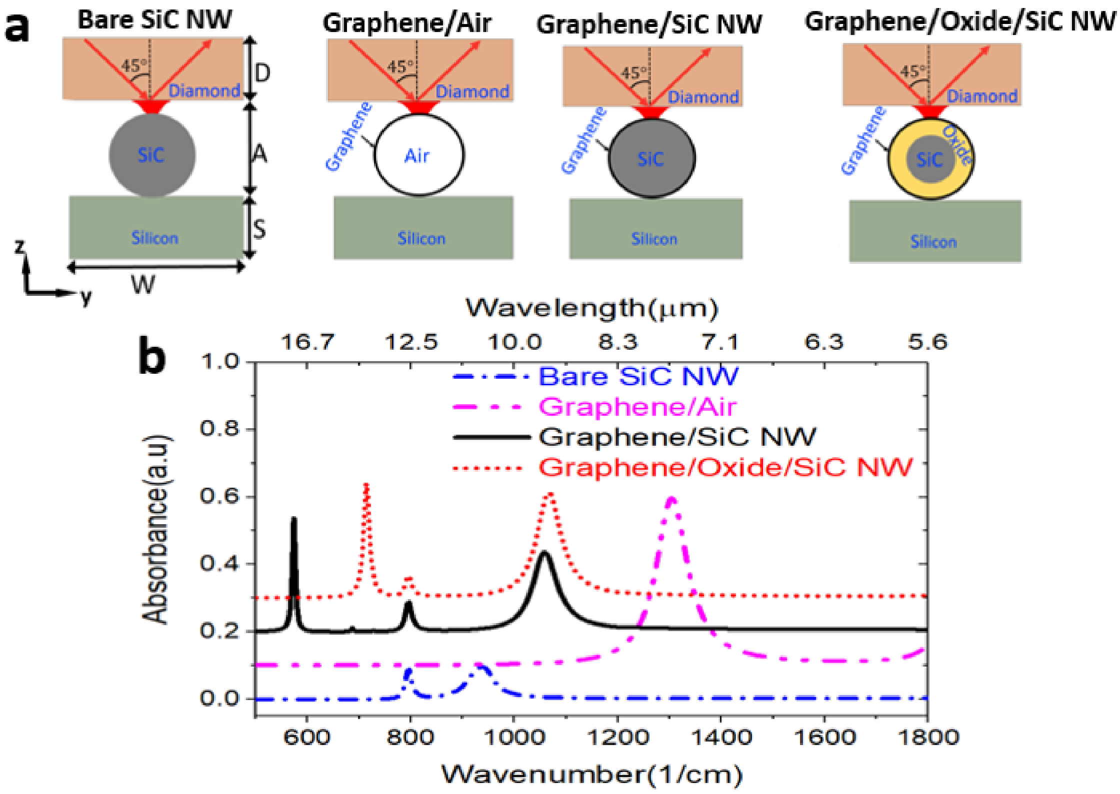

Figure C.1. Electromagnetic simulation model set up. (a) Schematic of 4 different simulated models: Bare SiC NW, graphene/Air, Graphene/SiC NW, and graphene/oxide/SiC NW. (b) Simulated absorbance for four different models: bare SiC NW, graphene/air, graphene/SiC NW, and graphene/oxide/SiC NW. The following geometry parameters were used: W=500 nm, S=200 nm, A=120 nm, D =100nm. For all four simulations, the total nanowire diameter is 50 nm. For the graphene/oxide/SiC NW model, oxide shell thickness is 4 nm while SiC is 42 nm.

C2. Electric field vector analysis for M1 and M2 in Graphene/Oxide/SiC NW model

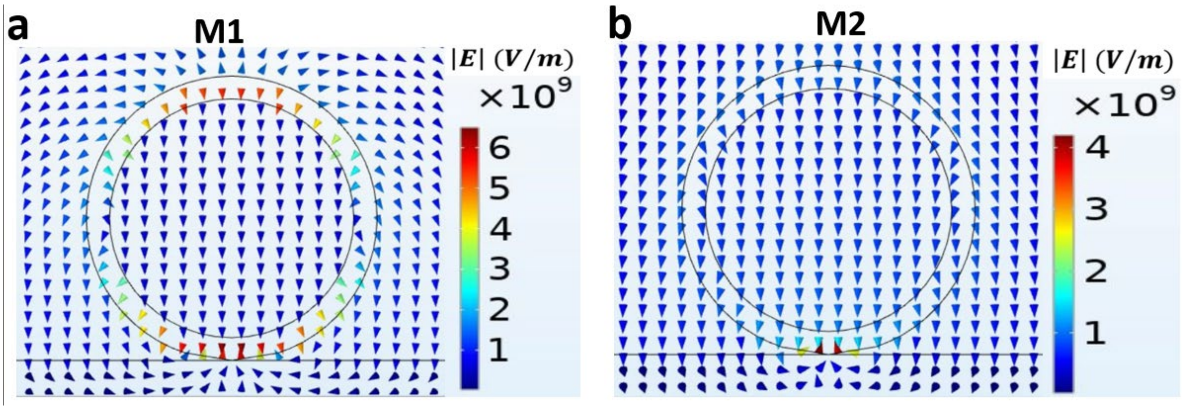

Figure C.2. Electric field vectors for (a) M1 and (b) M2 in graphene/oxide /SiC NW model when oxide shell thickness is 4 nm.

C3. Simulated absorbance for different orientations of the incident field

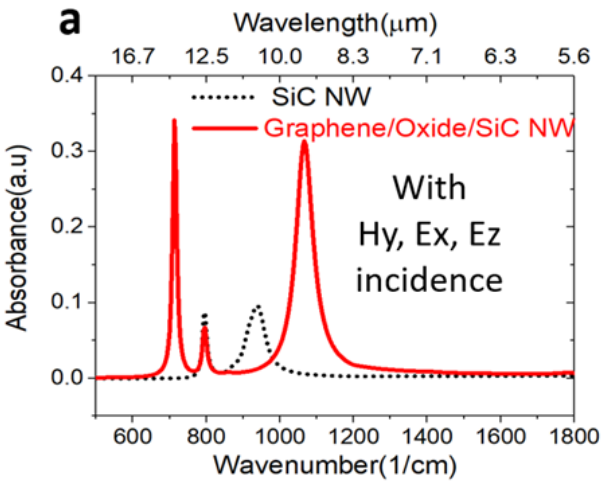

Figure C.3.Absorbance for different orientations of the incident field for 4nm thick oxide layer (a) Hy, Ex, Ez (b) Hx, Ey, Ez. The Ez component in both cases dominates the response. Lack of electric field component along the wire (Ex) significantly reduces TO response in (b).

C4. Nanowires diameter distributions

Figure C.4 shows the nanowires diameters distributions. The diameters distributions were estimated from the SEM image(Figure 6.8a-b) for the bare and graphitised 3C-SiC nanowires using Image J software[320].

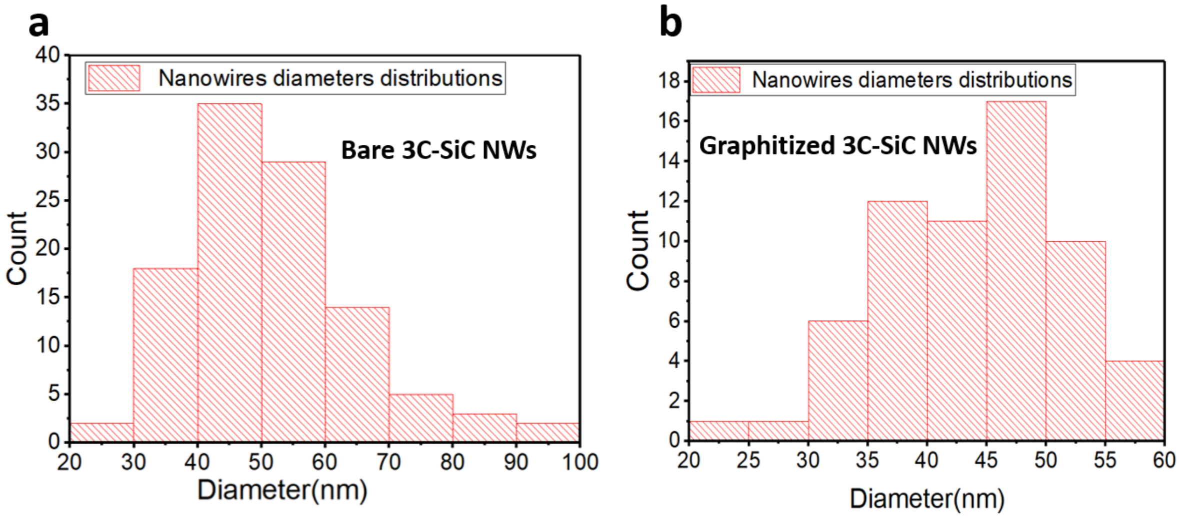

Figure C.4. Nanowires diameter distribution as estimated from SEM data of bare and graphitized 3C-SiC NWs samples using Image J software[320]. (a) Bare 3C-SiC NWs, the average diameter is 48.6 nm (b) fully graphitized 3C-SiC NWs, the average diameter is 44.8 nm.

Bibliography

[1] J. C. Maxwell, "VIII. A dynamical theory of the electromagnetic field," Philosophical transactions of the Royal Society of London, vol. 155, pp. 459-512, 1865.

[2] T. G. Folland and J. D. Caldwell, "Semiconductor Nanophotonics Using Surface Polaritons," in Advanced Study Institute on NATO ASI on Quantum Nano-Photonics, 2017, pp. 235-254: Springer.

[3] T. Folland, L. Nordin, D. Wasserman, and J. Caldwell, "Probing polaritons in the mid- to far-infrared," Journal of Applied Physics, vol. 125, no. 19, p. 191102, 2019.

[4] J. D. Caldwell et al., "Low-loss, infrared and terahertz nanophotonics using surface phonon polaritons," Nanophotonics, vol. 4, no. 1, pp. 44-68, 2015.

[5] J. Takahara, S. Yamagishi, H. Taki, A. Morimoto, and T. Kobayashi, "Guiding of a one-dimensional optical beam with nanometer diameter," Optics letters, vol. 22, no. 7, pp. 475-477, 1997.

[6] T. Low and P. Avouris, "Graphene plasmonics for terahertz to mid-infrared applications," ACS nano, vol. 8, no. 2, pp. 1086-1101, 2014.

[7] Q. Bao and K. P. Loh, "Graphene photonics, plasmonics, and broadband optoelectronic devices," ACS nano, vol. 6, no. 5, pp. 3677-3694, 2012.

[8] F. J. Garcia de Abajo, "Graphene plasmonics: challenges and opportunities," Acs Photonics, vol. 1, no. 3, pp. 135-152, 2014.

[9] A. Grigorenko, M. Polini, and K. Novoselov, "Graphene plasmonics," Nature photonics, vol. 6, no. 11, p. 749, 2012.

[10] D. Rodrigo et al., "Mid-infrared plasmonic biosensing with graphene," Science, vol. 349, no. 6244, pp. 165-168, 2015.

[11] J. D. Caldwell and K. S. Novoselov, "Mid-infrared nanophotonics," Nature materials, vol. 14, no. 4, pp. 364-366, 2015.

[12] M. Liu, X. Yin, and X. Zhang, "Double-layer graphene optical modulator," Nano letters, vol. 12, no. 3, pp. 1482-1485, 2012.

[13] F. Xia, T. Mueller, Y.-m. Lin, A. Valdes-Garcia, and P. Avouris, "Ultrafast graphene photodetector," Nature nanotechnology, vol. 4, no. 12, p. 839, 2009.

[14] T. Mueller, F. Xia, and P. Avouris, "Graphene photodetectors for high-speed optical communications," Nature photonics, vol. 4, no. 5, p. 297, 2010.

[15] Y. Zhang et al., "Broadband high photoresponse from pure monolayer graphene photodetector," Nature communications, vol. 4, p. 1811, 2013.

[16] X. Gan et al., "Chip-integrated ultrafast graphene photodetector with high responsivity," Nature Photonics, vol. 7, no. 11, p. 883, 2013.

[17] G. Ni et al., "Ultrafast optical switching of infrared plasmon polaritons in high-mobility graphene," Nature Photonics, vol. 10, no. 4, pp. 244-247, 2016.

[18] Z. Fang, Z. Liu, Y. Wang, P. M. Ajayan, P. Nordlander, and N. J. Halas, "Graphene-antenna sandwich photodetector," Nano letters, vol. 12, no. 7, pp. 3808-3813, 2012.

[19] M. Ono et al., "Ultrafast and energy-efficient all-optical switching with graphene-loaded deep-subwavelength plasmonic waveguides," Nature Photonics, vol. 14, no. 1, pp. 37-43, 2020.

[20] Q. Bao et al., "Broadband graphene polarizer," Nature photonics, vol. 5, no. 7, pp. 411-415, 2011.

[21] S. Foteinopoulou, G. C. R. Devarapu, G. S. Subramania, S. Krishna, and D. Wasserman, "Phonon-polaritonics: enabling powerful capabilities for infrared photonics," Nanophotonics, vol. 8, no. 12, pp. 2129-2175, 2019.

[22] B. Qiang, A. M. Dubrovkin, H. N. Krishnamoorthy, Q. Wang, N. I. Zheludev, and Q. J. Wang, "Germanium-on-Carborundum Surface Phonon-Polariton Infrared Metamaterial," Advanced Optical Materials, p. 2001652, 2020.

[23] T. Echtermeyer et al., "Strong plasmonic enhancement of photovoltage in graphene," Nature communications, vol. 2, no. 1, pp. 1-5, 2011.

[24] V. W. Brar, M. S. Jang, M. Sherrott, J. J. Lopez, and H. A. Atwater, "Highly confined tunable mid-infrared plasmonics in graphene nanoresonators," Nano letters, vol. 13, no. 6, pp. 2541-2547, 2013.

[25] H. Yan et al., "Damping pathways of mid-infrared plasmons in graphene nanostructures," Nature Photonics, vol. 7, no. 5, pp. 394-399, 2013.

[26] Y. Liu and R. F. Willis, "Plasmon-phonon strongly coupled mode in epitaxial graphene," Physical Review B, vol. 81, no. 8, p. 081406, 2010.

[27] S. Dai et al., "Graphene on hexagonal boron nitride as a tunable hyperbolic metamaterial," Nature nanotechnology, vol. 10, no. 8, p. 682, 2015.

[28] N. Mishra, J. Boeckl, N. Motta, and F. Iacopi, "Graphene growth on silicon carbide: A review," physica status solidi (a), vol. 213, no. 9, pp. 2277-2289, 2016.

[29] C. Berger et al., "Ultrathin epitaxial graphite: 2D electron gas properties and a route toward graphene-based nanoelectronics," The Journal of Physical Chemistry B, vol. 108, no. 52, pp. 19912-19916, 2004.

[30] E. Hwang, R. Sensarma, and S. D. Sarma, "Plasmon-phonon coupling in graphene," Physical Review B, vol. 82, no. 19, p. 195406, 2010.

[31] K. Li et al., "Graphene Plasmon Cavities Made with Silicon Carbide," ACS Omega, vol. 2, no. 7, pp. 3640-3646, 2017.

[32] X. Xiao, X. Li, J. D. Caldwell, S. A. Maier, and V. Giannini, "Theoretical analysis of graphene plasmon cavities," Applied Materials Today, vol. 12, pp. 283-293, 2018.

[33] F. Iacopi et al., "A catalytic alloy approach for graphene on epitaxial SiC on silicon wafers," Journal of Materials Research, vol. 30, no. 5, pp. 609-616, 2015.

[34] A. Pradeepkumar et al., "p-Type Epitaxial Graphene on Cubic Silicon Carbide on Silicon for Integrated Silicon Technologies," ACS Applied Nano Materials, vol. 3, no. 1, pp. 830-841, 2019.

[35] N. Mishra et al., "Solid source growth of graphene with Ni–Cu catalysts: towards high quality in situ graphene on silicon," Journal of Physics D: Applied Physics, vol. 50, no. 9, p. 095302, 2017.

[36] N. Mishra, M. Bosi, F. Rossi, G. Salviati, J. Boeckl, and F. Iacopi, "Growth of graphitic carbon layers around silicon carbide nanowires," Journal of Applied Physics, vol. 126, no. 6, p. 065304, 2019.

[37] B. V. Cunning, M. Ahmed, N. Mishra, A. R. Kermany, B. Wood, and F. Iacopi, "Graphitized silicon carbide microbeams: wafer-level, self-aligned graphene on silicon wafers," Nanotechnology, vol. 25, no. 32, p. 325301, 2014.

[38] V. C. Coffey, "Seeing in the dark: Defense applications of IR imaging," Optics and Photonics News, vol. 22, no. 4, pp. 26-31, 2011.

[39] X. Wang, Z. Cheng, K. Xu, H. K. Tsang, and J.-B. Xu, "High-responsivity graphene/silicon-heterostructure waveguide photodetectors," Nature Photonics, vol. 7, no. 11, pp. 888-891, 2013.

[40] A. N. Grigorenko, M. Polini, and K. Novoselov, "Graphene plasmonics," Nature photonics, vol. 6, no. 11, pp. 749-758, 2012.

[41] J. T. Kim and S.-Y. Choi, "Graphene-based plasmonic waveguides for photonic integrated circuits," Optics express, vol. 19, no. 24, pp. 24557-24562, 2011.

[42] M. Liu and X. Zhang, "Graphene benefits," Nature Photonics, vol. 7, no. 11, pp. 851-852, 2013.

[43] B. Wang, X. Zhang, F. J. García-Vidal, X. Yuan, and J. Teng, "Strong coupling of surface plasmon polaritons in monolayer graphene sheet arrays," Physical Review Letters, vol. 109, no. 7, p. 073901, 2012.

[44] S. A. Maier, Plasmonics: fundamentals and applications. New York, U. S. A: Springer Science & Business Media, 2007.

[45] S. Bhadra and A. Ghatak, Guided Wave Optics and Photonic Devices. CRC Press, 2016.

[46] H. Raether, "Surface plasmons on smooth surfaces," in Surface plasmons on smooth and rough surfaces and on gratings: Springer, 1988, pp. 4-39.

[47] W. L. Barnes, "Surface plasmon–polariton length scales: a route to sub-wavelength optics," Journal of optics A: pure and applied optics, vol. 8, no. 4, p. S87, 2006.

[48] G. Goubau, "Surface waves and their application to transmission lines," Journal of Applied Physics, vol. 21, no. 11, pp. 1119-1128, 1950.

[49] H. Högström, S. Valizadeh, and C. G. Ribbing, "Optical excitation of surface phonon polaritons in silicon carbide by a hole array fabricated by a focused ion beam," Optical Materials, vol. 30, no. 2, pp. 328-333, 2007.

[50] D. Sarid and W. A. Challener, Modern introduction to surface plasmons: theory, Mathematica modeling, and applications. Cambridge University Press, 2010.

[51] A. A. Maradudin, J. R. Sambles, and W. L. Barnes, Modern plasmonics. Elsevier, 2014.

[52] W. L. Barnes, A. Dereux, and T. W. Ebbesen, "Surface plasmon subwavelength optics," nature, vol. 424, no. 6950, p. 824, 2003.

[53] E. Kretschmann and H. Raether, "Radiative decay of non radiative surface plasmons excited by light," Zeitschrift für Naturforschung A, vol. 23, no. 12, pp. 2135-2136, 1968.

[54] H. Ditlbacher et al., "Fluorescence imaging of surface plasmon fields," Applied physics letters, vol. 80, no. 3, pp. 404-406, 2002.

[55] H. Ditlbacher, J. R. Krenn, G. Schider, A. Leitner, and F. R. Aussenegg, "Two-dimensional optics with surface plasmon polaritons," Applied Physics Letters, vol. 81, no. 10, pp. 1762-1764, 2002.

[56] S. Kawata, M. Ohtsu, and M. Irie, Near-field optics and surface plasmon polaritons. Springer Science & Business Media, 2001.

[57] A. Otto, "Excitation of nonradiative surface plasma waves in silver by the method of frustrated total reflection," Zeitschrift für Physik A Hadrons and nuclei, vol. 216, no. 4, pp. 398-410, 1968.

[58] S. Pechprasarn, S. Learkthanakhachon, G. Zheng, H. Shen, D. Y. Lei, and M. G. Somekh, "Grating-coupled Otto configuration for hybridized surface phonon polariton excitation for local refractive index sensitivity enhancement," Optics express, vol. 24, no. 17, pp. 19517-19530, 2016.

[59] E. Kretschmann, "The angular dependence and the polarisation of light emitted by surface plasmons on metals due to roughness," Optics Communications, vol. 5, no. 5, pp. 331-336, 1972.

[60] E. Kretschmann, "Decay of non radiative surface plasmons into light on rough silver films. Comparison of experimental and theoretical results," Optics Communications, vol. 6, no. 2, pp. 185-187, 1972.

[61] A. C. Neto, F. Guinea, N. M. Peres, K. S. Novoselov, and A. K. Geim, "The electronic properties of graphene," Reviews of modern physics, vol. 81, no. 1, p. 109, 2009.

[62] K. S. Novoselov et al., "Two-dimensional gas of massless Dirac fermions in graphene," nature, vol. 438, no. 7065, p. 197, 2005.

[63] H. Petroski, The pencil: A history of design and circumstance. Alfred a Knopf Incorporated, 1992.

[64] K. S. Novoselov et al., "Electric field effect in atomically thin carbon films," science, vol. 306, no. 5696, pp. 666-669, 2004.

[65] P. Phillips, "Mottness," Annals of Physics, vol. 321, no. 7, pp. 1634-1650, 2006.

[66] M. Jablan, M. Soljačić, and H. Buljan, "Plasmons in graphene: fundamental properties and potential applications," Proceedings of the IEEE, vol. 101, no. 7, pp. 1689-1704, 2013.

[67] K. F. Mak, M. Y. Sfeir, Y. Wu, C. H. Lui, J. A. Misewich, and T. F. Heinz, "Measurement of the optical conductivity of graphene," Physical review letters, vol. 101, no. 19, p. 196405, 2008.

[68] K. Ziegler, "Minimal conductivity of graphene: Nonuniversal values from the Kubo formula," Physical Review B, vol. 75, no. 23, p. 233407, 2007.

[69] R. Alaee, M. Farhat, C. Rockstuhl, and F. Lederer, "A perfect absorber made of a graphene micro-ribbon metamaterial," Optics express, vol. 20, no. 27, pp. 28017-28024, 2012.

[70] G. W. Hanson, "Quasi-transverse electromagnetic modes supported by a graphene parallel-plate waveguide," Journal of Applied Physics, vol. 104, no. 8, p. 084314, 2008.

[71] Y. Francescato, V. Giannini, and S. A. Maier, "Strongly confined gap plasmon modes in graphene sandwiches and graphene-on-silicon," New Journal of Physics, vol. 15, no. 6, p. 063020, 2013.

[72] X. Luo, T. Qiu, W. Lu, and Z. Ni, "Plasmons in graphene: recent progress and applications," Materials Science and Engineering: R: Reports, vol. 74, no. 11, pp. 351-376, 2013.

[73] A. Vakil and N. Engheta, "Transformation optics using graphene," Science, vol. 332, no. 6035, pp. 1291-1294, 2011.

[74] M. Jablan, H. Buljan, and M. Soljačić, "Plasmonics in graphene at infrared frequencies," Physical review B, vol. 80, no. 24, p. 245435, 2009.

[75] E. L. Runnerstrom, K. P. Kelley, E. Sachet, C. T. Shelton, and J.-P. Maria, "Epsilon-near-zero modes and surface plasmon resonance in fluorine-doped cadmium oxide thin films," ACS Photonics, vol. 4, no. 8, pp. 1885-1892, 2017.

[76] S. Campione, I. Brener, and F. Marquier, "Theory of epsilon-near-zero modes in ultrathin films," Physical Review B, vol. 91, no. 12, p. 121408, 2015.

[77] S. Vassant, J.-P. Hugonin, F. Marquier, and J.-J. Greffet, "Berreman mode and epsilon near zero mode," Optics express, vol. 20, no. 21, pp. 23971-23977, 2012.

[78] B. Dastmalchi, P. Tassin, T. Koschny, and C. M. Soukoulis, "A new perspective on plasmonics: confinement and propagation length of surface plasmons for different materials and geometries," Advanced Optical Materials, vol. 4, no. 1, pp. 177-184, 2016.

[79] J. Chen et al., "Optical nano-imaging of gate-tunable graphene plasmons," Nature, vol. 487, no. 7405, p. 77, 2012.

[80] Q. Guo, C. Li, B. Deng, S. Yuan, F. Guinea, and F. Xia, "Infrared nanophotonics based on graphene plasmonics," ACS Photonics, vol. 4, no. 12, pp. 2989-2999, 2017.

[81] Y. Fan et al., "Tunable mid-infrared coherent perfect absorption in a graphene meta-surface," Scientific reports, vol. 5, p. 13956, 2015.

[82] S. Adachi, Optical properties of crystalline and amorphous semiconductors: Materials and fundamental principles. New York, U. S. A: Springer Science & Business Media, 2012.

[83] C. F. Bohren and D. R. Huffman, Absorption and scattering of light by small particles. John Wiley & Sons, 2008.

[84] J. D. Caldwell et al., "Low-loss, extreme subdiffraction photon confinement via silicon carbide localized surface phonon polariton resonators," Nano letters, vol. 13, no. 8, pp. 3690-3697, 2013.

[85] I. J. Luxmoore et al., "Strong coupling in the far-infrared between graphene plasmons and the surface optical phonons of silicon dioxide," ACS photonics, vol. 1, no. 11, pp. 1151-1155, 2014.

[86] A. Mooradian and G. Wright, "Observation of the interaction of plasmons with longitudinal optical phonons in GaAs," Physical Review Letters, vol. 16, no. 22, p. 999, 1966.

[87] C. García Núñez et al., "Surface optical phonons in GaAs nanowires grown by Ga-assisted chemical beam epitaxy," Journal of Applied Physics, vol. 115, no. 3, p. 034307, 2014.

[88] H. Nienhaus, T. Kampen, and W. Mönch, "Phonons in 3C-, 4H-, and 6H-SiC," Surface science, vol. 324, no. 1, pp. L328-L332, 1995.

[89] S. Dai et al., "Phonon Polaritons in Monolayers of Hexagonal Boron Nitride," Advanced Materials, vol. 31, no. 37, p. 1806603, 2019.

[90] A. Fali et al., "Refractive Index-Based Control of Hyperbolic Phonon-Polariton Propagation," Nano letters, vol. 19, no. 11, pp. 7725-7734, 2019.

[91] I. Chatzakis et al., "Strong confinement of optical fields using localized surface phonon polaritons in cubic boron nitride," Optics letters, vol. 43, no. 9, pp. 2177-2180, 2018.

[92] J. D. Caldwell et al., "Sub-diffractional volume-confined polaritons in the natural hyperbolic material hexagonal boron nitride," Nature communications, vol. 5, p. 5221, 2014.

[93] M. Tamagnone et al., "Ultra-confined mid-infrared resonant phonon polaritons in van der Waals nanostructures," Science advances, vol. 4, no. 6, p. eaat7189, 2018.

[94] I.-H. Lee et al., "Pushing the polariton confinement limits with low losses using image polaritons in boron nitride," arXiv preprint arXiv:2001.10583, 2020.

[95] I. Razdolski et al., "Resonant enhancement of second-harmonic generation in the mid-infrared using localized surface phonon polaritons in subdiffractional nanostructures," Nano letters, vol. 16, no. 11, pp. 6954-6959, 2016.

[96] K. Feng, W. Streyer, Y. Zhong, A. Hoffman, and D. Wasserman, "Photonic materials, structures and devices for Reststrahlen optics," Optics Express, vol. 23, no. 24, pp. A1418-A1433, 2015.

[97] Z. Li and N. Yu, "Modulation of mid-infrared light using graphene-metal plasmonic antennas," Applied Physics Letters, vol. 102, no. 13, p. 131108, 2013.

[98] K. I. Bolotin et al., "Ultrahigh electron mobility in suspended graphene," Solid State Communications, vol. 146, no. 9-10, pp. 351-355, 2008.

[99] A. Woessner et al., "Highly confined low-loss plasmons in graphene–boron nitride heterostructures," Nature materials, vol. 14, no. 4, pp. 421-425, 2015.

[100] A. Ouerghi et al., "Epitaxial graphene on 3C-SiC (111) pseudosubstrate: Structural and electronic properties," Physical Review B, vol. 82, no. 12, p. 125445, 2010.

[101] M. Radulaski et al., "Photonic crystal cavities in cubic (3C) polytype silicon carbide films," Optics express, vol. 21, no. 26, pp. 32623-32629, 2013.

[102] B.-S. Song, S. Yamada, T. Asano, and S. Noda, "Demonstration of two-dimensional photonic crystals based on silicon carbide," Optics express, vol. 19, no. 12, pp. 11084-11089, 2011.

[103] R. Koch, T. Seyller, and J. Schaefer, "Strong phonon-plasmon coupled modes in the graphene/silicon carbide heterosystem," Physical Review B, vol. 82, no. 20, p. 201413, 2010.

[104] W. B. Lu, W. Zhu, H. J. Xu, Z. H. Ni, Z. G. Dong, and T. J. Cui, "Flexible transformation plasmonics using graphene," Optics express, vol. 21, no. 9, pp. 10475-10482, 2013.

[105] S. Xiao, X. Zhu, B.-H. Li, and N. A. Mortensen, "Graphene-plasmon polaritons: From fundamental properties to potential applications," Frontiers of Physics, vol. 11, no. 2, p. 117801, 2016.

[106] Y. Wang, H. Liu, S. Wang, M. Cai, and L. Ma, "Optical transport properties of graphene surface plasmon polaritons in Mid-Infrared band," Crystals, vol. 9, no. 7, p. 354, 2019.

[107] J. B. Khurgin, "How to deal with the loss in plasmonics and metamaterials," Nature nanotechnology, vol. 10, no. 1, p. 2, 2015.

[108] J. D. Caldwell, I. Vurgaftman, J. G. Tischler, O. J. Glembocki, J. C. Owrutsky, and T. L. Reinecke, "Atomic-scale photonic hybrids for mid-infrared and terahertz nanophotonics," Nature nanotechnology, vol. 11, no. 1, p. 9, 2016.

[109] A. Pradeepkumar et al., "p-type Epitaxial Graphene on Cubic Silicon Carbide on Silicon for Integrated Silicon Technologies," ACS Applied Nano Materials, 2019.

[110] H. Boehm, A. Clauss, G. Fischer, and U. Hofmann, "Surface properties of extremely thin graphite lamellae," in Proceedings of the fifth conference on carbon, 1962, vol. 1, pp. 73-80: Pergamon Press New York.

[111] H. Boehm, R. Setton, and E. Stumpp, "Nomenclature and terminology of graphite intercalation compounds," ed: Pergamon, 1986.

[112] S. Bae et al., "Roll-to-roll production of 30-inch graphene films for transparent electrodes," Nature nanotechnology, vol. 5, no. 8, p. 574, 2010.

[113] M. H. Rümmeli et al., "On the role of vapor trapping for chemical vapor deposition (CVD) grown graphene over copper," Chemistry of Materials, vol. 25, no. 24, pp. 4861-4866, 2013.

[114] M. H. Rummeli et al., "Direct low-temperature nanographene CVD synthesis over a dielectric insulator," ACS nano, vol. 4, no. 7, pp. 4206-4210, 2010.

[115] L. Jiao, L. Zhang, X. Wang, G. Diankov, and H. Dai, "Narrow graphene nanoribbons from carbon nanotubes," Nature, vol. 458, no. 7240, p. 877, 2009.

[116] M. Choucair, P. Thordarson, and J. A. Stride, "Gram-scale production of graphene based on solvothermal synthesis and sonication," Nature nanotechnology, vol. 4, no. 1, p. 30, 2009.

[117] W. A. De Heer et al., "Large area and structured epitaxial graphene produced by confinement controlled sublimation of silicon carbide," Proceedings of the National Academy of Sciences, vol. 108, no. 41, pp. 16900-16905, 2011.

[118] K. V. Emtsev et al., "Towards wafer-size graphene layers by atmospheric pressure graphitization of silicon carbide," Nature materials, vol. 8, no. 3, pp. 203-207, 2009.

[119] J.-H. Chen, C. Jang, S. Adam, M. Fuhrer, E. D. Williams, and M. Ishigami, "Charged-impurity scattering in graphene," Nature physics, vol. 4, no. 5, pp. 377-381, 2008.

[120] J.-H. Chen, C. Jang, S. Xiao, M. Ishigami, and M. S. Fuhrer, "Intrinsic and extrinsic performance limits of graphene devices on SiO 2," Nature nanotechnology, vol. 3, no. 4, pp. 206-209, 2008.

[121] Y. Zhang, L. Zhang, and C. Zhou, "Review of chemical vapor deposition of graphene and related applications," Accounts of chemical research, vol. 46, no. 10, pp. 2329-2339, 2013.

[122] Q. Yu, J. Lian, S. Siriponglert, H. Li, Y. P. Chen, and S.-S. Pei, "Graphene segregated on Ni surfaces and transferred to insulators," Applied Physics Letters, vol. 93, no. 11, p. 113103, 2008.

[123] J. Coraux et al., "Growth of graphene on Ir (111)," New Journal of Physics, vol. 11, no. 2, p. 023006, 2009.

[124] X. Li, W. Cai, L. Colombo, and R. S. Ruoff, "Evolution of graphene growth on Ni and Cu by carbon isotope labeling," Nano letters, vol. 9, no. 12, pp. 4268-4272, 2009.

[125] H. Ago et al., "Epitaxial chemical vapor deposition growth of single-layer graphene over cobalt film crystallized on sapphire," Acs Nano, vol. 4, no. 12, pp. 7407-7414, 2010.

[126] N. Petrone et al., "Chemical vapor deposition-derived graphene with electrical performance of exfoliated graphene," Nano letters, vol. 12, no. 6, pp. 2751-2756, 2012.

[127] X. Ding, G. Ding, X. Xie, F. Huang, and M. Jiang, "Direct growth of few layer graphene on hexagonal boron nitride by chemical vapor deposition," Carbon, vol. 49, no. 7, pp. 2522-2525, 2011.

[128] H. Bi, S. Sun, F. Huang, X. Xie, and M. Jiang, "Direct growth of few-layer graphene films on SiO 2 substrates and their photovoltaic applications," Journal of Materials Chemistry, vol. 22, no. 2, pp. 411-416, 2012.

[129] L. Zhang, Z. Shi, Y. Wang, R. Yang, D. Shi, and G. Zhang, "Catalyst-free growth of nanographene films on various substrates," Nano Research, vol. 4, no. 3, pp. 315-321, 2011.

[130] A. Khan et al., "Direct CVD growth of graphene on technologically important dielectric and semiconducting substrates," Advanced Science, vol. 5, no. 11, p. 1800050, 2018.

[131] B. Gupta, M. Notarianni, N. Mishra, M. Shafiei, F. Iacopi, and N. Motta, "Evolution of epitaxial graphene layers on 3C SiC/Si (1 1 1) as a function of annealing temperature in UHV," Carbon, vol. 68, pp. 563-572, 2014.

[132] T. Seyller et al., "Epitaxial graphene: a new material," physica status solidi (b), vol. 245, no. 7, pp. 1436-1446, 2008.

[133] D. Badami, "X-ray studies of graphite formed by decomposing silicon carbide," Carbon, vol. 3, no. 1, pp. 53-57, 1965.

[134] A. Van Bommel, J. Crombeen, and A. Van Tooren, "LEED and Auger electron observations of the SiC (0001) surface," Surface Science, vol. 48, no. 2, pp. 463-472, 1975.

[135] C. Berger et al., "Electronic confinement and coherence in patterned epitaxial graphene," Science, vol. 312, no. 5777, pp. 1191-1196, 2006.

[136] J. Hass et al., "Highly ordered graphene for two dimensional electronics," Applied Physics Letters, vol. 89, no. 14, p. 143106, 2006.

[137] H. Hibino, H. Kageshima, F. Maeda, M. Nagase, Y. Kobayashi, and H. Yamaguchi, "Microscopic thickness determination of thin graphite films formed on SiC from quantized oscillation in reflectivity of low-energy electrons," Physical Review B, vol. 77, no. 7, p. 075413, 2008.

[138] I. Langmuir, "Convection and conduction of heat in gases," Physical Review (Series I), vol. 34, no. 6, p. 401, 1912.

[139] G. R. Yazdi, R. Vasiliauskas, T. Iakimov, A. Zakharov, M. Syväjärvi, and R. Yakimova, "Growth of large area monolayer graphene on 3C-SiC and a comparison with other SiC polytypes," Carbon, vol. 57, pp. 477-484, 2013.

[140] R. Tromp and J. Hannon, "Thermodynamics and kinetics of graphene growth on SiC (0001)," Physical review letters, vol. 102, no. 10, p. 106104, 2009.

[141] B. Gupta, E. Placidi, C. Hogan, N. Mishra, F. Iacopi, and N. Motta, "The transition from 3C SiC (1 1 1) to graphene captured by Ultra High Vacuum Scanning Tunneling Microscopy," Carbon, vol. 91, pp. 378-385, 2015.

[142] M. Suemitsu and H. Fukidome, "Epitaxial graphene on silicon substrates," Journal of Physics D: Applied Physics, vol. 43, no. 37, p. 374012, 2010.

[143] A. Ouerghi et al., "Epitaxial graphene on cubic SiC (111)/Si (111) substrate," Applied physics letters, vol. 96, no. 19, p. 191910, 2010.

[144] A. Ouerghi et al., "Epitaxial graphene on single domain 3C-SiC (100) thin films grown on off-axis Si (100)," Applied physics letters, vol. 101, no. 2, p. 021603, 2012.

[145] H. Fukidome et al., "Controls over structural and electronic properties of epitaxial graphene on silicon using surface termination of 3C-SiC (111)/Si," Applied Physics Express, vol. 4, no. 11, p. 115104, 2011.

[146] M. Suemitsu, Y. Miyamoto, H. Handa, and A. Konno, "Graphene formation on a 3C-SiC (111) thin film grown on Si (110) substrate," e-Journal of Surface Science and Nanotechnology, vol. 7, pp. 311-313, 2009.

[147] H. Fukidome et al., "Site-selective epitaxy of graphene on Si wafers," Proceedings of the IEEE, vol. 101, no. 7, pp. 1557-1566, 2013.

[148] A. Ouerghi et al., "Sharp interface in epitaxial graphene layers on 3 C-SiC (100)/Si (100) wafers," Physical Review B, vol. 83, no. 20, p. 205429, 2011.

[149] Y. Zhang et al., "Direct observation of a widely tunable bandgap in bilayer graphene," Nature, vol. 459, no. 7248, pp. 820-823, 2009.

[150] M. Fanton, J. Robinson, B. Weiland, and J. Moon, "3C-SiC films grown on Si (111) substrates as a template for graphene epitaxy," ECS Transactions, vol. 19, no. 5, p. 131, 2009.

[151] P. Pirouz, C. Chorey, and J. Powell, "Antiphase boundaries in epitaxially grown β-SiC," Applied physics letters, vol. 50, no. 4, pp. 221-223, 1987.

[152] H. Deng and K. Yamamura, "Smoothing of reaction sintered silicon carbide using plasma assisted polishing," Current Applied Physics, vol. 12, pp. S24-S28, 2012.

[153] N. Mishra, L. Hold, A. Iacopi, B. Gupta, N. Motta, and F. Iacopi, "Controlling the surface roughness of epitaxial SiC on silicon," Journal of Applied Physics, vol. 115, no. 20, p. 203501, 2014.

[154] A. A. Yasseen, C. A. Zorman, and M. Mehregany, "Roughness Reduction of 3C-SiC Surfaces Using SiC-Based Mechanical Polishing Slurries," Journal of the Electrochemical Society, vol. 146, no. 1, p. 327, 1999.

[155] B. Julies, D. Knoesen, R. Pretorius, and D. Adams, "A study of the NiSi to NiSi2 transition in the Ni–Si binary system," Thin Solid Films, vol. 347, no. 1-2, pp. 201-207, 1999.

[156] L. E. F. Torres, S. Roche, and J.-C. Charlier, Introduction to graphene-based nanomaterials: from electronic structure to quantum transport. Cambridge University Press, 2020.

[157] Q. Guo et al., "Efficient electrical detection of mid-infrared graphene plasmons at room temperature," Nature materials, vol. 17, no. 11, pp. 986-992, 2018.

[158] R.-J. Shiue et al., "Thermal radiation control from hot graphene electrons coupled to a photonic crystal nanocavity," Nature communications, vol. 10, no. 1, pp. 1-7, 2019.

[159] S. Chakraborty, O. Marshall, T. Folland, Y.-J. Kim, A. Grigorenko, and K. Novoselov, "Gain modulation by graphene plasmons in aperiodic lattice lasers," Science, vol. 351, no. 6270, pp. 246-248, 2016.

[160] M. B. Lundeberg et al., "Tuning quantum nonlocal effects in graphene plasmonics," Science, vol. 357, no. 6347, pp. 187-191, 2017.

[161] G. Ni et al., "Fundamental limits to graphene plasmonics," Nature, vol. 557, no. 7706, pp. 530-533, 2018.

[162] L. Yu, J. Zheng, Y. Xu, D. Dai, and S. He, "Local and nonlocal optically induced transparency effects in graphene–silicon hybrid nanophotonic integrated circuits," ACS nano, vol. 8, no. 11, pp. 11386-11393, 2014.

[163] I. Silveiro, J. M. P. Ortega, and F. J. G. De Abajo, "Quantum nonlocal effects in individual and interacting graphene nanoribbons," Light: Science & Applications, vol. 4, no. 1, pp. e241-e241, 2015.

[164] S. Sunku et al., "Photonic crystals for nano-light in moiré graphene superlattices," Science, vol. 362, no. 6419, pp. 1153-1156, 2018.

[165] V. Ryzhii and M. Ryzhii, "Graphene bilayer field-effect phototransistor for terahertz and infrared detection," Physical Review B, vol. 79, no. 24, p. 245311, 2009.

[166] L. Ju et al., "Tunable excitons in bilayer graphene," Science, vol. 358, no. 6365, pp. 907-910, 2017.

[167] K. I. Bolotin et al., "Ultrahigh electron mobility in suspended graphene," Solid State Communications, vol. 146, no. 9-10, pp. 351-355, 2008.

[168] D. K. Efetov and P. Kim, "Controlling electron-phonon interactions in graphene at ultrahigh carrier densities," Physical review letters, vol. 105, no. 25, p. 256805, 2010.

[169] Y. Yao et al., "Electrically tunable metasurface perfect absorbers for ultrathin mid-infrared optical modulators," Nano letters, vol. 14, no. 11, pp. 6526-6532, 2014.

[170] N. K. Emani, T.-F. Chung, A. V. Kildishev, V. M. Shalaev, Y. P. Chen, and A. Boltasseva, "Electrical modulation of fano resonance in plasmonic nanostructures using graphene," Nano letters, vol. 14, no. 1, pp. 78-82, 2013.

[171] B. Sensale-Rodriguez et al., "Broadband graphene terahertz modulators enabled by intraband transitions," Nature communications, vol. 3, no. 1, pp. 1-7, 2012.

[172] S. H. Lee et al., "Switching terahertz waves with gate-controlled active graphene metamaterials," Nature materials, vol. 11, no. 11, pp. 936-941, 2012.

[173] Q. Zhang, Z. Zhen, Y. Yang, G. Gan, D. Jariwala, and X. Cui, "Hybrid phonon-polaritons at atomically-thin van der Waals heterointerfaces for infrared optical modulation," Optics express, vol. 27, no. 13, pp. 18585-18600, 2019.

[174] J. T. Kim, Y.-J. Yu, H. Choi, and C.-G. Choi, "Graphene-based plasmonic photodetector for photonic integrated circuits," Optics express, vol. 22, no. 1, pp. 803-808, 2014.

[175] X. Wang, Z. Cheng, K. Xu, H. K. Tsang, and J.-B. Xu, "High-responsivity graphene/silicon-heterostructure waveguide photodetectors," Nature Photonics, vol. 7, no. 11, p. 888, 2013.

[176] K. Yang, S. Liu, S. Arezoomandan, A. Nahata, and B. Sensale-Rodriguez, "Graphene-based tunable metamaterial terahertz filters," Applied Physics Letters, vol. 105, no. 9, p. 093105, 2014.

[177] H.-J. Li et al., "Graphene-based mid-infrared, tunable, electrically controlled plasmonic filter," Applied Physics Express, vol. 7, no. 2, p. 024301, 2014.

[178] J. Moon et al., "Top-gated epitaxial graphene FETs on Si-face SiC wafers with a peak transconductance of 600 mS/mm," IEEE Electron Device Letters, vol. 31, no. 4, pp. 260-262, 2010.

[179] J. Kedzierski et al., "Epitaxial graphene transistors on SiC substrates," IEEE Transactions on Electron Devices, vol. 55, no. 8, pp. 2078-2085, 2008.

[180] J. B. Oostinga, H. B. Heersche, X. Liu, A. F. Morpurgo, and L. M. Vandersypen, "Gate-induced insulating state in bilayer graphene devices," Nature materials, vol. 7, no. 2, p. 151, 2008.

[181] N. Jung, N. Kim, S. Jockusch, N. J. Turro, P. Kim, and L. Brus, "Charge transfer chemical doping of few layer graphenes: charge distribution and band gap formation," Nano letters, vol. 9, no. 12, pp. 4133-4137, 2009.

[182] Y.-J. Yu, Y. Zhao, S. Ryu, L. E. Brus, K. S. Kim, and P. Kim, "Tuning the graphene work function by electric field effect," Nano letters, vol. 9, no. 10, pp. 3430-3434, 2009.

[183] M. Fanton, J. Robinson, B. Weiland, and J. Moon, "3C-SiC films grown on Si (111) substrates as a template for graphene epitaxy," ECS Transactions, vol. 19, no. 5, pp. 131-135, 2009.

[184] X. Song et al., "Microtwin reduction in 3C–SiC heteroepitaxy," Appl. Phys. Lett., vol. 96, no. 14, p. 142104, 2010.

[185] A. Pradeepkumar, M. Zielinski, M. Bosi, G. Verzellesi, D. K. Gaskill, and F. Iacopi, "Electrical leakage phenomenon in heteroepitaxial cubic silicon carbide on silicon," Journal of Applied Physics, vol. 123, no. 21, p. 215103, 2018.

[186] H. Hu et al., "Broadly tunable graphene plasmons using an ion-gel top gate with low control voltage," Nanoscale, vol. 7, no. 46, pp. 19493-19500, 2015.

[187] J. Niu, Y. Jun Shin, Y. Lee, J.-H. Ahn, and H. Yang, "Graphene induced tunability of the surface plasmon resonance," Applied Physics Letters, vol. 100, no. 6, p. 061116, 2012.

[188] J. Kim et al., "Electrical control of optical plasmon resonance with graphene," Nano letters, vol. 12, no. 11, pp. 5598-5602, 2012.

[189] P. Q. Liu et al., "Highly tunable hybrid metamaterials employing split-ring resonators strongly coupled to graphene surface plasmons," Nature communications, vol. 6, p. 8969, 2015.

[190] M. Freitag, T. Low, W. Zhu, H. Yan, F. Xia, and P. Avouris, "Photocurrent in graphene harnessed by tunable intrinsic plasmons," Nature communications, vol. 4, p. 1951, 2013.

[191] Y. Liu, R. Zhong, Z. Lian, C. Bu, and S. Liu, "Dynamically tunable band stop filter enabled by the metal-graphene metamaterials," Scientific reports, vol. 8, no. 1, p. 2828, 2018.

[192] C. Shu, Q.-G. Chen, J.-S. Mei, and J.-H. Yin, "Dynamically tunable implementation of electromagnetically induced transparency based on bright and dark modes coupling graphene-nanostrips," Optics Communications, vol. 420, pp. 65-71, 2018.

[193] Z. Fang et al., "Active tunable absorption enhancement with graphene nanodisk arrays," Nano letters, vol. 14, no. 1, pp. 299-304, 2013.

[194] M. M. Jadidi et al., "Tunable terahertz hybrid metal–graphene plasmons," Nano letters, vol. 15, no. 10, pp. 7099-7104, 2015.

[195] H. Yan, Z. Li, X. Li, W. Zhu, P. Avouris, and F. Xia, "Infrared spectroscopy of tunable Dirac terahertz magneto-plasmons in graphene," Nano letters, vol. 12, no. 7, pp. 3766-3771, 2012.

[196] N. K. Emani, T.-F. Chung, X. Ni, A. V. Kildishev, Y. P. Chen, and A. Boltasseva, "Electrically tunable damping of plasmonic resonances with graphene," Nano letters, vol. 12, no. 10, pp. 5202-5206, 2012.

[197] Z. Fang et al., "Gated tunability and hybridization of localized plasmons in nanostructured graphene," ACS nano, vol. 7, no. 3, pp. 2388-2395, 2013.

[198] A. Kumar, T. Low, K. H. Fung, P. Avouris, and N. X. Fang, "Tunable light–matter interaction and the role of hyperbolicity in graphene–hBN system," Nano letters, vol. 15, no. 5, pp. 3172-3180, 2015.

[199] Z. Fang et al., "Active tunable absorption enhancement with graphene nanodisk arrays," Nano letters, vol. 14, no. 1, pp. 299-304, 2014.

[200] H. Yan et al., "Tunable infrared plasmonic devices using graphene/insulator stacks," Nature nanotechnology, vol. 7, no. 5, pp. 330-334, 2012.

[201] L. Patrick and W. Choyke, "Localized vibrational modes of a persistent defect in ion-implanted SiC," Journal of Physics and Chemistry of Solids, vol. 34, no. 3, pp. 565-567, 1973.

[202] C. R. Gubbin, F. Martini, A. Politi, S. A. Maier, and S. De Liberato, "Strong and coherent coupling between localized and propagating phonon polaritons," Physical review letters, vol. 116, no. 24, p. 246402, 2016.

[203] Y. Chen et al., "Spectral tuning of localized surface phonon polariton resonators for low-loss mid-IR applications," Acs Photonics, vol. 1, no. 8, pp. 718-724, 2014.

[204] A. Huber, N. Ocelic, T. Taubner, and R. Hillenbrand, "Nanoscale Resolved Infrared Probing of Crystal Structure and of Plasmon− Phonon Coupling," Nano letters, vol. 6, no. 4, pp. 774-778, 2006.

[205] T. Taubner, D. Korobkin, Y. Urzhumov, G. Shvets, and R. Hillenbrand, "Near-field microscopy through a SiC superlens," Science, vol. 313, no. 5793, pp. 1595-1595, 2006.

[206] J. A. Schuller, R. Zia, T. Taubner, and M. L. Brongersma, "Dielectric metamaterials based on electric and magnetic resonances of silicon carbide particles," Physical review letters, vol. 99, no. 10, p. 107401, 2007.

[207] M. Radulaski et al., "Visible photoluminescence from cubic (3C) silicon carbide microdisks coupled to high quality whispering gallery modes," ACS photonics, vol. 2, no. 1, pp. 14-19, 2014.

[208] I. A. Khramtsov, A. A. Vyshnevyy, and D. Y. Fedyanin, "Enhancing the brightness of electrically driven single-photon sources using color centers in silicon carbide," npj Quantum Information, vol. 4, no. 1, 2018.

[209] N. C. Passler et al., "Strong coupling of epsilon-near-zero phonon polaritons in polar dielectric heterostructures," Nano letters, vol. 18, no. 7, pp. 4285-4292, 2018.

[210] K. Pufahl, N. C. Passler, N. B. Grosse, M. Wolf, U. Woggon, and A. Paarmann, "Controlling nanoscale air-gaps for critically coupled surface polaritons by means of non-invasive white-light interferometry," Applied Physics Letters, vol. 113, no. 16, p. 161103, 2018.

[211] N. C. Passler, I. Razdolski, S. Gewinner, W. Schöllkopf, M. Wolf, and A. Paarmann, "Second-harmonic generation from critically coupled surface phonon polaritons," ACS Photonics, vol. 4, no. 5, pp. 1048-1053, 2017.

[212] C. R. Gubbin et al., "Hybrid longitudinal-transverse phonon polaritons," Nature communications, vol. 10, 2019.

[213] C. R. Gubbin, S. A. Maier, and S. De Liberato, "Theoretical investigation of phonon polaritons in SiC micropillar resonators," Physical review B, vol. 95, no. 3, p. 035313, 2017.

[214] D. Feldman, J. H. Parker Jr, W. Choyke, and L. Patrick, "Raman Scattering in 6 H SiC," Physical Review, vol. 170, no. 3, p. 698, 1968.

[215] D. Feldman, J. H. Parker Jr, W. Choyke, and L. Patrick, "Phonon dispersion curves by raman scattering in SiC, Polytypes 3 C, 4 H, 6 H, 1 5 R, and 2 1 R," Physical Review, vol. 173, no. 3, p. 787, 1968.

[216] H. Harima, S. i. Nakashima, and T. Uemura, "Raman scattering from anisotropic LO-phonon–plasmon–coupled mode in n-type 4H–and 6H–SiC," Journal of applied physics, vol. 78, no. 3, pp. 1996-2005, 1995.

[217] T. E. Tiwald et al., "Carrier concentration and lattice absorption in bulk and epitaxial silicon carbide determined using infrared ellipsometry," Physical Review B, vol. 60, no. 16, p. 11464, 1999.

[218] R. Hillenbrand, T. Taubner, and F. Keilmann, "Phonon-enhanced light–matter interaction at the nanometre scale," Nature, vol. 418, no. 6894, p. 159, 2002.

[219] J.-J. Greffet, R. Carminati, K. Joulain, J.-P. Mulet, S. Mainguy, and Y. Chen, "Coherent emission of light by thermal sources," Nature, vol. 416, no. 6876, pp. 61-64, 2002.

[220] B. Neuner III, D. Korobkin, C. Fietz, D. Carole, G. Ferro, and G. Shvets, "Critically coupled surface phonon-polariton excitation in silicon carbide," Optics letters, vol. 34, no. 17, pp. 2667-2669, 2009.

[221] B. Neuner III, D. Korobkin, C. Fietz, D. Carole, G. Ferro, and G. Shvets, "Midinfrared index sensing of pL-scale analytes based on surface phonon polaritons in silicon carbide," The Journal of Physical Chemistry C, vol. 114, no. 16, pp. 7489-7491, 2010.

[222] J. A. Schuller, T. Taubner, and M. L. Brongersma, "Optical antenna thermal emitters," Nature Photonics, vol. 3, no. 11, p. 658, 2009.

[223] T. Wang, P. Li, B. Hauer, D. N. Chigrin, and T. Taubner, "Optical properties of single infrared resonant circular microcavities for surface phonon polaritons," Nano letters, vol. 13, no. 11, pp. 5051-5055, 2013.

[224] Y. Chen et al., "Spectral Tuning of Localized Surface Phonon Polariton Resonators for Low-Loss Mid-IR Applications," ACS Photonics, vol. 1, no. 8, pp. 718-724, 2014.

[225] J. D. Caldwell et al., "Sub-diffractional volume-confined polaritons in the natural hyperbolic material hexagonal boron nitride," Nature communications, vol. 5, no. 1, pp. 1-9, 2014.

[226] D. G. Lidzey, D. Bradley, M. Skolnick, T. Virgili, S. Walker, and D. Whittaker, "Strong exciton–photon coupling in an organic semiconductor microcavity," Nature, vol. 395, no. 6697, p. 53, 1998.

[227] C. R. Gubbin et al., "Hybrid longitudinal-transverse phonon polaritons," Nature Communications, vol. 10, no. 1, p. 1682, 2019.

[228] T. G. Folland, G. Lu, A. Bruncz, J. R. Nolen, M. Tadjer, and J. D. Caldwell, "Vibrational Coupling to Epsilon-Near-Zero Waveguide Modes," ACS Photonics, vol. 7, no. 3, pp. 614-621, 2020.

[229] A. D. Dunkelberger et al., "Active tuning of surface phonon polariton resonances via carrier photoinjection," Nature Photonics, vol. 12, no. 1, pp. 50-56, 2017.

[230] D. C. Ratchford et al., "Controlling the Infrared Dielectric Function through Atomic-Scale Heterostructures," ACS nano, 2019.

[231] Z. Fei et al., "Infrared nanoscopy of Dirac plasmons at the graphene–SiO2 interface," Nano letters, vol. 11, no. 11, pp. 4701-4705, 2011.

[232] C. N. Santos et al., "Terahertz and mid-infrared reflectance of epitaxial graphene," Scientific reports, vol. 6, p. 24301, 2016.

[233] V. W. Brar et al., "Hybrid surface-phonon-plasmon polariton modes in graphene/monolayer h-BN heterostructures," Nano letters, vol. 14, no. 7, pp. 3876-3880, 2014.

[234] A. K. Geim and K. S. Novoselov, "The rise of graphene," Nature materials, vol. 6, no. 3, p. 183, 2007.

[235] R. Matz and H. Lüth, "Conduction-band surface plasmons in the electron-energy-loss spectrum of GaAs (110)," Physical Review Letters, vol. 46, no. 7, p. 500, 1981.

[236] R. Matz, "R. Matz and H. Lüth, Phys. Rev. Lett. 46, 500 (1981)," Phys. Rev. Lett., vol. 46, p. 500, 1981.

[237] R. Koch et al., "Robust phonon-plasmon coupling in quasifreestanding graphene on silicon carbide," Physical review letters, vol. 116, no. 10, p. 106802, 2016.

[238] W. B. Zimmerman, Multiphysics modeling with finite element methods. World Scientific Publishing Company, 2006.

[239] B. K. Daas and A. Dutta, "Electromagnetic dispersion of surface plasmon polariton at the EG/SiC interface," Journal of Materials Research, vol. 29, no. 21, pp. 2485-2490, 2014.

[240] J. Wang et al., "Perfect absorption and strong magnetic polaritons coupling of graphene-based silicon carbide grating cavity structures," Journal of Physics D: Applied Physics, vol. 52, no. 1, p. 015101, 2018.

[241] T. Langer, H. Pfnür, C. Tegenkamp, S. Forti, K. Emtsev, and U. Starke, "Manipulation of plasmon electron–hole coupling in quasi-free-standing epitaxial graphene layers," New Journal of Physics, vol. 14, no. 10, p. 103045, 2012.

[242] Y. Francescato, "New frequencies and geometries for plasmonics and metamaterials," Imperial College London, 2014.

[243] R. Reichelt, "Scanning Electron Microscopy," in Science of Microscopy, P. W. Hawkes and J. C. H. Spence, Eds. New York, NY: Springer New York, 2007, pp. 133-272.

[244] T. Dieing, O. Hollricher, and J. Toporski, Confocal raman microscopy. Springer, 2011.

[245] S. Pimenta, M. d. J. C. Maciel, A. Miranda, M. F. Cerqueira, P. Alpuim, and J. H. Correia, "Raman Spectroscopy for Tumor Diagnosis in Mammary Tissue," in PHOTOPTICS, 2020, pp. 131-134.

[246] L. Cançado et al., "General equation for the determination of the crystallite size L a of nanographite by Raman spectroscopy," Applied Physics Letters, vol. 88, no. 16, p. 163106, 2006.

[247] B. C. Smith, Fundamentals of Fourier transform infrared spectroscopy. CRC press, 2011.

[248] M. Born and E. Wolf, Principles of optics: electromagnetic theory of propagation, interference and diffraction of light. Elsevier, 2013.

[249] N. Thermo, "Introduction to Fourier transform infrared spectrometry," Thermo Nicolet Corporation: Madison-USA, 2001.

[250] B. A. Rahman and A. Agrawal, Finite element modeling methods for photonics. Artech house, 2013.

[251] K. Stamnes, S.-C. Tsay, W. Wiscombe, and K. Jayaweera, "Numerically stable algorithm for discrete-ordinate-method radiative transfer in multiple scattering and emitting layered media," Applied optics, vol. 27, no. 12, pp. 2502-2509, 1988.

[252] K. S. Kunz and R. J. Luebbers, The finite difference time domain method for electromagnetics. CRC press, 1993.

[253] M. Clemens and T. Weiland, "Discrete electromagnetism with the finite integration technique," Progress In Electromagnetics Research, vol. 32, pp. 65-87, 2001.

[254] J.-M. Jin, The finite element method in electromagnetics. John Wiley & Sons, 2015.

[255] C. Caloz and T. Itoh, Electromagnetic metamaterials: transmission line theory and microwave applications. John Wiley & Sons, 2005.

[256] C. Christopoulos, The transmission-line modeling method: TLM. Oxford University Press, 1995.

[257] A. Hrennikoff, "Solution of problems of elasticity by the framework method," J. appl. Mech., 1941.

[258] O. C. Zienkiewicz and R. L. Taylor, The finite element method for solid and structural mechanics. Elsevier, 2005.

[259] J. N. Reddy and D. K. Gartling, The finite element method in heat transfer and fluid dynamics. CRC press, 2010.

[260] P. P. Silvester and R. L. Ferrari, Finite elements for electrical engineers. Cambridge university press, 1996.

[261] P. P. Silvester and G. Pelosi, Finite Elements for Wave Electromagnetics: Methods and Techniques. Piscataway, NJ: IEEE Press, 1994.

[262] P. Silvester, "Finite element solution of homogeneous waveguide problems," Alta Frequenza, vol. 38, no. 1, pp. 313-317, 1969.

[263] P. Arlett, A. Bahrani, and O. Zienkiewicz, "Application of finite elements to the solution of Helmholtz's equation," in Proceedings of the Institution of Electrical Engineers, 1968, vol. 115, no. 12, pp. 1762-1766: IET.

[264] A. C. Polycarpou, "Introduction to the finite element method in electromagnetics," Synthesis Lectures on Computational Electromagnetics, vol. 1, no. 1, pp. 1-126, 2005.

[265] A. Arca, "The design and optimisation of nanophotonic devices using the Finite Element Method," University of Nottingham UK, 2010.

[266] N. Dediyagala, "Optical Fibre Bragg Grating Analysis Through FEA and its Application to Pressure Sensing," Victoria University, 2019.

[267] R. Garg, Analytical and computational methods in electromagnetics. Artech house, 2008.

[268] M. Tabatabaian, COMSOL5 for Engineers. Stylus Publishing, LLC, 2015.

[269] C. Multiphysics, "RF Module User's Guide," COMSOL Multiphysics, Burlington, MA, vol. 5.3a.

[270] D. B. Davidson, Computational electromagnetics for RF and microwave engineering. Cambridge University Press, 2010.

[271] A. Logg, K.-A. Mardal, and G. Wells, Automated solution of differential equations by the finite element method: The FEniCS book. Springer Science & Business Media, 2012.

[272] O. Schenk and K. Gärtner, "Solving unsymmetric sparse systems of linear equations with PARDISO," Future Generation Computer Systems, vol. 20, no. 3, pp. 475-487, 2004.

[273] C. Multiphysics, "Introduction to COMSOL Multiphysics®," COMSOL Multiphysics, Burlington, MA, accessed Feb, vol. 9, p. 2018, 1998.

[274] V. de La Rubia, J. Zapata, and M. A. Gonzalez, "Finite element analysis of periodic structures without constrained meshes," IEEE transactions on antennas and propagation, vol. 56, no. 9, pp. 3020-3028, 2008.

[275] J. Munn, "https://www.comsol.com/blogs/how-to-numerically-simplify-your-periodic-rf-models/," COMSOL Multiphysics, Burlington, MA, accessed July 23 2021

[276] L. Stark, "Electromagnetic waves in periodic structures," 1952.

[277] L. R. Petersson and J.-M. Jin, "A three-dimensional time-domain finite-element formulation for periodic structures," IEEE transactions on antennas and propagation, vol. 54, no. 1, pp. 12-19, 2006.

[278] N. C. Miller, A. D. Baczewski, J. D. Albrecht, and B. Shanker, "A discontinuous Galerkin time domain framework for periodic structures subject to oblique excitation," IEEE transactions on antennas and propagation, vol. 62, no. 8, pp. 4386-4391, 2014.

[279] W. Frei, "Modeling Metallic Objects in Wave Electromagnetics Problems. https://www.comsol.com/blogs/modeling-metallic-objects-in-wave-electromagnetics-problems/," COMSOL Multiphysics, Burlington, MA, accessed April 05 2021.

[280] G. Eriksson, "Efficient 3D simulation of thin conducting layers of arbitrary thickness," in 2007 IEEE International Symposium on Electromagnetic Compatibility, 2007, pp. 1-6: IEEE.

[281] Y. Liu, Y. Chen, J. Li, T.-c. Hung, and J. Li, "Study of energy absorption on solar cell using metamaterials," Solar energy, vol. 86, no. 5, pp. 1586-1599, 2012.

[282] T. Cadman and D. Sadowski, "Generalized equations for the calculation of absorptance, reflectance, and transmittance of a number of parallel surfaces," Applied optics, vol. 17, no. 4, pp. 531-537, 1978.

[283] D. Barchiesi and A. Otto, "Excitations of surface plasmon polaritons by attenuated total reflection, revisited," Riv. Nuovo Cimento, vol. 36, pp. 173-209, 2013.

[284] J. Yao, Y. Chen, L. Ye, N. Liu, G. Cai, and Q. H. Liu, "Multiple resonant excitations of surface plasmons in a graphene stratified slab by Otto configuration and their independent tuning," Photonics Research, vol. 5, no. 4, pp. 377-384, 2017.

[285] M. Amjadipour, D. Su, and F. Iacopi, "Graphitic-Based Solid-State Supercapacitors: Enabling Redox Reaction by In Situ Electrochemical Treatment," Batteries & Supercaps, vol. 3, no. 7, pp. 569-569, 2020.

[286] T. Nguyen et al., "Terahertz surface plasmon polaritons on freestanding multi-walled carbon nanotube aerogel sheets," Optical Materials Express, vol. 2, no. 6, pp. 782-788, 2012.

[287] A. K. Mishra, S. K. Mishra, and R. K. Verma, "Doped single-wall carbon nanotubes in propagating surface plasmon resonance-based fiber optic refractive index sensing," Plasmonics, vol. 12, no. 6, pp. 1657-1663, 2017.

[288] W. Zhou, X. Zhang, Y. Zhang, C. Tian, and C. Xu, "Strongly coupled exciton-surface plasmon polariton from excited-subband transitions of single-walled carbon nanotubes," Optics express, vol. 25, no. 25, pp. 32142-32149, 2017.

[289] K.-X. Xie, S.-S. Jia, J.-H. Zhang, H. Wang, and Q. Wang, "Amplified fluorescence by carbon nanotube (CNT)-assisted surface plasmon coupled emission (SPCE) and its biosensing application," New Journal of Chemistry, vol. 43, no. 36, pp. 14220-14223, 2019.

[290] X. Luo et al., "Reflection phase shift of one-dimensional plasmon polaritons in carbon nanotubes," Physical Review B, vol. 101, no. 4, p. 041407, 2020.

[291] M. S. Ukhtary and R. Saito, "Surface plasmons in graphene and carbon nanotubes," Carbon, vol. 167, pp. 455-474, 2020.

[292] N. Hartmann, G. Piredda, J. Berthelot, G. r. Colas des Francs, A. Bouhelier, and A. Hartschuh, "Launching propagating surface plasmon polaritons by a single carbon nanotube dipolar emitter," Nano letters, vol. 12, no. 1, pp. 177-181, 2012.

[293] K.-C. Chiu et al., "Strong and broadly tunable plasmon resonances in thick films of aligned carbon nanotubes," Nano letters, vol. 17, no. 9, pp. 5641-5645, 2017.

[294] A. Larin, Y. Sun, and D. Zuev, "Numerical design of Au/Si core-shell nanoparticles," in Journal of Physics: Conference Series, 2018, vol. 1092, no. 1, p. 012074: IOP Publishing.

[295] W. Lv, P. E. Phelan, R. Swaminathan, T. P. Otanicar, and R. A. Taylor, "Multifunctional core-shell nanoparticle suspensions for efficient absorption," Journal of solar energy engineering, vol. 135, no. 2, 2013.

[296] H. Xu, "Multilayered metal core-shell nanostructures for inducing a large and tunable local optical field," Physical review B, vol. 72, no. 7, p. 073405, 2005.

[297] D. Paria, C. Zhang, and I. Barman, "Towards rational design and optimization of near-field enhancement and spectral tunability of hybrid core-shell plasmonic nanoprobes," Scientific reports, vol. 9, no. 1, pp. 1-9, 2019.

[298] W. Wu, M. Wan, P. Gu, Z. Chen, and Z. Wang, "Strong coupling between few molecular excitons and Fano-like cavity plasmon in two-layered dielectric-metal core-shell resonators," Optics express, vol. 25, no. 2, pp. 1495-1504, 2017.

[299] N. G. Khlebtsov, L. Lin, B. N. Khlebtsov, and J. Ye, "Gap-enhanced Raman tags: fabrication, optical properties, and theranostic applications," Theranostics, vol. 10, no. 5, p. 2067, 2020.

[300] J. N'Diaye et al., "One-Step In-Situ Growth of Core–Shell SiC@ Graphene Nanoparticles/Graphene Hybrids by Chemical Vapor Deposition," Advanced Materials Interfaces, vol. 3, no. 8, p. 1500806, 2016.

[301] Z. Chen, M. Zhou, Y. Cao, X. Ai, H. Yang, and J. Liu, "In situ generation of few-layer graphene coatings on SnO2-SiC core-shell nanoparticles for high-performance lithium-ion storage," Advanced Energy Materials, vol. 2, no. 1, pp. 95-102, 2012.

[302] S. Bhardwaj, R. Uma, and R. Sharma, "A study of metal@ graphene core–shell spherical nano-geometry to enhance the SPR tunability: influence of graphene monolayer shell thickness," Plasmonics, vol. 12, no. 4, pp. 961-969, 2017.

[303] Y. Li, X. He, M. Wan, W. Wu, and Z. Chen, "Unconventional Fano effect based spectrally selective absorption enhancement in graphene using plasmonic core-shell nanostructures," Applied Physics Letters, vol. 109, no. 3, p. 031909, 2016.

[304] T. Christensen, A.-P. Jauho, M. Wubs, and N. A. Mortensen, "Localized plasmons in graphene-coated nanospheres," Physical Review B, vol. 91, no. 12, p. 125414, 2015.

[305] J. Song, Q. Cheng, Z. Luo, X. Zhou, and Z. Zhang, "Modulation and splitting of three-body radiative heat flux via graphene/SiC core-shell nanoparticles," International Journal of Heat and Mass Transfer, vol. 140, pp. 80-87, 2019.

[306] F. A. Memon, F. Morichetti, and A. Melloni, "Silicon Oxycarbide Waveguides for Photonic Applications," in Journal of Physics: Conference Series, 2018, vol. 961, no. 1, p. 012014: IOP Publishing.

[307] D. Tzarouchis and A. Sihvola, "Light scattering by a dielectric sphere: perspectives on the Mie resonances," Applied Sciences, vol. 8, no. 2, p. 184, 2018.

[308] S. H. Raad and Z. Atlasbaf, "Equivalent RLC ladder circuit for scattering by graphene-coated nanospheres," IEEE Transactions on Nanotechnology, vol. 18, pp. 212-219, 2019.

[309] I.-H. Lee, D. Yoo, P. Avouris, T. Low, and S.-H. Oh, "Graphene acoustic plasmon resonator for ultrasensitive infrared spectroscopy," Nature nanotechnology, vol. 14, no. 4, p. 313, 2019.

[310] H. Lin et al., "A 90-nm-thick graphene metamaterial for strong and extremely broadband absorption of unpolarized light," Nat. Photonics, vol. 13, no. 4, pp. 270-276, 2019.

[311] M. Negri et al., "Tuning the radial structure of core–shell silicon carbide nanowires," CrystEngComm, vol. 17, no. 6, pp. 1258-1263, 2015.

[312] I. Aksyanov, M. Kompan, and I. Kul’kova, "Raman scattering in mosaic silicon carbide films," Physics of the Solid State, vol. 52, no. 9, pp. 1850-1854, 2010.

[313] P. A. Temple and C. Hathaway, "Multiphonon Raman spectrum of silicon," Physical Review B, vol. 7, no. 8, p. 3685, 1973.

[314] Q. Pan et al., "Electrospun mat of poly (vinyl alcohol)/graphene oxide for superior electrolyte performance," ACS applied materials & interfaces, vol. 10, no. 9, pp. 7927-7934, 2018.

[315] S. Sarkar, K. Raul, S. Pradhan, S. Basu, and A. Nayak, "Magnetic properties of graphite oxide and reduced graphene oxide," Physica E: Low-dimensional Systems and Nanostructures, vol. 64, pp. 78-82, 2014.

[316] P. Avouris and C. Dimitrakopoulos, "Graphene: synthesis and applications," Materials today, vol. 15, no. 3, pp. 86-97, 2012.

[317] K. E. Whitener Jr and P. E. Sheehan, "Graphene synthesis," Diamond and related materials, vol. 46, pp. 25-34, 2014.

[318] W. A. De Heer et al., "Epitaxial graphene," Solid State Communications, vol. 143, no. 1-2, pp. 92-100, 2007.

[319] M. Amjadipour, J. MacLeod, N. Motta, and F. Iacopi, "Fabrication of free-standing silicon carbide on silicon microstructures via massive silicon sublimation," Journal of Vacuum Science & Technology B, Nanotechnology and Microelectronics: Materials, Processing, Measurement, and Phenomena, vol. 38, no. 6, p. 062202, 2020.

[320] C. A. Schneider, W. S. Rasband, and K. W. Eliceiri, "NIH Image to ImageJ: 25 years of image analysis," Nature methods, vol. 9, no. 7, pp. 671-675, 2012.